OPTIMIZATION OF THE MECHANICAL PROPERTIES OF Ti-6Al-4V ALLOY PRODUCED BY THREE DIMENSIONAL ADDITIVE MANUFACTURING USING TERMOCHEMICAL PROCESSES

A THESIS SUBMITTED TO
THE GRADUATE SCHOOL OF NATURAL AND APPLIED SCIENCES
OF
MIDDLE EAST TECHNICAL UNIVERSITY

BY

GÜNEY MERT BİLGİN

IN PARTIAL FULFILLMENT OF THE REQUIREMENTS
FOR
THE DEGREE OF MASTER OF SCIENCE
IN
METALLURGICAL AND MATERIALS ENGINEERING

JANUARY 2017

Approval of the thesis:

OPTIMIZATION OF THE MECHANICAL PROPERTIES OF Ti-6Al-4V ALLOY PRODUCED BY THREE DIMENSIONAL ADDITIVE MANUFACTURING USING TERMOCHEMICAL PROCESSES

submitted by **GÜNEY MERT BİLGİN** in partial fulfillment of the requirements for the degree of **Master of Science in Metallurgical and Materials Engineering, Middle East Technical University** by,

Prof. Dr. Gülbin Dural Ünver
Dean, Graduate School of **Natural and Applied Sciences** _____

Prof. Dr. C. Hakan Gür
Head of Department, **Metallurgical and Materials Engineering** _____

Prof. Dr. Caner Durucan
Supervisor, **Metallurgical and Materials Engineering, METU** _____

Assoc. Prof. Dr. Ziya Esen
Co-supervisor, **Materials Sci. and Eng. Dept., Çankaya Uni.** _____

Examining Committee Members:

Prof. Dr. C. Hakan Gür
Metallurgical and Materials Engineering, METU _____

Prof. Dr. Caner Durucan
Metallurgical and Materials Engineering, METU _____

Prof. Dr. M. Kadri Aydınol
Metallurgical and Materials Engineering, METU _____

Assoc. Prof. Dr. H. Emrah Ünalan
Metallurgical and Materials Engineering, METU _____

Assoc. Prof. Dr. Ziya Esen
Materials Science and Eng., Çankaya Uni. _____

Date: 16.01.2017

I hereby declare that all information in this document has been obtained and presented in accordance with academic rules and ethical conduct. I also declare that, as required by these rules and conduct, I have fully cited and referenced all material and results that are not original to this work.

Name, Last Name : Güney Mert BİLGİN

Signature :

ABSTRACT

OPTIMIZATION OF THE MECHANICAL PROPERTIES OF Ti-6Al-4V ALLOY PRODUCED BY THREE DIMENSIONAL ADDITIVE MANUFACTURING USING TERMOCHEMICAL PROCESSES

Bilgin, Güney Mert
M.S., Department of Metallurgical and Materials Engineering
Supervisor: Prof. Dr. Caner Durucan
Co-Supervisor: Assoc. Prof. Dr. Ziya Esen
January 2017, 141 pages

Selective laser melting (SLM) is an additive manufacturing (AM) technology used for aerospace and biomedical Ti-6Al-4V alloys to produce parts with complex geometry at one step with reduced production time, scrap and cost. However, parts produced by SLM are lack of ductility due to microstructures similar to those cast products and residual stresses generated during laser processing. In this study, Ti-6Al-4V alloys produced by SLM were treated by thermo-hydrogen process (THP) to increase ductility and to refine the microstructure without changing the parts' final geometry as opposed to thermo-mechanical processes. It has been observed that conventional 4-step THP decrease alloy's mechanical properties despite refined microstructure because of grain boundary α-phase formation during β-solutionizing and eutectoid decomposition steps. Additionally, excessive growth of β-grains occurred during β-solutionizing was another drawback of the 4-step process. On the other hand, modified 2-step THP, which was conducted below α/β transition temperature, was found to increase the alloy's ductility without degrading its

strength. Although similar microstructures were developed in samples treated by 2- and 4-step THP, grain growth and grain boundary α- phase formation was not encountered in samples treated by 2-step THP. Even though hydrogen absorption of the alloy has not been changed considerably, initial microstructure of the alloy was found to be effective on final properties. THP transformed α'-martensite to fine α and β phases by significant increase in ductility, while it did not alter the type of phases and ductility too much in samples containing lamellar α+β microstructure; however, a discontinuous morphology was obtained.

Keywords: Additive Manufacturing (AM), Selective Laser Melting (SLM), Ti-6Al-4V Alloy, Thermochemical Processes (TCP), Thermohydrogen Process (THP).

ÖZ

ÜÇ BOYUTLU KATMANLI İMALAT YÖNTEMİ İLE ÜRETİLEN Ti-6Al-4V ALAŞIMININ MEKANİK ÖZELLİKLERİNİN TERMOKİMYASAL YÖNTEMLER KULLANILARAK OPTİMİZASYONU

Bilgin, Güney Mert
Yüksek Lisans, Metalurji ve Malzeme Mühendisliği Bölümü
Tez Yöneticisi: Prof. Dr. Caner Durucan
Ortak Tez Yöneticisi: Doç. Dr. Ziya Esen
Ocak 2017, 141 sayfa

Seçmeli lazer ergitme (SLE), havacılık ve biyomedikal sektörlerinde kullanılan karmaşık yapılı Ti-6Al-4V parçaların tek bir basamakta zaman, hurda ve maliyeti azaltarak üretimlerinin yapılmasını sağlayan katmanlı imalat (Kİ) yöntemlerinden bir tanesidir. Ancak, SLE ile üretilen parçaların mikroyapıları döküm ile üretilen parçaların mikroyapılarına benzer olduğu ve lazer ergitmesi sırasında kalıntı gerilmeler açığa çıktığı için bu parçaların süneklikleri düşüktür. Bu çalışmada, SLE ile üretilen Ti-6Al-4V alaşımlara sünekliği arttırmak ve mikroyapıyı iyileştirmek için termo-mekanik işlemlerin aksine parçaların son şekilini bozmayarak termo-hidrojen işlemi (THİ) uygulanmıştır. Geleneksel olarak uygulanan 4-basamaklı THİ'de, iyileştirilmiş mikroyapıya rağmen β çözündürme ve ötektoid ayrışma işlemleri sırasında tane sınırlarında α fazı birikmesi sebebiyle mekanik özellikler düşmüştür. Buna ek olarak, β-tanelerinin β-çözündürme işlemi sırasında aşırı büyümesi 4-basamaklı THİ'nin bir başka dezavantajı olarak buulunmuştur. Diğer

taraftan, α/β geçiş sıcaklığının altında gerçekleştirilen 2-basamaklı yeniden düzenlenmiş THİ'nin mukavemeti azaltmadan sünekliği arttırdığı keşfedilmiştir. 4- ve 2-basamakla THİ'ye tabi tutulan numunlerde benzer mikroyapı açığa çıkmasına rağmen 2-basamaklı THİ sonucunda numunelerde tane büyümesi ve tane sınırlarında α fazı birikmesi meydana gelmemiştir. Alaşımın hidrojen emmesi başlangıç mikroyapısı ile önemli oranda değişmediği halde son özelliklerinin başlangıç mikroyapısına bağlı olduğu bulunmuştur. THİ, α'-martenziti ince yapılı α ve β fazlarına dönüştürerek sünekliği önemli oranda arttırırken yapraksı α + β yapısının sünekliliği ve fazları üzerine önemli etkide bulunmayarak süreksiz yapının elde edilmesine sebep olmuştur.

Anahtar Kelimeler: Katmanlı İmalat (Kİ), Seçmeli Laser Ergitme (SLE) Ti-6Al-4V Alaşımı, Termo-kimyasal İşlem (TKİ), Termo-hidrojen İşlem (THİ).

To my beloved family

ACKNOWLEDGMENTS

I am grateful to my supervisor Prof. Dr. Caner Durucan for his guidance and assistance. I would not have completed writing this dissertation without his support.

I would like to express my truthful appreciation to my admirable advisor Assoc. Prof. Dr. Ziya Esen for his valuable motivation, wise criticism, exceptional advice and endless support. His ceaseless patience, valuable suggestions, feedbacks, advices, criticisms, encouragements and close collaboration helped me in all the time of my research. This thesis could not have been accomplished without his support and devoted work.

I wish to express my gratitude to my remote supervisor Prof. Dr. Arcan F. Dericioğlu for his never ending support, encouragement, advice and help throughout the entire period of the study. His feedbacks boosted my vision and widened my perspective in the field of research. I owe a great appreciation to him for allowing me to study in this research topic and in a splendid laboratory environment.

I am also grateful to Assist. Prof. Dr. Şeniz Kuşhan Akın, Dr. Elif Tarhan Bor and Dr. Kaan Pehlivanoğlu for their precious helps, advice, valuable support and encouragement during the development of the study.

I am obligated to my laboratory mates and friends; Sıla Ece Atabay, Simge Tülbez, Tuğçe Altuntop, Aylin Güneş and Güney Daloğlu for their helps, endless patience and wise suggestions. I cannot thank them enough for spending their knowledge and great effort in every process of my study.

I wish to state my deepest appreciation to Ezgi Bütev, Bengisu Akpınar, Fatih Sıkan, Serkan Yılmaz and Semih Pençereci for their never ending support and

encouragement. Additional thanks go to various friends including Erdem Budak, Çiğse Tuncel, Özge Koç, Berfu Göksel, Orhun Altunlu and Salih Özgen who believe and support me throughout the thesis writing period.

I would like to specially thank to all the technical staff of the Metallurgical and Materials Engineering Department for their suggestions, help and comments during this study.

Finally, I owe gratefulness to every individual of my beloved family for their warm support in any case regardless to my unstable mood. I feel so lucky to have such a great family. I wish to indicate my special appreciation to my mom and dad. I am so glad to have them.

TABLE OF CONTENTS

LIST OF TABLES

TABLES

LIST OF FIGURES

FIGURES

CHAPTER 1

INTRODUCTION

Ti-6Al-4V alloy is a workhorse particularly in aerospace and biomedical sectors due to its superior properties like high strength to weight ratio and outstanding corrosion resistance when compared to other metallic materials. This alloy is widely used in the applications where high temperature strength is required along with weight saving is essential for a product design. Ti-6Al-4V weight share is more than 25 % in the fan and compression sections of aero engine disks and blades, which have an operating temperature about 500 °C. The elevated temperature specific strength of Ti-6Al-4V is exceptionally greater than aluminum alloys and its density is lower as for that of steel and nickel alloys. Additionally, Ti-6Al-4V can be used as artificial implant in the body environment since it has good biocompatibility and great corrosion resistance.

Compared to conventional fabrication techniques, additive manufacturing (AM) of Ti-6Al-4V alloys offers various advantages including near net shape production of complex structural designs without the need of expensive molds, dies and labor force. An additive manufacturing method like selective laser melting (SLM) allows direct production of a part from computer aided design model with short deferments. Some properties like low time to market and high level of flexibility in SLM, attract today's manufacturing technology in which complex geometrical strategies are mandatory and cannot be provided by a conventional methods. Thus, in recent years, SLM has become more popular in a wide variety of fields producing complex Ti-6Al-4V parts.

In the course of SLM process, Ti-6Al-4V powders are formed layer by layer within a chamber in a selective manner by a laser beam under an inert argon gas environment. Optimization of process parameters such as laser power, scan velocity, powder layer thickness is essential to ensure the high material density with less residual porosity. Upon interaction of a laser beam with sufficient power, Ti-6Al-4V powders are heated and melted. Subsequent to removal of laser, the liquid Ti-6Al-4V solidifies very rapidly and fused powder forms a layer of the final part. The large thermal input in SLM causes rapid solidification of molten pool especially when laser irradiates different part of the metal at the same time.

It was found that rapid solidification in SLM gives rise some problems like formation of non-equilibrium phases in the microstructure. A very fine, acicular martensite forms when Ti-6Al-4V parts are fabricated by SLM. Moreover, laser beam induced highly localized heat input leads to internal and residual stresses while short interaction time of laser causes segregation in the structure. Numerous mechanical properties such as strength, ductility, fracture toughness and fatigue resistance individually altered in the case of SLM of Ti-6Al-4V. Also, melt pool instabilities as well as porosity and high surface roughness might arise due to non-optimal scanning parameters. Therefore, post processing of SLM parts is highly needed to ensure desired mechanical properties that meet the specifications of the standards particularly adapted to aerospace and biomedical fields.

The mechanical properties of Ti-6Al-4V can be improved when hot working is conducted at an elevated temperature. However, such treatment is not applicable particularly to the complex geometries where abnormal and multifaceted parts are required to be produced. In this study, thermochemical processes (TCP) were utilized to SLM fabricated Ti-6Al-4V parts by using hydrogen gas with the purpose of refining the microstructure and improving the mechanical properties of the samples without changing the samples' shape and dimensional tolerances. Hydrogen is a unique alloying element for Ti-6Al-4V because of its reversible penetrability; hence it both can be absorbed and removed by the fundamental processes at high temperatures. The TCP treatment done with the concept of temporary alloying with

hydrogen is broadly known as thermohydrogen process (THP) in the literature. In this study, SLM fabricated Ti-6Al-4V parts were alternatively post processed with THP because of the toned for preserving the final complex shape. The most crucial feature of THP is that of it does not deform the entire material so that the mechanical properties of SLM fabricated Ti-6Al-4V parts can be improved without plastic deformation.

Previous studies have shown that temporary alloying of Ti-6Al-4V with hydrogen has a remarkable impact on phase transformations since hydrogen promotes the transformation of β phase and retards the α phase formation. Furthermore, β transition temperature decreases sharply from 990 °C to about 800 °C even a low concentration of hydrogen absorbed into Ti-6Al-4V. Such a decrease in the β transus allows heat treatments made at lower temperatures. Temporary alloying with hydrogen has been used several times in order to improve the working, machining, sintering, etc. due to more plastically deformable and softer β phase stabilizing effect of hydrogen. Hydrogen addition into Ti-6Al-4V slows down the kinetics for martensite transformation by lowering the nose temperature and critical cooling rate as well. THP has been used by several authors because of its positive effects on Ti-6Al-4V like refining the microstructure and improving the mechanical properties. However, in the literature, this technique has not been applied to any kind of AM produced parts yet, and these studies have only been focused on cast and wrought Ti-6Al-4V parts. In this regard, the present thesis approaches to SLM fabricated Ti-6Al-4V parts as a novel post processing technique with the purpose of obtaining optimal mechanical properties conforming the ASTM standards for AM fabricated parts.

This master thesis contains five chapters to give information about the main concepts of THP and THP of SLM Ti-6Al-4V alloy. The literature review, given in Chapter 2, consists of several sections so as to present theoretical background that enlightens the main study. Firstly, properties of titanium and its physical metallurgy are explained with its suitability to aerospace and biomedical fields. Next, AM technology has been discussed by emphasizing metallic parts production. SLM

fabrication method, an AM technology, is explained in a detailed manner particularly for Ti-6Al-4V with its microstructural evaluation and mechanical characteristics after production by SLM. Moreover, the various structural properties and mechanical characteristics of THPed Ti-6Al-4V alloys are discussed in a depth perception in Chapter 2. In Chapter 3, the experimental set-up is presented along with the physical and chemical properties of initial SLM fabricated samples. The principles of various characterization methods including compositional analysis, metallographic examinations, X-ray diffractions, mechanical tests and hardness measurements are introduced within this chapter. Chapter 4 covers experimental results and their discussions with respect to structural, microstructural and mechanical doctrines. Consequently, conclusions with the future works are presented in Chapter 5.

CHAPTER 2

LITERATURE REVIEW

2.1. Introduction to Titanium and Its Applications

Titanium and its alloys are used in a variety of fields including aerospace, biomedical, petrochemical, personal product and automotive industries due to their superior properties such as high strength to weight ratio (specific strength) and excellent corrosion resistance. High specific strength at elevated temperatures makes titanium an indispensable aerospace material. As it can be seen in Figure 2.1, strength to weight ratio of Ti-6Al-4V is higher than that of most metallic materials up to 400-550 °C operating temperature. Today, following benefits are significant for widespread use of titanium alloys in aerospace industry [1].

- Pure titanium is 40% lighter than steel and nickel based super alloys,
- The tensile strength of some titanium alloys are better than ferritic and austenitic stainless steels and can be comparable to that of martensitic stainless steel,
- Titanium alloys are useful at temperature range of 400-550 °C. Titanium aluminates have even higher strength at higher temperatures.
- Their thermal expansion coefficients are less than half of aluminum and lower than that of steel.
- When operating temperature exceeds 130 °C titanium alloys could replace aluminum.

Although only composites have higher specific strength rather than any other metallic materials at lower temperatures, their usage in aerospace applications like aero engine components is diminished by their limited operating temperature extent.

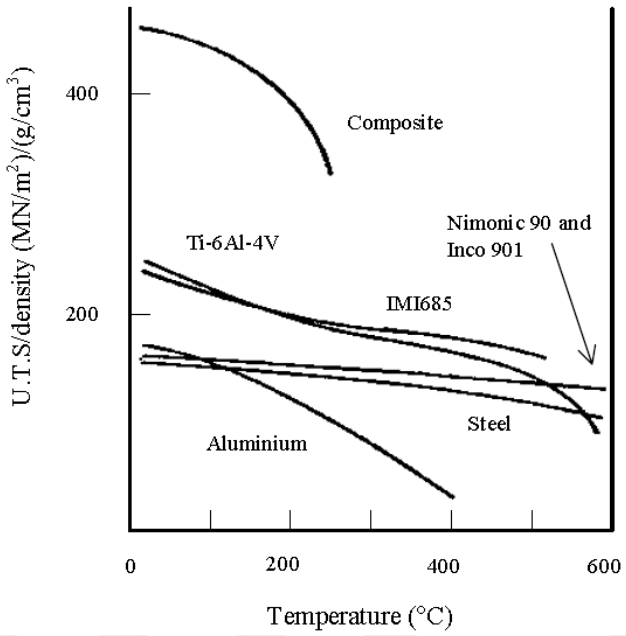

Figure 2. 1: Comparison of specific strength vs. temperature for several different materials [2].

For aerospace industry, primary selection criteria of titanium alloys based upon their lower density permitting weight saving compared to steels. The strength of titanium alloys is higher than aluminum alloys even at higher temperature. Therefore, titanium alloys offer greater resistance in high temperature applications than aluminum alloys. Moreover, weight saving can be maintained when titanium is replaced with aluminum despite its higher density of about 60% [3].

The other most widely used area for titanium alloys is the biomedical field. Since titanium has high corrosion resistance, mechanical properties close to bone and good biocompatibility in body environment, hard tissues of the body can be replaced with artificial titanium implants. Therefore, they may be used in hip joints, teeth, knees, artificial vascular stents, screw-shaped bone fixation devices and so on, Figure 2.2 [4].

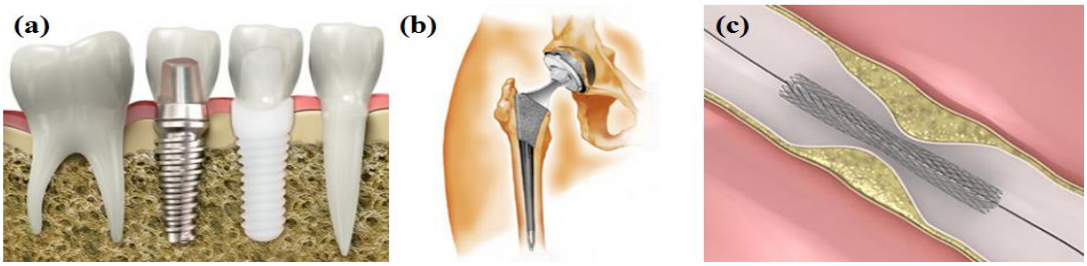

Figure 2. 2: Various biomedical application of titanium alloys; (a) dental implant, (b) hip joint, (c) vascular stent [5, 6].

2.2. Properties of Titanium and Its Physical Metallurgy

In Table 2.1 presents some physical and mechanical properties of titanium and titanium alloys and other metals like Fe, Ni and Al.

Table 2. 1: Some basic characteristics of titanium and its alloys compared to some other metallic materials [7].

Property	Ti	Fe	Ni	Al
Melting Temperature (°C)	1670	1538	1455	660
Allotropic Transformation (°C)	882	912	-	-
Crystal Structure	hcp→bcc	bcc→fcc	fcc	fcc
Room Temperature E (GPa)	115	215	200	72
Yield Stress (MPa)	1000	1000	1000	500
Density (g/cm^3)	4.5	7.9	8.9	2.7
Comparative Corrosion Resistance	very high	low	medium	high
Comparative Reactivity with O_2	very high	low	low	high
Comparative Price of Metal	very high	low	high	medium

Even though titanium has relatively higher specific strength among other metals, its price relatively higher because of the expensive production method called as Kroll's

process. The high price of titanium is mainly related to high reactivity with oxygen. Due to high oxygen affinity of titanium, the use of vacuum or inert atmosphere is required during the production process to avoid oxygen contamination. Conversely, high oxygen reactivity leads to formation of immediate oxide layer throughout the surface when titanium exposed to air. This thin surface oxide layer provides excellent corrosion resistance, which is desirable in various applications [8].

Pure titanium undergoes an allotropic phase transformation from hexagonal close packed (hcp) α-phase, which is stable at the room temperature, to body centered cubic (bcc) β-phase when the temperature is raised above 882 °C. Schematic unit cell of hcp-α and bcc-β phases are given in Figure 2.3 along with their lattice constants. The hcp α phase unit cell has the lattice parameters of a=0.295nm and c=0.468nm, while the bcc β phase has a=0.0332nm at 900 °C. The α phase has 3 slip systems and thus, it is less ductile when compared to β phase which has 12 slip systems. The β phase is more plastically deformable and softer than the α as a consequence of easier gliding of dislocations over slip systems and the higher atomic density in bcc crystal [9].

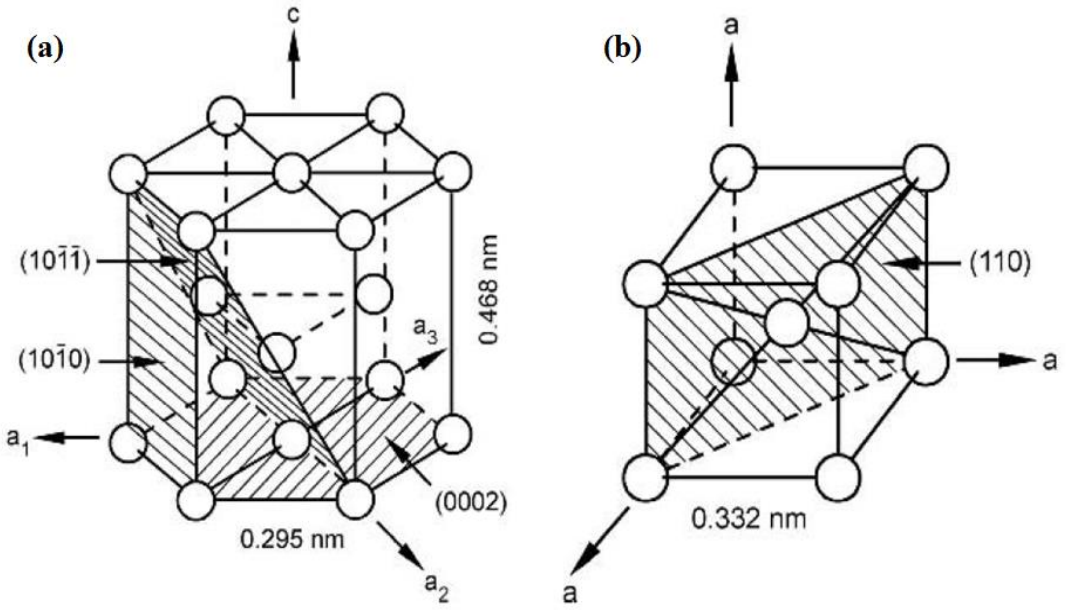

Figure 2. 3: The unit cell of titanium; (a) α-phase, (b) β-phase [9].

The allotropic transformation temperature, i.e. 882 °C for pure titanium, is dependent on the amount of substitutional and interstitial alloying elements. The effect of various elements on α to β transition temperature is shown in schematic phase given in Figure 2.4. Aluminum is the most commonly used substitutional alloying element due to its high solubility in both α and β phases. Other alloying elements such as B, Ge, Ga and rare earth elements raise the β transus temperature just as Al; however, their solid solubility in titanium are far below as compared to Al. Nitrogen, carbon and oxygen are the α phase stabilizers among the interstitial elements. Especially oxygen has significant α phase stabilizing effect, whereas oxygen content increases the embrittlement risk drastically and decreases the ductility [10]. Only hydrogen has β phase stabilizing effect among the interstitial elements, thereby, lowering the α to β transition temperature. V, Nb, Mo, Fe, Cr and Si elements are the most widely used β stabilizer substitutional elements. . Alloying titanium with proper amounts of these elements is sufficient to make β phase stable at room temperature. Zr, Hf and Sn are the last group of alloying elements having no stabilizing effect. Particularly Sn is considered as α phase stabilizing element in many commercial applications even if it has no effect on the α to β transition temperature. When Al is present in structure, Sn behaves like α phase stabilizer with the result of the replacement in hexagonal ordered Ti_3Al phase [11, 12].

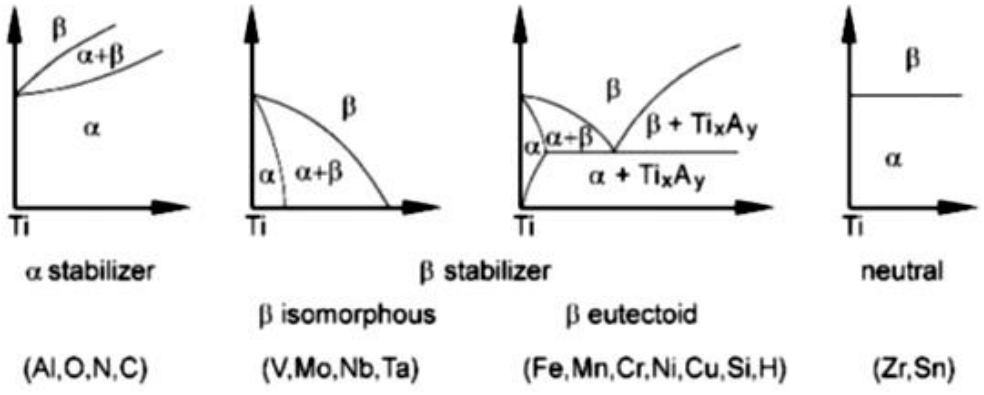

Figure 2. 4: Influence of some alloying elements on titanium phase diagrams [9].

The α and near α alloys are stable at the low temperatures. With increasing amount of β stabilizing elements, β phase become more stable at the room temperature. In α

+ β alloys, α phase dominantly present in the microstructure along with a little amount of β phase. In general term, β titanium alloys is determined by retaining 100% β phase when they have been quenched from β phase field [13].

2.3. Titanium Alloys

There are various classes of titanium alloys such as α and near α alloys, α+β alloys, near β and β-alloys with different properties, which are classified according to content and type of the alloying elements, Figure 2.5.

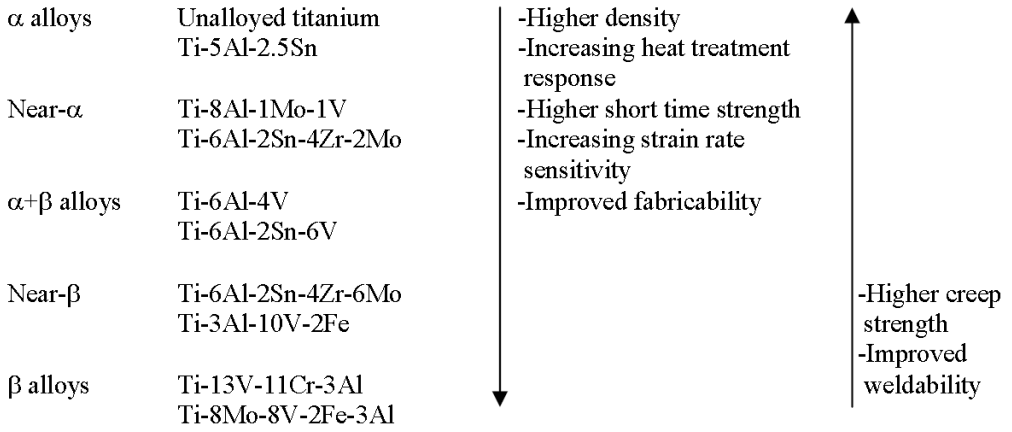

Figure 2. 5: Properties of various classes titanium alloys [14].

2.3.1. α and near α alloys

Commercially pure titanium (CP-Ti) and the titanium alloyed with an α phase stabilizer element fall into this category. At lower temperatures, possessing 100% hcp titanium is the main criteria to be classified as a near α alloy. Both substitutional alloying elements (Al, Sn) and interstitial elements (N, C, O) are soluble in hcp α phase. α titanium alloys such as Ti-3Al-2.5V, Ti-5Al-2.5Sn, Ti-8Al-1Mo-1V, Ti-6Al-2Sn-4Zr-2Mo are widely used in variety of fields, where high creep resistance is required like gas turbine components. Properties of such alloys cannot be altered

by a heat treatment and thus, they are useful at higher temperatures compared to α + β alloys such as Ti-6Al-4V alloy. Only solution annealing treatment, just below the 100% β phase field, can be utilized to this type of alloys. They have excellent corrosion resistance and good weldability with respect to other types of titanium alloys. Some α alloys like Ti-0.3Mo-0.8Ni contain β phase stabilizers and minor amounts of Si to enhance the creep resistance [13, 15, 16]. The mechanical properties of α phase can be increased enormously by dissolving aluminum in it. Al has significant effect on the strengthening mechanism of titanium with ensuring the formation of hexagonal Ti_3Al phase.

2.3.2. α + β alloys

The alloys belonging to this category contain both α and β stabilizer elements together. As a general term, to promote the α and β phase formations together, aluminum is added with one or two β stabilizer substitutional elements such as V and Mo. Likewise, Ti-6Al-4V alloy, which is a workhorse for titanium industry, contains predominantly α phase stable along with β phase at the room temperature. Combined properties of α and β phases are desirable when higher strength than α alloy or better creep resistance than β alloy is required. An α + β alloy can be heat treated and heat treating capability increases more readily with increasing content of β favoring elements. Solutionizing below the β transition temperature is the most widely performed heat treatment. Amount and type of the alloying elements of α + β alloy have strong influence on several properties ranging from hardenability, strength to plastic deformability. Properties of α + β alloys are shown in Figure 2.6. Ti-6Al-4V alloys find applications in variety of working fields in industry and academic researches as they possess properties combination of α alloys and β alloys. The α + β alloys include alloys such as Ti-6Al-4V, Ti-6Al-7Nb, Ti-6Al-6V-2Sn, Ti-8Mn, Ti-7Al-4Mo, Ti-3Al-2.5V, Ti-6Al-2Sn-4Zr-6Mo [1, 14].

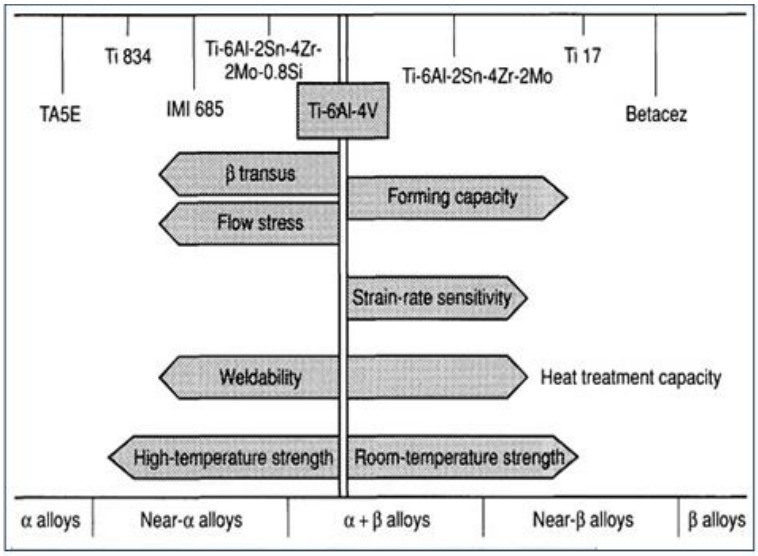

Figure 2. 6: Main characteristics of titanium alloy family [1].

2.3.3. β alloys

A titanium alloy is considered as β alloy when β phase retains upon quenching from 100% β phase field without transformation to martensite. Sufficient amount of β stabilizer elements cause a high strength up to 1400 MPa after heat treatment. These types of alloys are more readily heat treatable and thus mechanical properties can be varied in a broad range. Solution heat treatment is done above the β transition temperature as a regular process. The room temperature strength is significantly higher than other titanium alloys. Good forming capability due to presence of bcc beta phase, among other types of titanium alloys, leads to easier cold rolling of β alloys. However, β alloys are not weldable and creep resistance is lower with respect to α alloys. Despite the name, β phase is metastable at room temperature and thus transformation to α phase can be observed at a result of cold working or heating to an elevated temperature [1, 14]. The β alloys include alloys such as Ti-10V-2Fe-3Al, Ti-15V-3Cr-3Al-3Sn, Ti-8Mo-8V-2Fe-3Al, Ti-15Mo-2.7Nb-3Al-0.2Si, Ti-3Al-8V-6Cr-4Mo-4Zr.

2.4. Ti-6Al-4V Alloy

The Ti-6Al-4V alloy is an α + β alloy which has 6 wt.% aluminum as α phase stabilizer and 4 wt.% vanadium as β phase stabilizer. Approximately 90 wt.% hcp α phase is stable at room temperature along with 10 wt. % metastable bcc β phase upon slow cooling from the high temperature β phase region. Depending on the type of heat treatment and cooling rate, the amounts of α and β phases and the microstructure vary and may include primary or globular α, grain boundary allotriomorph α, martensitic, basketweave and Widmanstätten structures [17].

The β transition temperature of Ti-6Al-4V alloy might be altered with by changing the interstitial elements, however, transformation temperature of α and β phases to 100% β system is about 995 ± 20 °C [8]. When the alloy is very slowly cooled from above the β transition temperature, β phase primarily transforms to globular α. For higher cooling rates, acicular α plates emerged into β grain boundaries in a Widmanstätten which is a casting microstructure shown in Figure 2.7 [18].

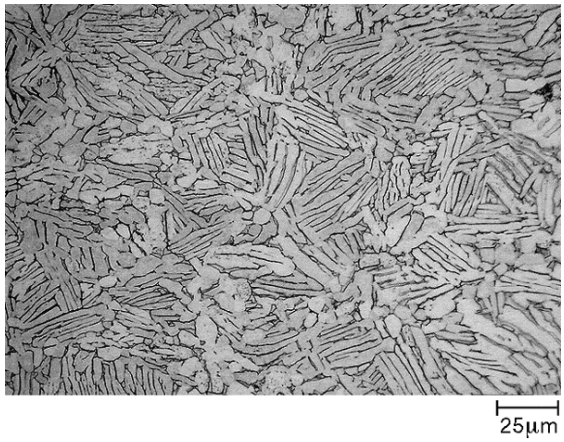

Figure 2. 7: Optical micrograph showing Widmanstätten structure resulted in a casting where α phase in white and β phase is dark [19].

The nucleation rate of α plates into primary β grains are enhanced by the increasing cooling rate thereby the width and length of these α plates are mainly determined by the cooling regime [18]. Besides, upon quenching from all β region, when the Ti-6Al-4V alloy gets through the Ms (martensite-start), the transformation from β to α'

phase (hcp martensite) is observed. The martensite in titanium exists in two forms including hexagonal martensite and orthorhombic martensite (α" phase). The amount of α'/α" phase is mainly dependent on chemical composition of β stabilizer elements in the alloy. After quenching from 100% β phase field softer α" martensite can be formed in either condition where ≥ 10 wt.% vanadium is present or hydrogen is added [20]. The schematic illustration of phase constituents of Ti-6Al-4V alloy upon quenching from different temperatures is shown in Figure 2.8.

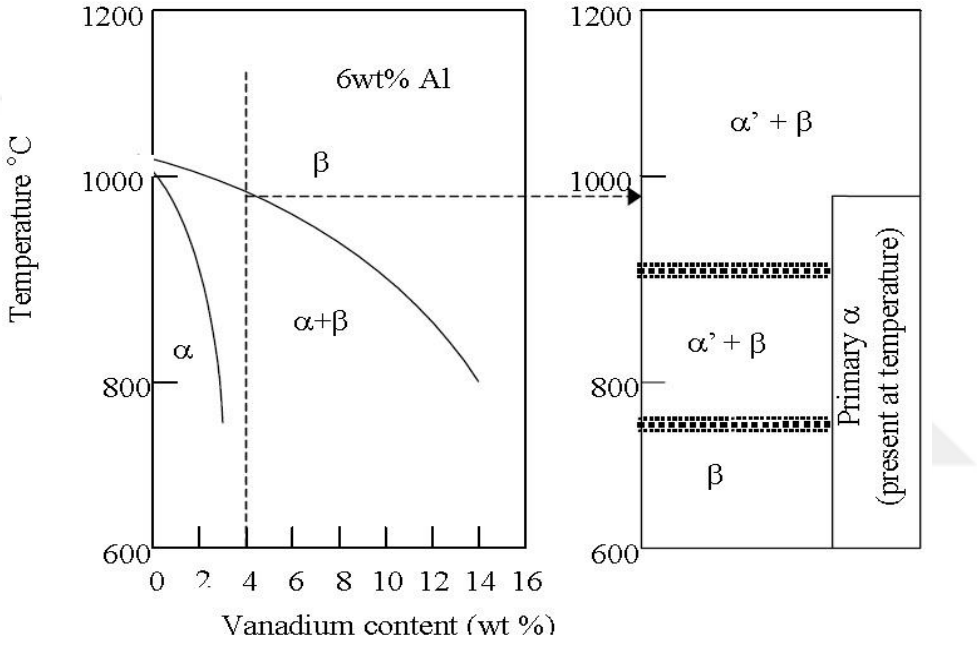

Figure 2. 8: Phase constituents of Ti-6Al-4V alloy upon quenching [8, 20].

The relationship between mechanical properties and microstructure of Ti-6Al-4V alloy has been studied by Lütjering [17]. According to the study, the colony size of α plates is the most important microstructural parameter effecting the mechanical properties in Ti-6Al-4V alloy. With decreasing in α colony size the mechanical properties such as yield strength, ductility, and crack propagation resistance determining the low cycle fatigue (LCF) strength are enhanced. Only fracture toughness and macro crack propagation resistance are decreased with decreasing α colony size. Therefore, texturing the microstructure is crucial for determining the mechanical properties of the Ti-6Al-4V used in various applications. The size of α colony mainly depends on cooling rate from all β phase field, thereby, the final

microstructure determined by fabrication process and subsequent heat treatment [17].

Ti-6Al-4V alloy, which the extensively used material in aerospace industry, can be used in various forms in cast and wrought conditions. Conventionally, Ti-6Al-4V components are fabricated by machining and hot working of wrought products. The final microstructure, which determines the mechanical properties, is mainly affected by the temperature and strain rate of deformation. In such cases, mechanical properties are mainly defined during deformation at elevated temperature. However, Ti-6Al-4V alloy is known as their hard plastic deformability with respect to steel and aluminum alloys. Significant machining process and labor force are needed when complex and complicated parts like porous hip joint disks are desired to produce with a traditional method [8].

In today's processing technology there is a strong demand of easier and cost efficient method to produce complex Ti-6Al-4V parts [21]. One of the popular techniques called AM mostly eliminates intermediate processing steps (deformation, machining, welding, etc) and the need for dies and reduces production time considerably.

Elemental composition and mechanical properties of cast, wrought and AM Ti-6Al-4V alloys are more or less the same; however, they may show a slight difference shown in ASTM standards presented in Tables 2.2 and 2.3.

Table 2. 2: The compositions for cast, wrought and AM Ti-6Al-4V conforming ASTM standards.

Element	Chemical Composition (wt. %)		
	ASTM F1108-14 (cast)	**ASTM F136-13 (wrought)**	**ASTM F2924-14 (AM)**
Al	5.50 to 6.75	5.50 to 6.50	5.50 to 6.75
V	3.50 to 4.50	3.50 to 4.50	3.50 to 4.50
Fe	0.30 max.	0.25 max.	0.30 max.
O	0.20 max.	0.13 max.	0.20 max.
C	0.10 max.	0.08 max.	0.08 max.
N	0.05 max.	0.05 max.	0.05 max.
H	0.015 max.	0.015 max.	0.015 max.
Titanium	0.015 max.	Balance	Balance

Table 2. 3: Minimum tensile properties of cast, wrought, AM Ti-6Al-4V alloys.

Standard	YS (MPa)	UTS (MPa)	Elongation %	Reduction of Area %
ASTM F1108-14	758	860	8	14
ASTM F136-13	795	860	10	25
ASTM F2924-14	825	895	10	15

2.5. Additive Manufacturing (AM)

2.5.1. Introduction to Additive Manufacturing and 3D Terms

3D printing is popular term of additive manufacturing (AM) for what used to be called as rapid prototyping (RP) [22]. The concept of printing a physical 3D object involves extending of 2D processes into the third dimensions. Additive manufacturing term is related to the fabrication process of components by adding building materials (partially sintered or melted & solidified powders) in layers. This technology differs from machining processes, which remove materials from a single piece of unibody, and the final form of the material is achieved in a single process without any subsequent plastic deformation or material removal step [22].

Development the concept of AM was originated from utilizing computers, lasers and controllers to up to date life. In 1980s, parallel patents were obtained by some individuals including; Murutani (Japan), Andre et al. (France), Charles Hull (USA). From beginning to these days, the principle of AM technology is to fabricate a model with using computer aided design (CAD) without the need of complex process planning including tools and additional fixtures as other manufacturing techniques. Every each additional processing steps lead to additional labor force as well as extra production time. AM only needs basic understanding of materials and machines that are used [23].

The AM of rely on adding building materials layer by layer in a thin cross section derived from CAD model. Every each layer has its own thickness which determines the final shape of the material. Thinner the adding layers promote fabrication of more similar parts to the originals produced by a conventional method [24]. However, throughout the AM, layer thickness can be affected from several parameters including thermal inputs and heating sources, which will be discussed in further in the following parts. In today's AM technology, production parameters of different kinds of materials differs from each other, thereby, commercialized AM

machines and related process requirements are varied significantly by the materials to be manufactured [24].

2.5.2. The Profits of AM

This technology is described as a revolution in manufacturing and product development chain for many people. For some, AM technology is still in its growing stage and in near future its ultimate consequences will bring us a new industrial revolution [25]. The main benefit of AM is due to its structural freedom which serves the purpose of manufacturing extremely complex parts in a single production stage. By comparison with AM, conventional methods require multiple stages to produce complex parts. Number of processes are reduced when AM is used instead of any conventional manufacturing method [26]. For instance, 16 individual parts, including screws and nuts, must be assembled to produce an aircraft ventilating slot sample, however the part can be obtained in a single step when AM is applied [27].

Alongside the design flexibility in AM, following process advantages are unique to AM [27];

Complexity in Shape: The capability of shape complexity eliminates the need for molding or hard tooling which can increase cost of the entire manufacturing process.

Complexity in Hierarchy: Hierarchical complexity can be tailored with controlling the laser power, cooling rate, scan velocity in a particular location in multiple size scales including nano/micro microstructures, mesostructures and macrostructures.

Complexity in Function: During the building of a functional part, it is advantageous to construct multiple parts at the same time into components to avoid post processing.

Material Complexity: The opportunity of varying the material composition at different locations is possible through some AM machines.

2.5.3. AM Processing Steps

AM basically involves some processing steps mainly independent from the type of AM machine. From desktop sized simple 3D machines to larger industrial processing machines, all manufacturing is based on several stages beginning with virtual CAD model [28].

1. Computer Aided Design (CAD) Model
2. Conversion to STereoLithography (STL) file format
3. STL File Manipulation into AM Machine
4. Machine Setup
5. Building of Parts
6. Material Removal From the Building Platform
7. Post Processing

2.5.4. Types of AM Processes

AM processes use either laser or electron beam as an energy source to manufacture components using the starting materials in powder or wire form. In the case of production based on powders as raw materials, the laser/electron beam can be directed to a stationary powder bed having a specific layer thickness on a building platform or powder/powder mixtures may be fed to platform through a nozzle which lies near the laser beam. These processes are called, respectively, powder bed fusing process and directed energy deposition process [29].

2.5.4.1. Powder Bed Fusion Process (PBF)

In the method of PBF, schematically shown in Figure 2.9, the fusion is induced by an interaction between thermal source and powder particles. The heat source is most commonly provided by a laser or an electron beam. When the powder bed is

irradiated by a thermal source, a layer of powder is melted or heated just below the melting point and subsequently, the fabrication piston is lowered by one layer thickness to add a new powder layer with a powder roller. During manufacturing, oxidation is prevented with introduction of an inert gas such as nitrogen or argon or by use of vacuum environment as in electron beam melting (EBM) technology [27, 30].

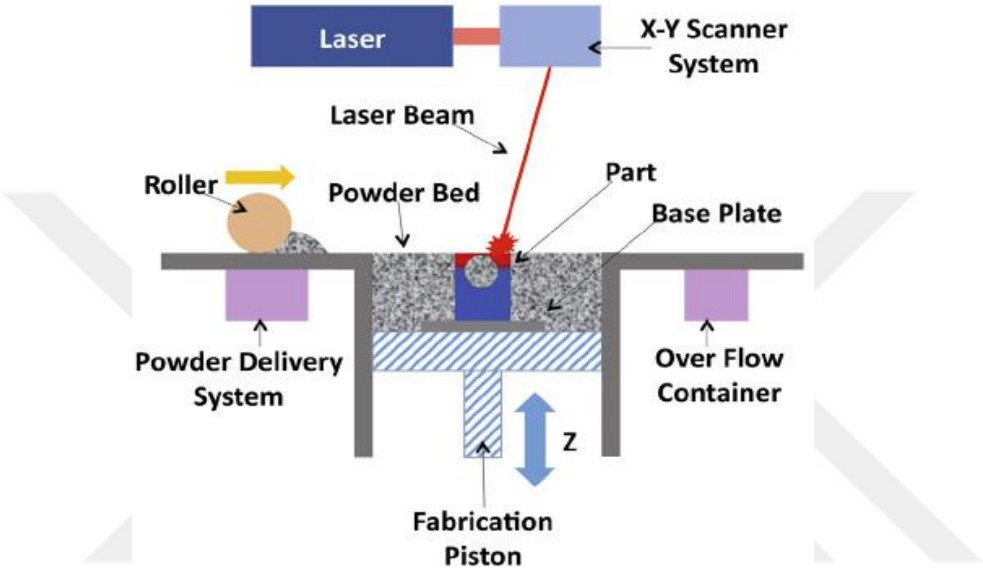

Figure 2. 9: The powder bed fusion process using laser as a thermal source [30].

Laser Based PBF Systems for Metal Manufacturing:

The lasers are utilized thanks to their leading properties of providing highly collimated beam energy and high intensity. By this means, lasers can be moved rapidly in a specific location with using a scanning mirror. Once the laser makes contact with powder bed, a layer of powder melts and subsequently solidifies very quickly in a selective manner when the laser is focused to different location, which is a fundamental for AM of metallic materials [31].

Laser based PBF systems for sintering and complete melting of metallic materials are commercially applied by several companies: Selective Laser Melting Solutions (Germany), EOS (Germany), 3D Systems (France/USA), Renishaw (UK), Realizer (Germany) and Concept Laser (Germany). There are several common terminologies

for the technologies used by these companies such as selective laser melting (SLM). The terms of selective laser sintering SLS and Laser Cusing are also used by some manufacturers [27, 31].

Processing of metal powders are more difficult than polymer powders because of their high thermal conductivity, tendency to oxidation, high surface tension, residual stresses and laser reflectivity [32]. To overcome these inherent issues, selective remelting approach has been developed by Fraunhofer Institute for Laser Technology of Germany. Within the purpose of increasing absorptivity of laser beam, they enabled Nd-YAG laser instead of CO_2 laser for easing better wavelengths. Today, almost all machines, developed by the companies mentioned above, use fiber lasers to obtain better beam quality and energy efficient lasers [33, 34].

Laser based PBF process machine manufacturers are aware of the fact that the material properties are as important as the machine technology to determine the final structure. So that, they developed some process parameters altered by the type of material to be manufactured. These variables can be counted as layer thickness, laser power, laser velocity, build volume, scanning strategy, and more [32, 35].

Electron Beam Based PBF Systems for Metal Manufacturing:

Electron beam melting (EBM) is a specific technique that uses electron beam as a heat source, which was commercialized by Arcam AB, Sweden, in 2001. Similar to laser based systems, in the EBM process, an electron beam contacts with previously laid powder layer which causes complete melting and solidification [36, 37].

There are several differences between working principles of SLM and EBM due to their energy source, Table 2.4. While powder particles are heated with absorption of laser beams in SLM, in EBM heating is provided by the kinetic energy transformation from electrons to powders. In EBM powder bed, a higher temperature is achieved than SLM powder bed, so that high melting temperature

materials are manufactured in a short period of time. Higher temperature in EBM leads to larger and more diffusive heat input and therefore, cooling rate is slower than SLM process. In EBM, more similar microstructure to a cast microstructure is obtained and less amount of porosity is achieved. Rapid cooling in SLM causes finer grain sizes in the microstructure but larger heat input differences in a unit of time lead to arise of non-equilibrium phases. Moreover, the type of material to be produced in SLM and EBM is different. EBM powder bed is required to be conductive. Thus, EBM is only used to manufacture conductive materials like metals; however, SLM can be applied to any type of material which has the capability of absorbing the energy of the laser wavelength (e.g. metals, ceramics and polymers) [38, 39]. An illustration of an EBM system is shown in Figure 2.10.

Table 2. 4: Differences between SLM and EBM processes [31].

Characteristic	SLM	EBM
Thermal source	Laser	Electron beam
Atmosphere	Inert gas	Vacuum
Scanning	Galvanometers	Deflection coils
Energy Absorption	Absorptivity limited	Conductivity limited
Powder preheating source	Infrared or resistive heater	Electron beam
Scan speed	Limited by galvanometer	Very fast
Cost of energy	High	Moderate
Surface quality	Moderate	Poor
Feature resolution	Excellent	Moderate
Materials	Polymer, metal, ceramic	Metals
Powder particle size	Fine	Medium

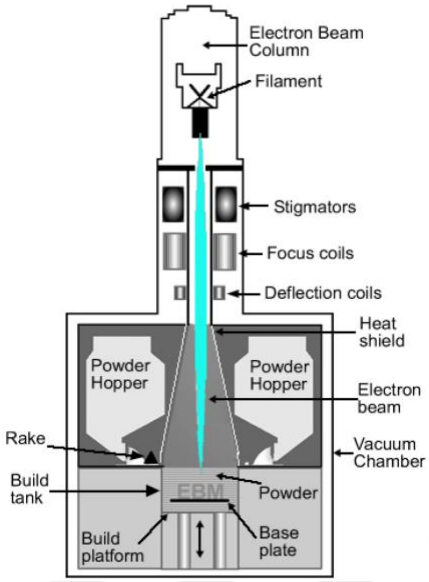

Figure 2. 10: EBM apparatus [36].

Outcomes of PBF Processes:

Laser and electron beam metal production systems are broadly used in biomedical and aerospace industry because of their complex geometrical advantages and material related benefits. Despite some unique process advantages in PBF technology, there are some drawbacks when compared to conventional manufacturing processes. Apart from other technologies, in metal PBF processes, supporting materials are required in order to keep solidified powders fixed to the build platform. These supports are also necessary to avoid warping during solidification; however, an additional process is required to remove supports from entire body of the part. When compared to traditional metal manufacturing processes, the surface quality is far below in PBF. The roughness is mainly affected by the process parameters such as powder particle size and scan velocity. Decreasing the powder size and the scan velocity allow production of a smoother surface. The porosity was a vital issue for PBF processes when this technology has been introduced newly; yet today, this disadvantage can be outfaced with ensuring complete melting and optimizing process parameters in both laser and electron beam technologies. Because of the residual stresses and non-equilibrium phases present in

PBF processed metals, a subsequent heat treatment is required before application [40 - 42].

2.5.4.2. Directed Energy Deposition Process (DED)

Directed energy deposition (DED) method uses a heat source based on laser or electron beam to melt powders before they are deposited to the substrate. A schematic illustration of laser based DED system is shown in Figure 2.11.

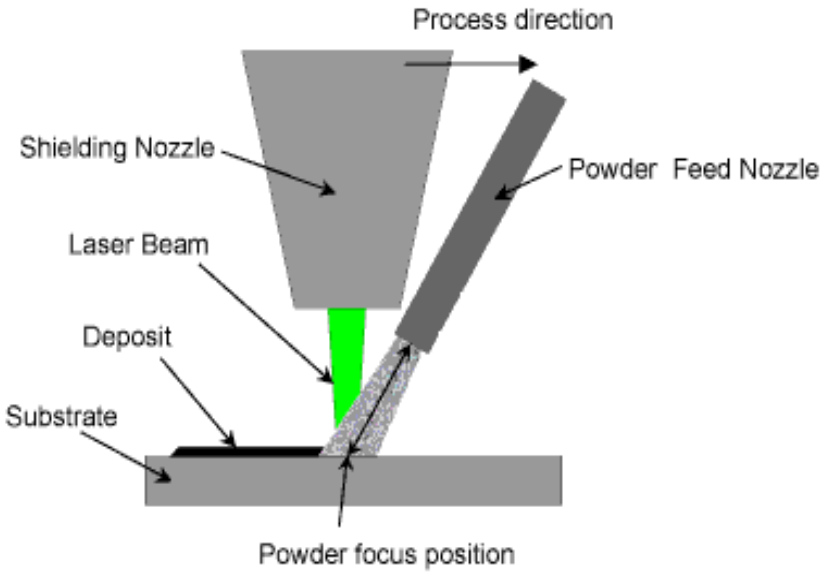

Figure 2. 11: Laser based DED system [43].

A basic DED machine consists of a deposition head which hosts a powder nozzle, an inert gas tube and a heat source. Previously melted powder particles are deposited in a certain direction controlled by substrate and deposition head movement. In most DED systems, the substrate and the deposition head can be moved in x, y and z axes.

Laser Based DED Systems for Metal Manufacturing:

Laser based DED system was firstly developed by Sandia National Laboratories, USA. The technology, called as LENS, was commercialized by Optomec, USA in

1997 [44]. This process is usually referred as laser metal deposition (LMD) owing to the fact that it is majorly applied to produce metal parts. Recently, like laser based PBF processes, LMD technology uses fiber laser as a heat source after having experience of Nd-YAG laser. Powders are deposited in an inert gas environment to prevent oxidation. Apart from Optomec, there are number of companies using this technology; POM Group, USA, was acquired by DM3D Technology, AeroMet Inc., USA, Accufusion, Canada and Controlled Metal Buildup (CMB), Germany, Trumpf Group, Germany [27, 45].

Electron Beam Based DED Systems for Metal Manufacturing:

This technology was initialized by NASA Langley, USA, in order to manufacture and repair their aerospace components, which is called Electron Beam Freeform Fabrication (EBF). The process of EBF operates with very high electric current and relatively slower deposition rates under vacuum. Moreover, different from laser systems, electron beam processes use wire feeding instead of powder particles. Another company which develops electron beam DED machines is Sciaky, USA. Sciaky machines complete their manufacturing in huge vacuum chambers proving very large build scales up to 6 m. This company especially focused on building large metallic components with rapid depositing rates for the use of aerospace industry [46, 47].

Outcomes of DED Processes:

Direct energy deposition technology is capable of manufacturing parts with full density and stable microstructural properties. Unlike PBF processes, the final microstructure can be controlled as unparalleled distribution because of directional solidification feature in DED. The DED products are very good candidates for the replacement, repair and modernization applications. Due to deposition principle in DED processes, corrosion and wear resistance thin layer coatings can be performed [48]. Poor surface quality, slower scanning speed and very long building times are

the major process drawbacks for DED processes. When compared to PBF techniques, DED processes are not able to manufacture complex structural designs because of the insufficient supporting between the substrate and the part. After manufacturing step, a post processing is usually required to avoid residual stresses [49-51].

2.6. Additive Manufacturing of Ti-6Al-4V Alloy

Recently, additive manufacturing (AM) technology is mainly focused on to produce complex parts particularly used in biomedical and aerospace applications. Due to the unique properties of Ti-6Al-4V alloy as pointed out in section 2.1, biomedical and aerospace fields give close attention to manufacture this alloy with an alternative process which allows structural flexibility and cost efficiency. For this reason, number of metal AM processes (e.g. powder bed fusion and directed energy deposition) has been developed to manufacture complex Ti-6Al-4V parts. In this section, together with the additive manufacturing of Ti-6Al-4V alloy, various structural properties such as densification phenomena, mechanical behavior and microstructure are summarized based on a comparative analysis of different production methods. The AM processes mentioned in this section are; selective laser melting (SLM), selective laser sintering (SLS), electron beam melting (EBM) and laser metal deposition (LMD).

2.6.1. Densification Phenomena

In Table 2.5, as-built densities of Ti-6Al-4V are summarized according to type of AM processes including SLM, SLS, EBM and LMD. AM machines given in Table 2.6 are the most commonly used technologies to produce Ti-6Al-4V aerospace parts. As-built densities can be reached up to 99%, if the processes parameters such as layer thickness, scan velocity, scan strategy, etc., are determined properly [52, 53]. Only in SLS technology, the theoretical density falls below 99% and mostly is

around 95% because of the solid state sintering, which is lower than the melting point (1660 °C) for Ti-6AL-4V. In SLS process, sintering mechanism is completed in the β phase field corresponding to approximately 1300 °C and subsequent treatment like hot isostatic pressing (HIP) is required in order to increase the density. HIP, which is a default processing after laser sintering of Ti-6Al-4V, allows an alteration in microstructure and decreases the porosity [35, 44, 45, 54 - 61]. The capability of maintaining complete melting in SLM, EBM and LMD causes the molten phase to fill the pores; thereby, fully dense parts can be produced by any of these methods. Many authors have reported that in EBM process, it is possible to produce parts having more than 99% density by maintaining optimum parameters [58, 62]. However, in SLM technology the theoretical density is about 99% which is lower than EBM and LMD techniques due to rapid melting/solidification and entrapped argon gas (more than LMD) [34, 63, 63].

Table 2. 5: AM process variables and as-manufactured Ti-6Al-4V densities [35, 44, 45, 54 - 61].

AM Method	AM Machine	Heat Source	Build volume in mm (x/y/z)	Part Density
SLM	SLM 280 HL	400W IPG fiber laser (x2)	280x280x350	≈ 99 %
SLS	EOSINT M280	400W Yb fiber laser	250x250x325	< 99 %
EBM	Arcam A2X	3000W e-beam power	200x200x380	> 99 %
LMD	LENS MR-7	5000W IPG fiber laser	300x300x300	≥ 99.9 %

2.6.2. Microstructure of Additive Manufactured Ti-6Al-4V Alloy

In both PBF and DED techniques, a part is produced layer by layer via direct contact of a heat source focused on powder or wire. In all AM techniques, solidification occurs in very short time due to large thermal ingredients no matter what the process type is. Also deposition of a subsequent layer is an important factor that affects the resulting microstructure. While a layer is solidified, the latter is deposited with high temperatures onto previously deposited layer. Interaction between these two layers leads to microstructural alterations induced by heat exchanging throughout the process. Pre-heating of powders (or wires), substrate heating and building temperature have strong impact on the final microstructure [53, 60].

Selective Laser Sintering:

SLS components are usually serviced after HIP is applied to increase the density and enhance the final mechanical properties. Das et al.[56], reported that the Ti-6Al-4V alloy which has been produced by conventional powder metallurgy (PM) has a theoretical density as same that of SLS parts and thus in both processes, HIP is a favorable subsequent method to reach a density above 99%. PM + HIP and SLS + HIP resulting microstructures have similar Widmanstätten structure consisting of α (white) and β (grey) lamellas which is illustrated in Figure 2.12.

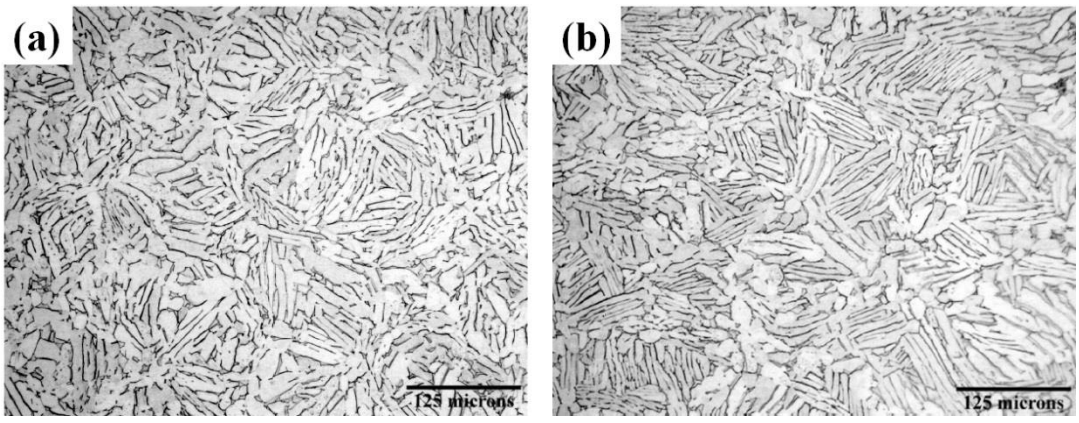

Figure 2. 12: Optical micrographs of; (a) PM + HIP, (b) SLS + HIP Ti-6Al-4V[56].

Selective Laser Melting:

SLM processing usually referred as ‘Cold Powder Bed’ technique since powder deposition is occurred over a non-preheated substrate [60]. Each layer of melted powders solidified rapidly over the cold powder bed and this results the presence of non-equilibrium phases like hcp martensite (α') which is shown in Figure 2.13. The entire microstructure consists of acicular martensite phase, when Ti-6Al-4V alloy is produced by SLM [57].

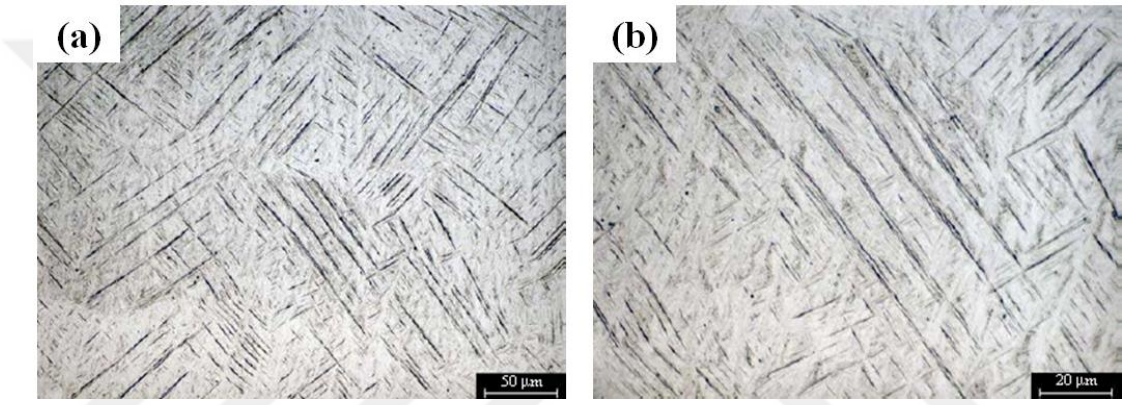

Figure 2. 13: Microstructure of SLM produced Ti-6Al-4V alloy [57].

Furthermore process parameters have strong influence on solidification behavior in SLM production. Once a laser with high power input is focused on powders, α' plates precipitate throughout the microstructure because of very large undercooling during solidification. The laser power, the scan velocity, the scan strategy, the laser spot diameter, the hatch spacing are the most important process parameters that determine the final microstructure [34, 60]. Thijs et al. have reported the effects of process parameter on microstructural evolution of SLM produced Ti-6Al-4V alloy [53]. They produced their specimens in a zigzag pattern which was obtained by rotating laser beam 90° scanning direction after scanning of each layer. Zigzag pattern is a widespread scanning parameter to obtain high density in SLM production. Wavy β grain boundaries are present in microstructure because of zigzag scanning pattern and between these primary β grains martensite plates precipitate, Figure 2.14 (a) [53]. Grain boundary α have not been observed between primary β

grain boundaries since rapid solidification occurs in SLM. In transverse cross section to building direction, Figure 2.14 (b), dark horizontal bands are equal to layer thickness in SLM production which is 30 μm. [53]. Optimum process parameters used in the reported study made by Thijs et al. is given in Table 2.6.

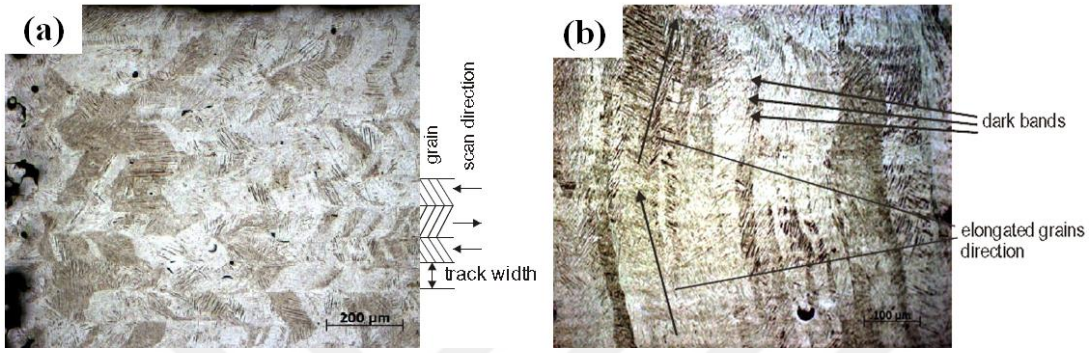

Figure 2. 14: Micrographs of SLM as-built Ti-6Al-4V; (a) front view, (b) transverse cross section [53].

Table 2. 6: SLM process parameters optimized by Thijs et al. [53].

Variable	Process Parameters
Laser Power, P (W)	42
Velocity, v (mm/s)	200
Layer Thickness, t (μm)	30
Scan Strategy	Zigzag pattern
Hatching Spacing, h (μm)	75
Energy density, E (10^{-9} J m^{-3})	93
Relative Density (%)	99.6

Electron Beam Melting:

Apart from the laser based PFB processes, in EBM, the cooling rate can be controlled via preheating of the substrate. Also the cooling rate can be decreased because of higher and more diffusive thermal inputs derived upon energy transformation from electrons to powders. Unlike SLM technique, continuous primary β grains are observed upon remelting the previously laid powders due to the higher temperature in powder bed throughout the processing [54, 64]. By maintaining the substrate material as same as the solidified material, the wetting angle (θ) can theoretically be provided as 0° allowing no nucleation barrier upon solidification [65]. Figure 2.15 shows the microstructures of EBM as-built Ti-6Al-4V components at two different directions and magnifications. The bulk microstructure is mainly composed of α + β lamellas in Widmanstätten morphology within the primary β grain boundaries. Lamellar α colonies are accumulated along the primary β boundaries orientated to the building direction. Such a directional columnar growth microstructure is reported by several authors [58 - 60].

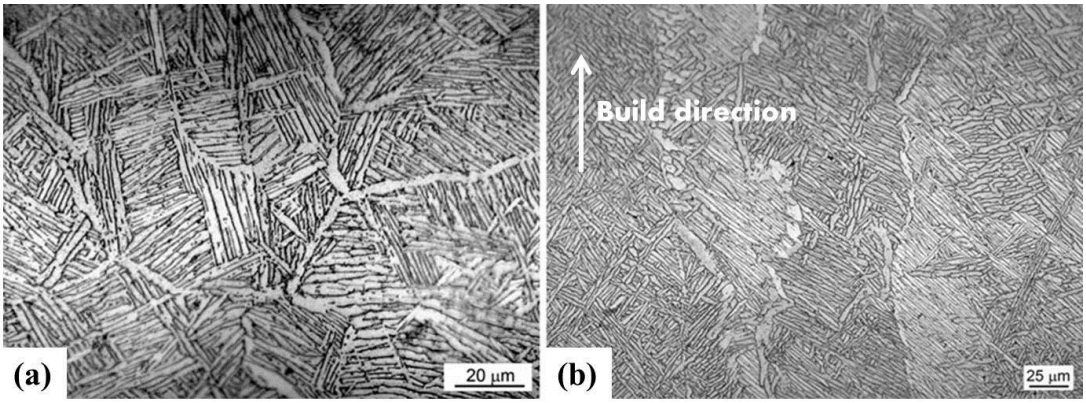

Figure 2. 15: Optical micrographs of the EBM produced Ti-6Al-4V; (a) transverse cross section, (b) longitudinal cross section [61].

Laser Metal Deposition:

Recently, wire feeding is used instead of powder deposition in LMD techniques to achieve larger building volumes and to overcome the problems of powder

contamination and high price. Particularly LENS technology is capable of building huge components with high density while the geometrical freedom is limited when compared to powder based technologies [55]. The microstructure, illustrated in Figure 2.16, shows the heterogeneity with presence of α + β lamellas and acicular α' phase. In LMD process, no primary β grains are orientated along the building direction unlike SLM and EBM due to deposition in multiple axes. For instance LENS MR-7 machine uses a laser deposition head that moves in 3 axes [66].

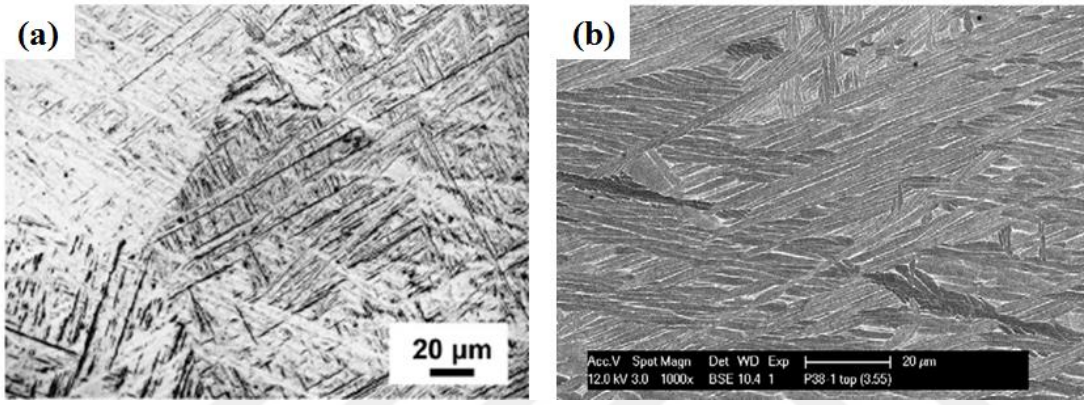

Figure 2. 16: Microstructures of LMD produced Ti-6Al-4V; (a) optical micrograph illustrating heterogeneity at the surface of the alloy (Widmanstätten α + β and acicular α') [67], (b) SEM image of transverse section showing Widmanstätten α + β [68].

2.6.3. Mechanical Properties of Additive Manufactured Ti-6Al-4V Alloys

There are numerous studies present in literature that compare the mechanical properties of Ti-6Al-4V alloy obtained after several AM methods. Brandl et al. [62] compared the tensile properties of AM processed Ti-6Al-4V with forged Ti-6Al-4V samples. They reported that SLM produced alloys have the highest strength along with low elongation. Despite the poor ductility in SLM, elongation can be improved reasonably by a subsequent annealing or HIP processing. EBM processed samples have relatively higher elongation and yield strength compared to forged Ti-6Al-4V

alloy while the yield strength of LMD processed sample is higher than EBM processed sample [62].

Murr et al. [60] also compared the mechanical properties of EBM and SLM as built samples with that of wrought Ti-6Al-4V alloys. Their experiments showed that SLM produced parts are less ductile than EBM parts because of the resulted martensitic microstructure in SLM. Therefore, a heat treatment is required to tailor the microstructure; hence they treated SLM parts at 843 °C for 2 hours and then furnace cooled. EBM processed as built parts have 12% elongation while this value is 16% in wrought Ti-6Al-4V [60].

Boufeld et al. [55] suggested that due to the heterogeneous microstructure in LMD processed Ti-6Al-4V samples, transverse grain boundaries to test direction act as a potential failure source. Therefore, a heat treatment at 845 °C for 2 hours is sufficient to increase the strain to failure for LMD processing [55].

In accordance with the previous studies in the literature, yield strength and elongation of additive manufactured Ti-6Al-4V alloy is summarized with ASTM F29224-14 standard in Figure 2.17 [35, 44, 45, 54 - 61]. Mechanical values of SLS specimen are given in hot isostatic pressed condition, because in literature HIP takes place as a regular treatment after SLS [56].

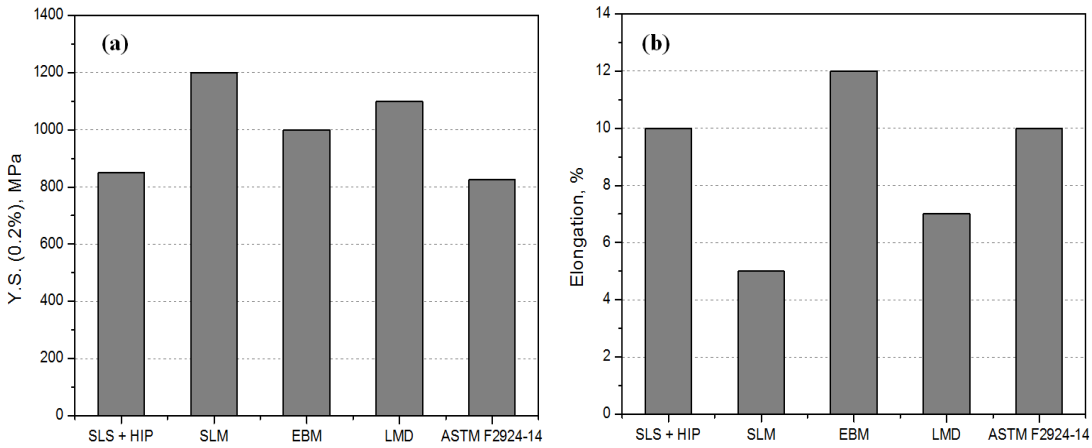

Figure 2. 17: (a) Yield strength at 0.2% offset, (b) elongation of additive manufactured Ti-6Al-4V [35, 44, 45, 54 - 61].

2.7. Heat Treatments Applied to Additively Manufactured Ti-6Al-4V Parts

In literature, various heat treatments are utilized for the additively manufactured Ti-6Al-4V parts, particularly for the ones that fabricated by laser based powder bed fusion (PBF) method since their instable microstructure is required to refine [69 - 71]. Restoring a homogeneous stable microstructure can be achieved without a heat treatment when directed energy deposition (DED) and electron beam used PBF methods are performed for the production of Ti-6Al-4V parts. However, as a result of rapid solidification and extremely localized heat inputs, a heat treatment is required in order to control the microstructure of laser based PBF fabricated parts [69 - 71].

The heat treatments of SLM produced parts were conducted in two different temperature strategies based on the study suggested by Vilaro et al [69]. They applied low temperature strategy such as annealing at 730 °C for 2 hours when stress relieving was essential without affecting the microstructure. The initial α' martensite phase was partially decomposed to α and β phases once the sample was cooled in the air to room temperature from 730 °C. The high temperature annealing strategy was done with the purpose of achieving high ductility. They held their specimens just

below the β transition temperature (980 °C) for 1 hour to avoid grain growth and consequently they obtained a final microstructure consisting of α and β grains. Moreover, they applied tempering treatments at the temperatures between 700-900 °C after samples water quenched from a temperature above the β transus (1000 °C). Vilaro et al. states that as the tempering temperature increases the hardness of the samples decrease subsequent to furnace cooling while higher temperature annealing leads to β grain growth in α matrix [69].

In Table 2.7, various heat treatments are shown along with their yield strength and elongation values according to the study suggested by Thöne et al. [70]. They performed several post processes to SLM fabricated initial Ti-6Al-4V samples so as to illustrate their mechanical responses after heat treatments made at different temperatures. It must be noted that all samples were furnace cooled subsequent to each heat treatment. The quasi-static tensile test results shown in Table 2.7 indicate the decreasing regime in the yield strength with increasing heat treatment temperature. Although the yield strength of as-received sample was decreased by 12.5%, the elongation of this sample was increased about 625% when a heat treatment utilized at 1050 °C for 2 hours. In this study, a comprehensive EBSD analysis which notices the increasing amount of β phase with increasing heat treatment temperature was also conducted [70].

Table 2. 7: The mechanical responses of the Ti-6Al-4V samples with increasing heat treatment temperatures [70].

	As-received	**1st sample**	**2nd sample**	**3rd sample**	**4th sample**	**5th sample**
Temperature (°C)	-	750	800	850	950	1050
Time (h)	-	2	2	2	2	2
Yield Strength (MPa)	1080	1062	1040	1009	972	945
Elongation (%)	1.6	3.7	5.1	5.2	10.1	11.6

The similar study indicating the effect of various heat treatments and cooling regimes on the final microstructure and mechanical properties were carried out by Vracken et al. [71]. In Table 2.8, the mechanical properties of SLM fabricated Ti-6Al-4V alloys are shown with different heat treatments. The fracture strain basically tended to increase with increasing heat treatment temperature when cooling was conducted in furnace. However, under the same circumstance, the yield strength was likely to decrease [71]. According to the microstructural observations made by Vracken et al, the 2 hours treatments carried out at 780, 843 and 1015 °C were resulted with decomposition of α and β phases from single α' phase following furnace cooling. With increasing treatment temperature α plate sizes become coarser than the treatments made at lower temperature [71].

Table 2. 8: Mechanical properties of heat treated Ti-6Al-4V SLM alloys [71]

Sample	**T (°C)**	**T (h)**	**Cooling**	**σ_y (MPa)**	**ε %**
1	540	5	WQ	1118	5.36
2	850	2	FC	955	12.84
3	850	5	FC	909	premature failure
4	1015	0.5	AC	801	13.45
	843	2	FC		
5	1020	2	FC	760	14.06
6	705	3	AC	1026	9.04
7	940	1	AC	899	13.59
	650	2	AC		
8	1015	0.5	AC	822	12.74
	730	2	AC		

2.8. Thermohydrogen Processing (THP)

A heat treatment is required for many AM processed Ti-6Al-4V in order to transform rapid cooling induced metastable martensite (α') to stable α + β phases and to reduce residual thermal stresses. HIPping and annealing at an elevated temperature are the mostly applied heat treatments to AM produced parts [60]. In this study, an alternative heat treatment for SLM produced Ti-6Al-4V was done with temporary alloying of hydrogen which is called as thermohydrogen processing (THP). Thermohydrogen treatment is usually applied cast and powder metallurgy Ti6Al4V alloys produced by conventional techniques. However, in the literature, THP has not applied to any of AM parts so far, therefore, the effect of THP is discussed on cast Ti-6Al-4V alloys.

2.8.1. Introduction to Thermohydrogen Processing

THP is a method in which hydrogen is used due to its positive impacts on the microstructure and the processing techniques including hot/cold working, machining, sintering and so on. Temporary hydrogen alloying of titanium alloys allows tailoring the microstructure and leads to improve the mechanical properties [72, 73].

Hydrogen is a β phase stabilizer interstitial element in titanium alloys and thus, with increasing hydrogen concentration, β phase transition temperature decreases, which allows the heat treatment at lower temperatures. Also increasing hydrogen content widens the α + β coexisting phase range where the hot working is done particularly for α titanium alloys (see Figure 2.20) [74 – 76]. Alloying titanium alloys with hydrogen, causes α phase softening and β phase strengthening [77]. Yoshimura et al. [74] have reported that the critical cooling rate to obtain martensite is decreased with addition of hydrogen, this property of alloying with hydrogen leads to an improving in hardenability. Hydrogen content can also be used for controlling the phase constituents and their specific volumes in titanium alloys [76].

There are two main steps in THP; hydrogenation and dehydrogenation. Hydrogenation step is done on the purpose of increasing hydrogen content which results the new phase distribution with finer grains in the microstructure. Presence of hydrogen prompts to an alteration in concentrations of other alloying elements within the phases that were present prior to hydrogenation. Once the novel microstructure is obtained, the hydrogen content must be lowered once again to avoid the future hydrogen embrittlement [78]. Since alloying of hydrogen is a reversible processing in titanium alloys, hydrogen removing can be utilized by using vacuum or inert gas environment at an elevated temperature. Consequently, when the alloy is dehydrogenated, the novel microstructure has been maintained and the mechanical properties have been improved as shown by several researchers [79 - 82].

2.8.2. Hydrogen Absorption of Ti-6Al-4V

The study made by Wasilewski et al. [83], suggested that the phenomena of hydrogen absorption is mainly related to the hydrogen concentration and hydrogenation temperature. Within this context, when Ti-6Al-4V is heated to a certain temperature in a hydrogen environment, hydrogen atoms start to diffuse until Ti-6Al-4V reaches a solubility limit at that temperature. Another important parameter that effect hydrogen solubility in Ti-6Al-4V is the hydrogenation pressure. The equilibrium hydrogen content is dependent on the hydrogenation temperature and pressure of the hydrogen environment [83]. Hydrogen absorption is a unique alloying technique for titanium alloys due to reversible property of the hydrogenation unlike oxidation and nitridation processes. Wasilewski et al. also proposed a hydrogen absorption rate equation depending on the variables of pressure and temperature:

$$\frac{d\omega}{dt} = c(p)^{0.5} \exp\left(\frac{-b}{T}\right) \qquad (2.1)$$

where; dω/dt is the hydrogen absorption rate, p is the hydrogenation pressure, T is the hydrogenation temperature, c and b are the constants [83].

The effect of hydrogenation temperature and pressure on hydrogen absorption is also studied by Zhang et al. [84]. In Figure 2.18, they illustrated that in 1 hour hydrogenation, the hydrogen content does not increased significantly when the hydrogenation temperature is below 400 °C; however, hydrogen absorption is drastically increased at 400 °C hydrogenation temperature. With increasing hydrogenation temperature the tendency of hydrogen absorption decreases continuously [84].

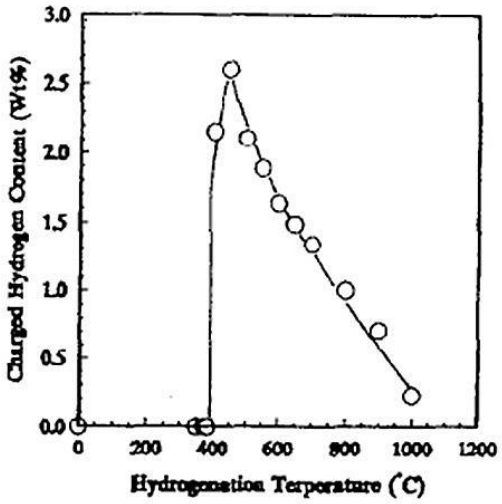

Figure 2. 18: Hydrogen content versus hydrogenation temperature diagram [84].

According to Zhang et al., Silvert's Law solves the solution of diatomic gas molecules in a metal. Silvert's Law; square root of the hydrogen pressure is proportional to the solubility of hydrogen in metal [84]:

$$C = k.P^{0.5} \qquad (2.2)$$

where; hydrogen concentration in a metal is C; hydrogen pressure is P; k coefficient related to hydrogenation temperature T and the heat Q.

$$k = k_0 \exp\left(\frac{-Q}{RT}\right) \qquad (2.3)$$

Substituting k in Equation 2.2 to Equation 2.3:

$$\log C = A - B/T, \qquad A = \log k_0 + 1/2 \log P, \qquad B = (Q/R).\log e \qquad (2.4)$$

From the Equation 2.4, a linear relationship between logC and 1/T is established. The solution heat Q is a negative value so that B is also negative. This reveals that with increasing hydrogenation temperature the absorption of hydrogen in Ti-6Al-4V decreases [84].

Similar to Zhang et al., in 2003, Lopez et al. was found maximum hydrogen absorption as 500 °C [85]. They used elastic recoil detection analysis (ERDA) to reveal the relationship between temperature and hydrogen absorption and basically they confirmed that hydrogen is not diffused until reaching up to 500 °C [85].

Another important parameter affecting the solubility of hydrogen is the hydrogen partial pressure of the environment which was studied by Manchester et al. [86]. Figure 2.19 illustrates the hydrogen partial pressure solubility curves for Ti-6Al-4V alloys. To keep concentration of dissolved hydrogen constant, partial pressure of the hydrogen gas should be changed with temperature. Hydrogen content in Ti-H system increases with increasing hydrogen pressure while the hydrogen absorption shows a decreasing regime with increasing temperature [86].

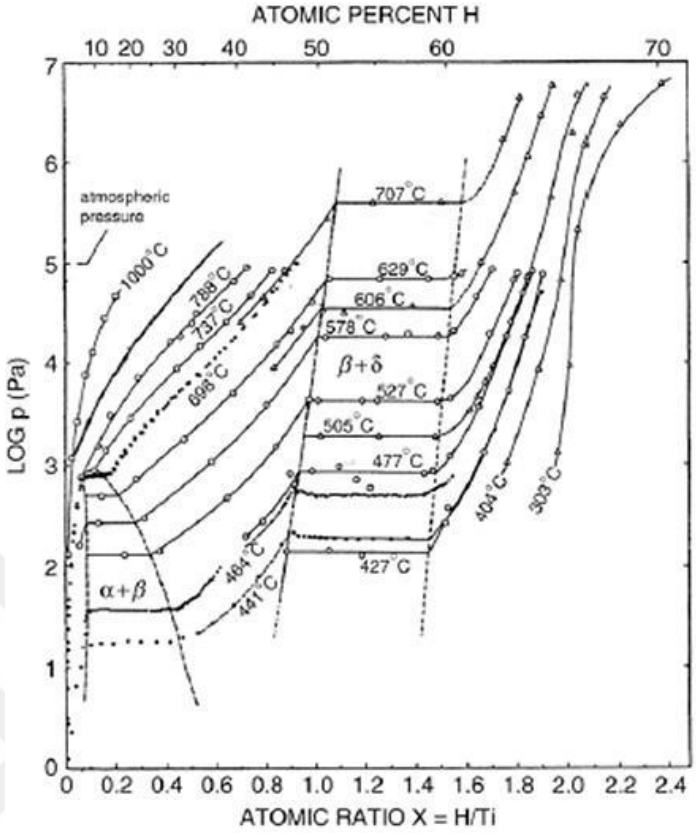

Figure 2. 19: Temperature vs pressure phase diagram for binary Ti-H system [86].

In Ti-6Al-4V, the β phase predominantly dissolves hydrogen since hydrogen atoms occupy tetrahedral interstitial sites. The bcc β phase has 6 octahedral and 12 tetrahedral sites while the α phase has only 2 octahedral and 4 tetrahedral sites. [87]. The diffusion coefficients of hydrogen for α and β phases were derived by Wasilewski et al. [83]:

$$D_{\beta} = 1.95x10^{-3} \exp\left[(-6640 \pm 500)/RT\right] \ cm^2/s \qquad (2.5)$$

$$D_{\alpha} = 1.8x10^{-2} \exp\left[(-12380 \pm 680)/RT\right] \ cm^2/s \qquad (2.6)$$

Where; R is the gas constant and T is the absolute temperature.

2.8.3. Hydrogen Induced Phase Boundaries

Ti-H Binary Phase System:

The Ti-H binary phase diagram shown in Figure 2.20 was suggested by San-Martin and Manchester [88]. The phase constituents of Ti-H system are hcp α titanium, bcc β titanium and δ titanium hydride. The δ phase has an fcc lattice with stoichiometric composition of TiH_2, where the hydrogen atoms occupying the tetrahedral sites [88]. Alloying pure titanium with hydrogen stabilizes the high temperature bcc β phase and decreases the β transition temperature from 882 °C to 300 °C at the eutectoid point. In addition, the presence of the hydrogen allows creation of α + β region [72]. At the eutectoid temperature, the hydrogen concentration in the α, β, and δ phases are 6.72 at.%, 39 at.%, and 51.9 at.%, respectively. The maximum hydrogen solubility in the α phase is only 6.72 at.%, while the terminal solubility at room temperature is about 0.04 at.%. The β phase can dissolve hydrogen up to 50 at.% above 600 °C [89, 90]. The presence of hydrogen in both solid solutions of α and β phases causes a lattice expansion. The volume increase in β phase is about 5.35 % when its maximum hydrogen solubility is reached [91]. On the other hand, 17.2% lattice expansion is resulted when α phase transforms to δ hydride phase. In such volume increase, high internal stresses might be followed by microcracks [92].

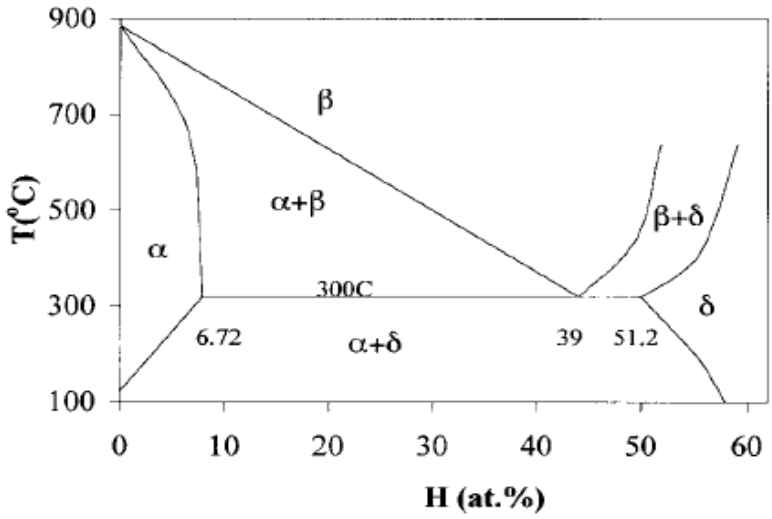

Figure 2. 20: The binary phase boundaries in Ti-H system [88].

Ti-6Al-4V-Hx Phase System:

In Figure 2.21 (a), the earliest phase diagram for Ti-6Al-4V-Hx system is shown which was suggested by William Kerr in 1985 [76]. Later on, Ilyn et al. [80] was proposed a new phase diagram, Figure 2.21 (b). Both authors agree on the point that a decrease in β transition temperature with increasing hydrogen content. However, these two authors disagree in their phase field definitions below the beta transition temperature. Kerr et al., refers a three phase region (α+β+δ) for 20 at.% hydrogen concentration and above. On the other hand, at the hydrogen concentrations between 0 at.% and 30 at.% Ilyn et al. proposes a two phase region (α+β) below the β transus. Besides, Ilyn et al. suggested that a three phase region (α+β+δ) is only stable below 300°C. In 2001, Qazi et al.[81], expanded Ti-6Al-4V-Hx phase system based on comprehensive XRD, optical microscopy and TEM analysis. Qazi et al. supported Kerr et al. with adding β+δ two phase region above the 15 at.% hydrogen concentrations between 800 and 900°C, their phase diagram is illustrated in Figure 2.21 (c).

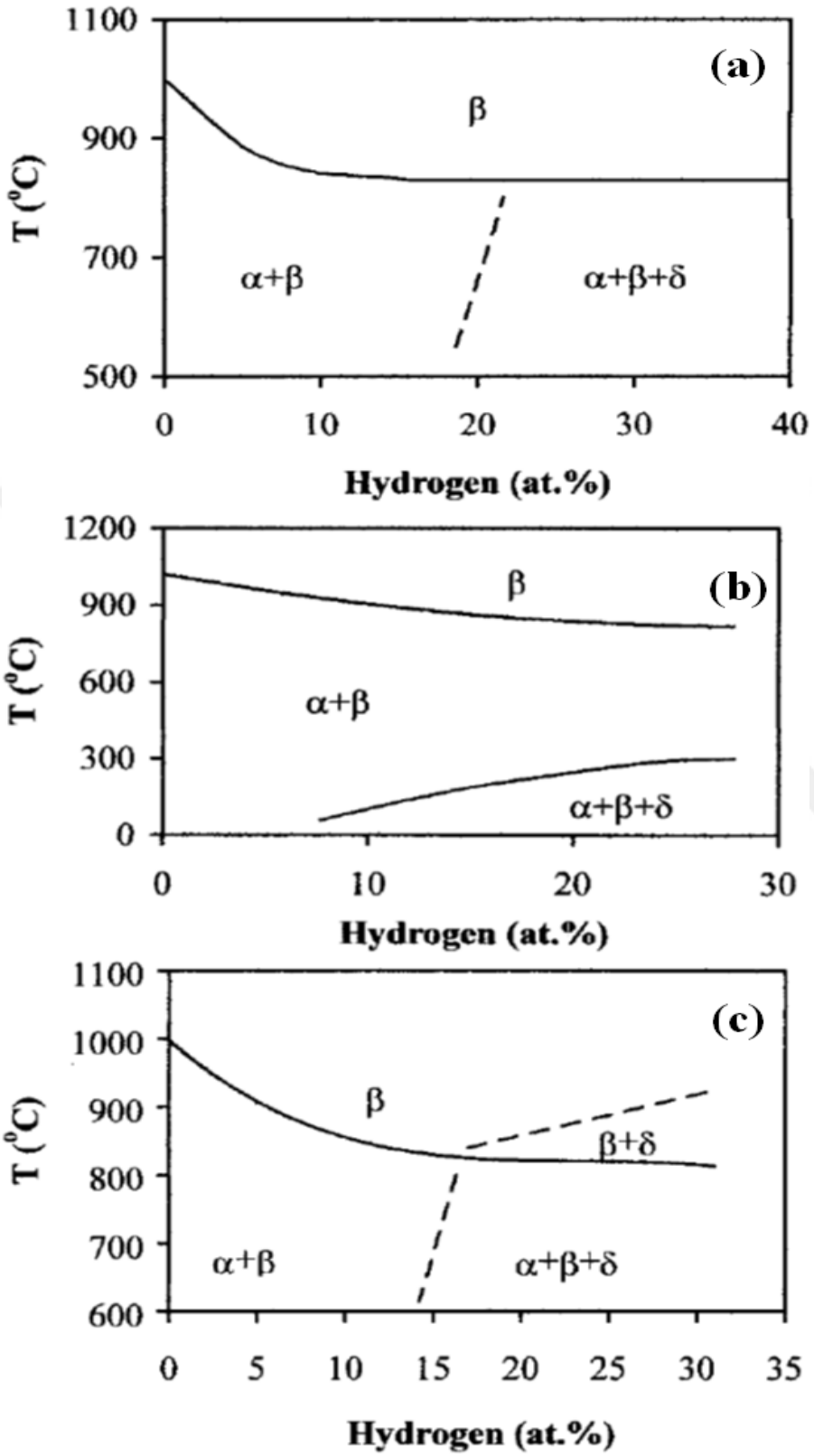

Figure 2. 21: The Ti-6Al-4V-Hx phase systems; (a) Kerr et al.[76], (b) Ilyn et al. [80], (c) Qazi et al.[81].

2.8.4. Microstructural Refinement by Using THP

Ti-6Al-4V alloy castings have coarse α and β lamellas in the Widmanstätten morphology. A subsequent heat treatment is required to as-cast Ti-6Al-4V parts on the purpose of refining the microstructure and leading to improvement in the mechanical properties. Conventionally mechanical properties of Ti-6Al-4V alloys are improved by hot working in α + β phase range [1]. However, such a method based on mechanical deformation is not applicable to the near net shaped complex parts. THP allows a refining in the microstructure without any mechanical deformation, therefore, this processing has been conducted by several authors [72, 93 - 96]. In Figure 2.22, as-cast lamellar and THP'ed fine microstructures are shown. White grains in optical micrographs correspond to the α phase in Figure 2.22 (a) and (b), while white grains represent the β phase in SEM images shown in Figure 2.22 (c) and (d). Because of THP, lamellar initial microstructure is transformed to one that has fine β precipitates in the α matrix.

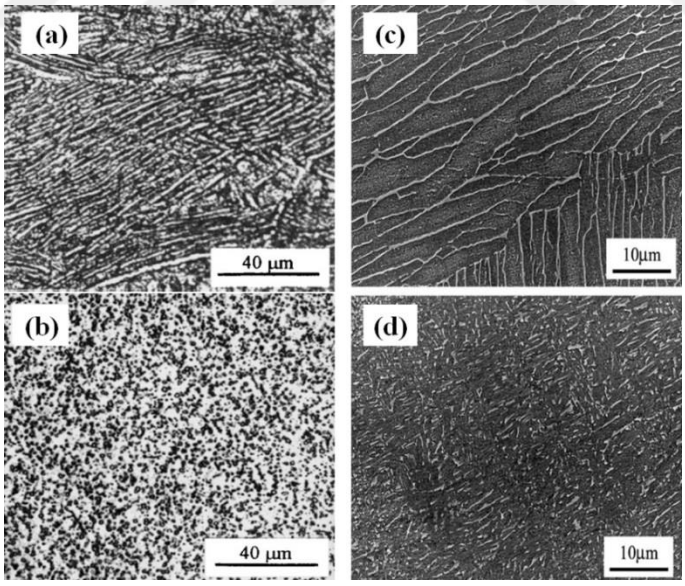

Figure 2. 22: Ti-6Al-4V microstructures of; (a) as-cast optical micrograph (OM), (b) OM after THP, (c) as-cast SEM image, (d) SEM image after THP [72, 93].

2.8.5. Refinement Mechanism of THP

There are several types of THP methods reported in literature including Hydrovac (HVC) and constitutional solution treatment (CST). Detailed information about these and other various THP methods can be reached from the study made by Oguh [97]. In today's commonly applied THP methods shown in Figure 2.23, as a first step treatment, hydrogen is usually absorbed by Ti-6Al-4V alloy at temperatures between 500-800 °C, which is below the β transition temperature.. A subsequent heating is done above the β transus to dissolve all phases in a single β phase containing dissolved hydrogen. The hydrogen treatment processes may differ depending on the cooling from β phase region. Difference between the methods shown in Figure 2.23 (a) and (b) is the cooling regime from β phase region. In the THP illustrated in Figure 2.23 (a) Ti-6Al-4V is slowly cooled to an isothermal eutectoid decomposition temperature in order to obtain fine α and δ precipitates in the primary β phase matrix in addition to β phase. However, second treatment shown in Figure 2.23 (b) contains water quenching to transform all microstructure to both hcp (α') and orthorhombic (α'') martensite before the aging step. In both methods a final dehydrogenation step is carried out to remove the hydrogen content and decompose the hydrides [82, 95, 98].

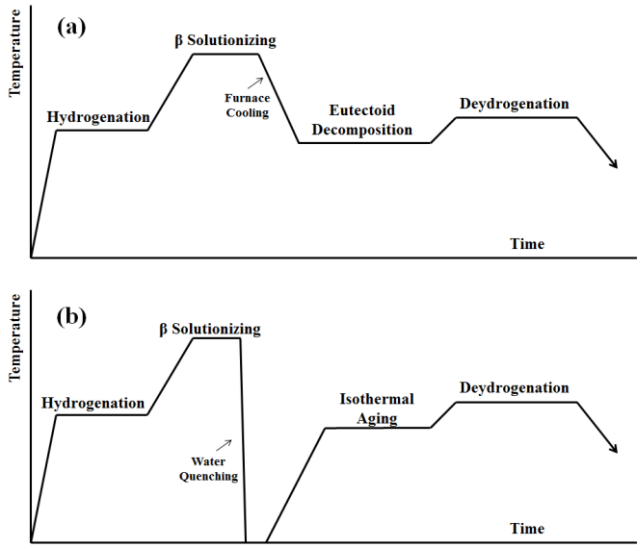

Figure 2. 23: THP methods; (a) eutectoid decomposition, (b) martensitic decomposition [82, 95].

Eutectoid Decomposition:

When a Ti-6Al-4V alloy is being hydrogenated, hydrogen atoms start to occupy tetrahedral interstitial sites in the α and the β phases. Gradually, formation of saturated α_H and β_H phases are occurred along with the further precipitation of δ hydride phase. Once the alloy is heated above the β transition temperature, which is lowered with addition of hydrogen, α_H and δ phases dissolve in β_H matrix, schematically shown in Figure 2.24 (a), [82, 99]. Fang et al, found that the full transformation to β_H phase is completed when the alloy, which has 2 mm thickness, is kept at 850 °C for 30 minutes [82]. After solutionizing treatment was completed the alloy is cooled slowly to a certain eutectoid decomposition temperature which has been figured out as 600 °C in the study made by Guitar et al [95]. Meanwhile α_H phase is formed at the primary β grain boundaries and interior parts of the grains, Figures 2.31 (b) and (c). Larger α_H plates diffuse at grain boundaries if the cooling rate is too slow [100, 101, 102]. At the eutectoid decomposition temperature, a significant amount of β_H phase transforms to α_H phase along with a slight content of β_H phase reside in the microstructure because of the vanadium element [103]. As Nelson et al. indicated, the maximum hydrogen solubility of α phase is 6.72 at. % and this solubility decreases continuously with decreasing temperature while the hydrogen solubility is about 50 at.% in β phase at 600 °C [90]. As long as more β_H transforms to α_H phase, hydrogen atoms distorts the α lattice thereby to eliminate the lattice distortion α_H phase separates into δ phase around the α grains, Figure 2.24 (d) and (e) [100, 101, 102]. The hydride precipitation results a volume expansion of about 17.2% leading to a volume misfit [92]. Shan et al. reported that this volume misfit causes a strain between hydride particles and surrounding matrix with following results [101]:

- Elastic and plastic deformation of the surrounding matrix,
- Hydride twinning,
- Strain induced martensite transformation.

The transformation from β_H to martensite can be obtained when the Ti-6Al-V-Hx alloy is cooled below the eutectoid temperature which is shown in Figure 2.24 (f).

The transformation of martensite can be either hcp α' or orthorhombic α" phase depending on hydrogen concentration [100].

The eutectoid decomposition treatment time must be long enough in order to obtain fine precipitates of α_H and δ hydride phases. For many authors decomposition of these phases is the main mechanism of the microstructural refinement [87, 82, 95, 99].

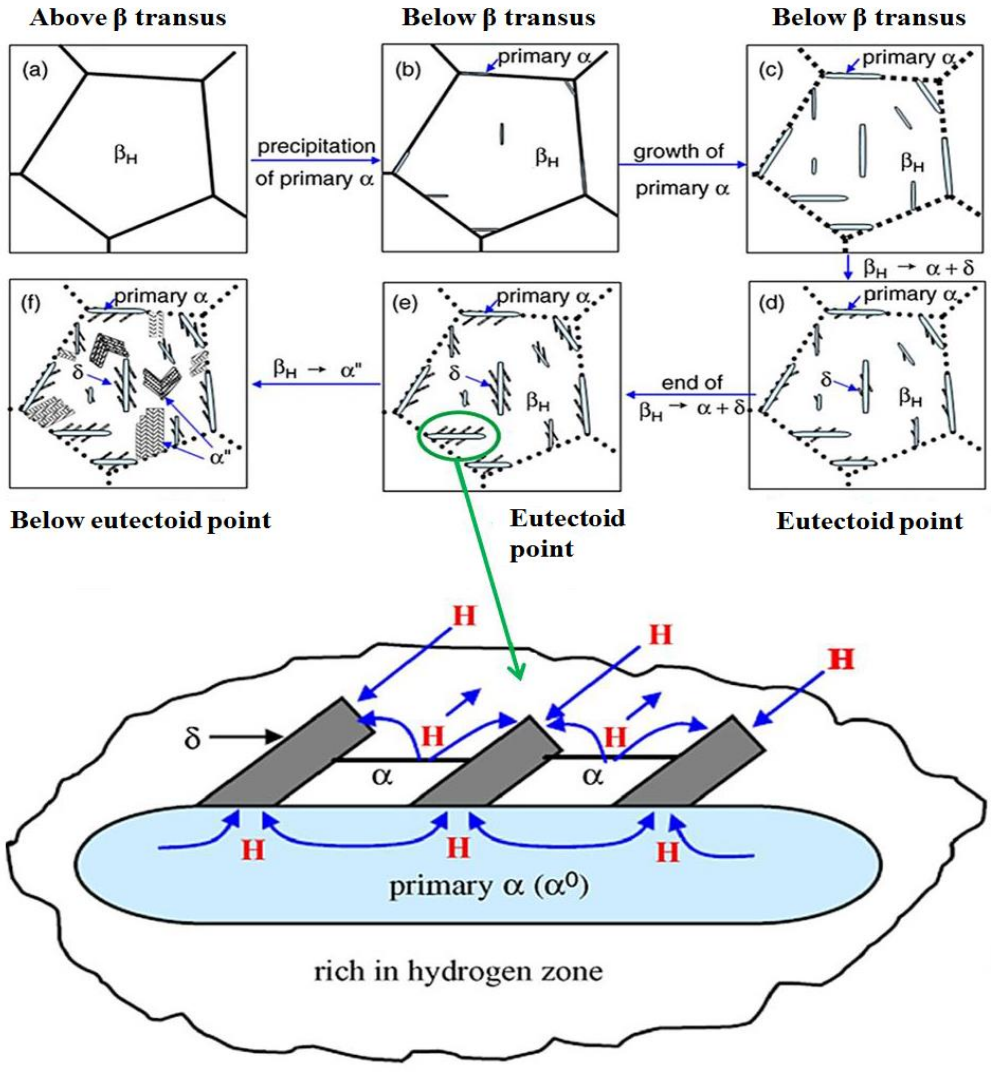

Figure 2. 24: Microstructural evaluation during eutectoid decomposition [100].

During the dehydrogenation step, hydrogen concentration is lowered because of the outward diffusion of hydrogen atoms in a vacuum chamber at an elevated

temperature. While hydrogen atoms are taken out from the structure, δ hydride decomposes to equilibrium α phase. Also α_H and β_H phases lose their hydrogen content by transforming fine, equiaxed α and β grains [82, 101, 104].

Decomposition of Martensite:

Qazi et al. [103] reported that addition of hydrogen to Ti-6Al-4V is slowed down the transformation kinetics of the β phase. The TTT diagrams in Figure 2.25 shows that the nose temperature decreases with increasing hydrogen concentration in the samples having 10, 20 and 30 at.% hydrogen contents, respectively. The following equation defines the relationship between the hydrogen concentration and the nose temperature for martensite decomposition with a regression coefficient of R^2=0.996.

$$T_N = 800 - 5.92C_H \qquad (2.7)$$

Where; T_N is the nose temperature (°C) and C_H is the hydrogen concentration (at.%) [103]. Mur et al. [105], found that when hydrogen content is increased from 0 at.% to 10 at.% the nose time for martensite decomposition increase from 6 seconds to 10 minutes.

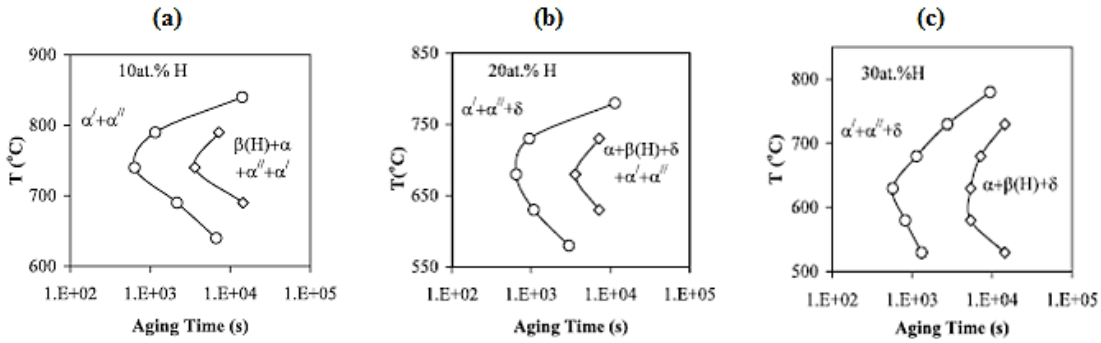

Figure 2. 25: Martensite decomposition diagrams for; (a) 10 at.% H, (b) 20 at.% H, (c) 30 at. %H [103].

Quenching from the β phase region results in formation of hcp α' and orthorhombic α" martensite phase mixture. The amount of α" martensite increases with increasing

hydrogen content upon quenching from the β phase field. The α' martensite only absorbs 5 at.% H, while the α" martensite has the ability of absorbing hydrogen about 36 at. %. The α" phase forms in Ti-6Al-4V when the alloy has high content of β phase stabilizer elements. On the other hand, the α' martensite decomposes in titanium alloys which has not been significant alloyed with β phase stabilizer elements (e.g. vanadium, hydrogen). These two martensite phases of α' and α" have different morphologies in microstructure due to their different lattice structures as shown in Figure 2.26. The α" martensite has wider needles whilst α' has thin and narrow ones [103].

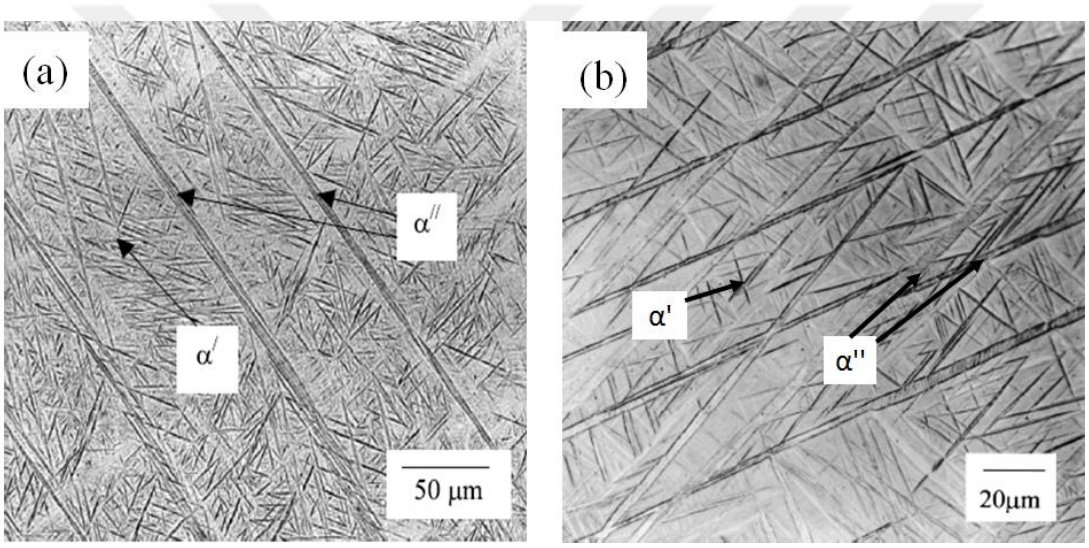

Figure 2. 26: Optical micrographs of Ti-6Al-4V having; (a) 10 at.% H, (b) 30 at.% H [103].

2.8.6. Hydrogen Effects on Hot Working

Hydrogen absorption increases ductility and decreases flow stress of the α phase along with lowering the β transition temperature. Decrease in the transformation temperature of softer and more deformable β phase allows usage of less amount of strain at relatively lower temperatures to deform the material plastically [106]. Kerr [76] reported that Ti-6Al-4V alloy shows 30% decrease in forging stress at 760 °C when hydrogenated with 16 at%. H. Many authors agree on the point that the flow

stress decreases, reaches a minimum value and then increases with continuous addition of hydrogen [81, 101, 107]. Figure 2.27 illustrates the hydrogen concentration dependency of stress values at different temperatures. The dotted line represents the β transition temperature which is shifted from 1253 K (980 °C) to 1023 K (750 °C) between 0 wt. % and 0.4 wt. % (≈0.15 at. %) hydrogen concentration[101]. From the diagram shown in Figure 2.27, it is remarkable that the hydrogen softening occurs until particular hydrogen content is reached for each hot deformation temperatures. Further hydrogen absorbing leads to hydrogen induced strengthening [101].

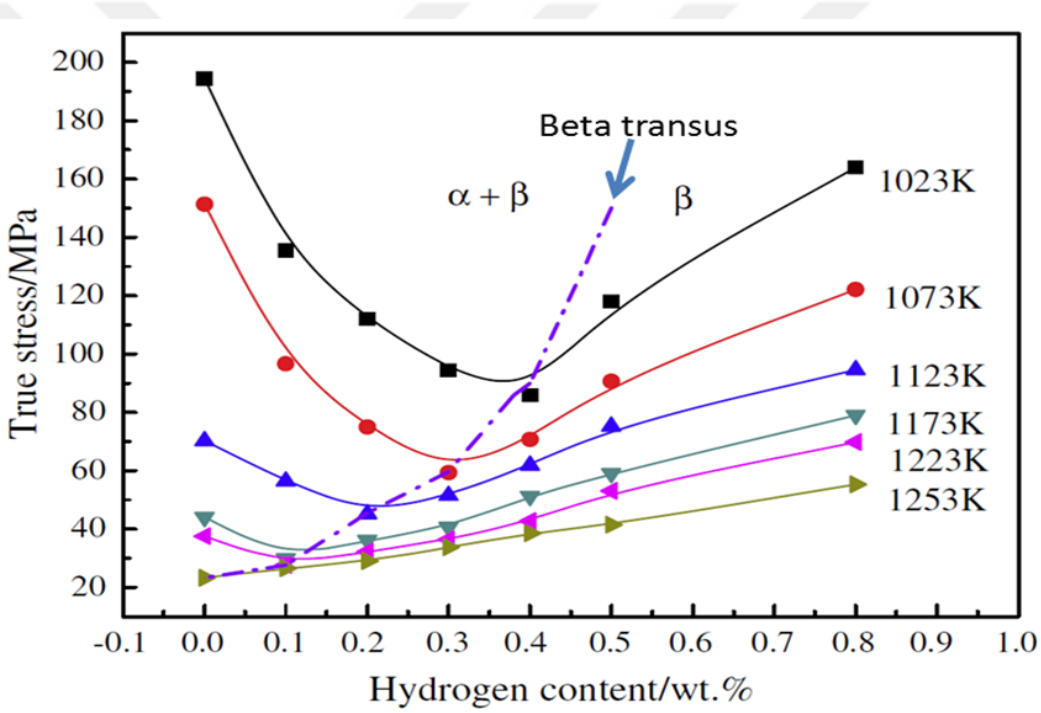

Figure 2. 27: Effect of hydrogen on hot working [101].

The reason of decreasing in flow stress with increasing hydrogen concentration is explained by the term of hydrogen induced softening of α phase [108]. In the α + β phase region, softening is associated with the combined effects of α phase softening and transformation to softer β phase. However, when hydrogen concentration is increased in the β phase region, β phase absorbs more hydrogen atoms and gradually diffusion of alloying elements is retarded in the matrix. This mechanism results the β phase hardening and reduces deformability [77].

CHAPTER 3

EXPERIMENTAL PROCEDURE

This chapter contains experimental procedures and techniques utilized during hydrogen processing and characterization of titanium alloys.

3.1. Starting Materials

In the present study, Ti-6Al-4V (grade 5) alloy specimens, which were previously produced by selective laser melting (SLM), were used as starting materials. The samples, supplied from 3D Systems Layerwise, Leuven, Belgium, were both in the form of cylindrical bars and tensile specimens in dog bone shape. Second set of as-received samples, supplied from SLM Solutions GmbH, Lübeck, Germany, was also used during THP. However, these samples were pressed in hot isostatic conditions (HIPped) after production with SLM. Shapes of the second set as-received samples were as same as with those which were produced by Layerwise.

SLM processing parameters were confidential; however, it has been known that parameters such as laser power, hatch spacing, scan velocity and the thickness between powder layers were kept the same to maintain volumetric energy density of 10.8 J/mm^3 for both samples produced by Layerwise and SLM Solutions companies. Average applied energy per unit volume during scanning of each layer gives the measure of volumetric energy density (E) [109].

$$E = \frac{P}{v\ t\ h} \tag{3.1}$$

where; P is the laser power ($J.s^{-1}$), ν is the scanning velocity ($mm.s^{-1}$), h (hatch spacing) is the distance between laser scanning lines (mm) and t is the powder layer thickness (mm).

To achieve a good surface quality and to produce high-density material, the layer thickness was kept as low as possible, around 30 μm. Spherical Ti-6Al-4V powders with average particle size of 30 μm were scanned in a zigzag pattern. Both as-received alloys were observed to meet chemical requirements of ASTM F2924-14 standard specification (Standard Specification for Additive Manufacturing Titanium - 6 Aluminum - 4 Vanadium with Powder Bed Fusion) as presented in Table 3.1.

Table 3. 1: Compositional analysis of as-received SLM and SLM + HIP fabricated Ti-6Al-4V alloy and ASTM F2924-14 standard specification.

Element	**Chemical Composition (wt. %)**		
	ASTM F2924-14	**SLM fabricated alloy**	**SLM + HIPped alloy**
Aluminum	5.50 to 6.75	6.13	5.97
Vanadium	3.50 to 4.50	4.03	4.16
Iron	0.30 max.	0.27	0.23
Oxygen	0.20 max.	0.15	0.12
Carbon	0.08 max.	0.076	0.044
Nitrogen	0.05 max.	0.042	0.036
Hydrogen	0.015 max.	0.0042	0.0139
Titanium	Balance	Balance	Balance

Both types of SLM fabricated Ti-6Al-4V alloys were cut into 2 mm thick disks from the bars having 50 mm length and 10 mm diameter in order to make microstructural analysis. The as-received SLM fabricated alloy had a fine microstructure containing acicular α' martensite phase as shown in Figure 3.1 (a) and (b). Due to large thermal

inputs and rapid solidification experienced during SLM, formation of non-equilibrium α' was observed instead of duplex microstructure composed of α + β phases in relatively slowly cooled Ti-6Al-4V alloys and the density of this alloy was measured as 4.40 gr/cm^3. On the other hand, second set of SLM fabricated + HIPped samples of which HIP parameters are presented in Table 3.2, were observed to contain lamellar structure composed of α and β phases, Figure 3.2 (a) and (b). The density of HIPped alloy was found as 4.42 gr/cm^3.

XRD spectrum of both types of as-received samples shown in Figure 3.3 also verify the presence of non-equilibrium hcp α' phase and equilibrium α and β phases shown in Figures 3.1 and 3.2.

Table 3. 2: HIP parameters of Ti-6Al-4V alloy produced by SLM.

Material	Temperature	Time	Pressure
Ti-6Al-4V alloy	920°C	2hr	1000bar

In order to optimize the mechanical properties of SLM fabricated components acicular α' phase containing microstructure must be turned into refined microstructure containing α + β phases with various post processing heat treatments which will be discussed in results chapter.

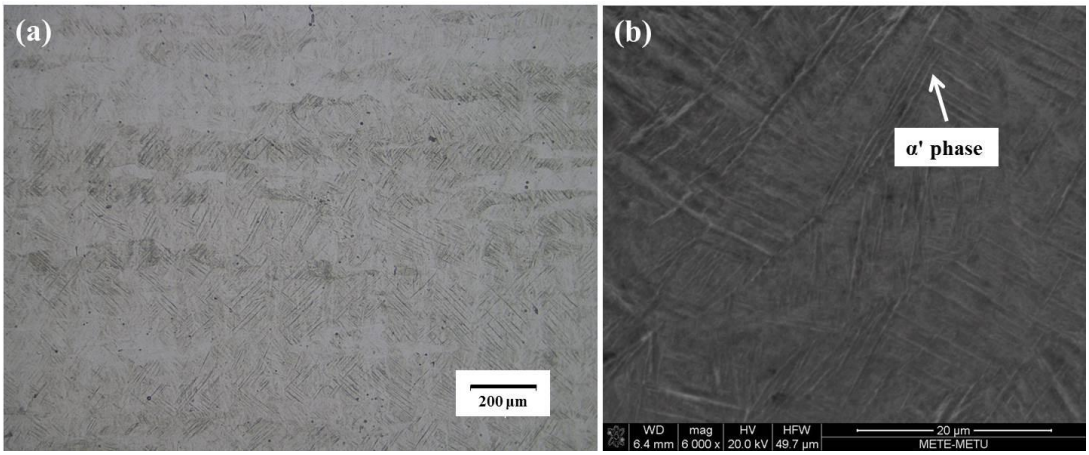

Figure 3. 1: Images illustrating microstructures of SLM as-received samples (a) optical micrograph (b) SEM.

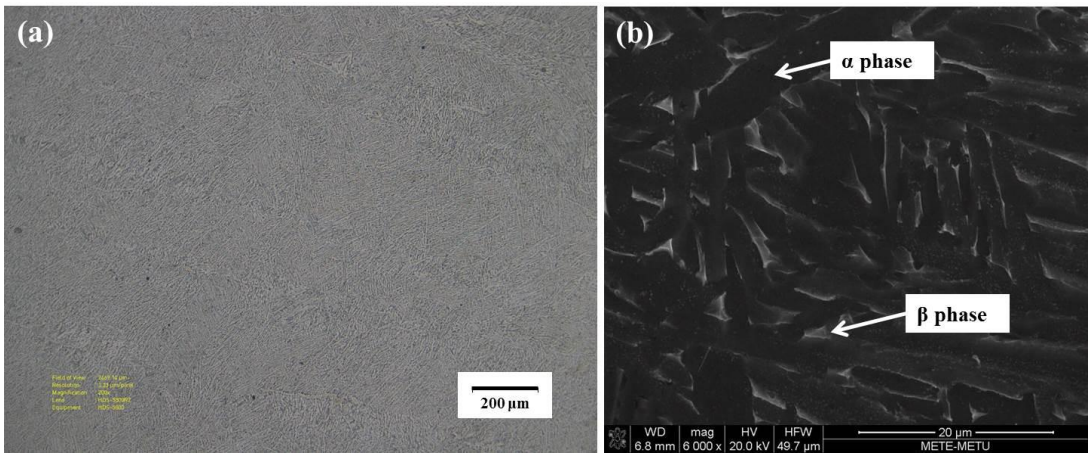

Figure 3. 2: Images illustrating microstructures of SLM +HIPed as-received samples (a) optical micrograph (b) SEM.

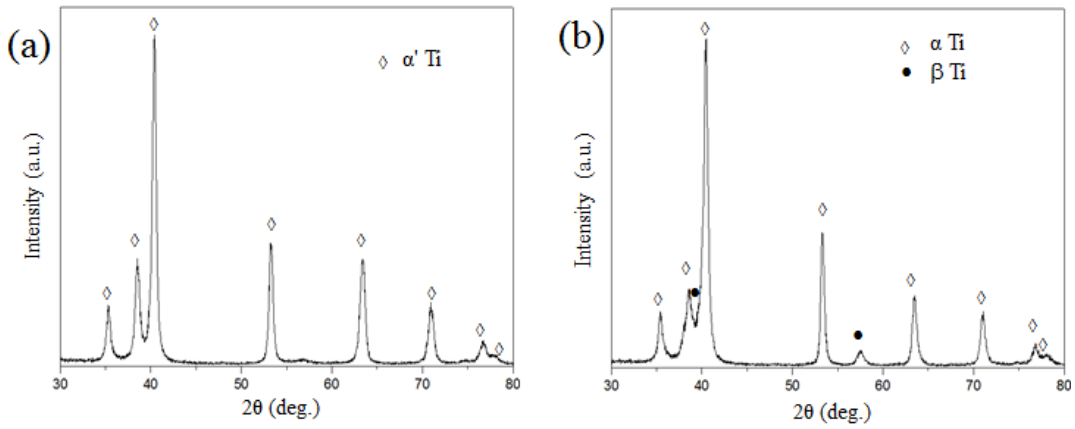

Figure 3. 3: XRD patterns of as-received samples (a) SLM fabricated (b) SLM fabricated + HIPped.

3.2. Thermochemical Processing (TCP)

Thermochemical processing (TCP) is a technique used to modify the microstructure for tuning the mechanical properties in titanium alloys. In our study, due to the reversible alloying property of hydrogen in Ti-6Al-4V, phase transformations in the alloy system were studied in hydrogen atmosphere at elevated temperatures. Thermochemical process including hydrogen treatment with the aim of adding

and/or removal of hydrogen from the alloy is known as thermohydrogen processing (THP) [82]. Commonly used THP includes various steps conducted at different temperatures such as hydrogenation treatment, β solution treatment, eutectoid decomposition and elevated temperature vacuum dehydrogenation as illustrated in Figure 3.4(a). A different type of THP (Figure 3.4(b)), which consists of only two steps including hydrogenation and dehydrogenation treatments, was also conducted as a part of the study. Purity and surface condition (i.e. presence of oxides) of the as-received alloy determine the processing temperature and the duration of each step. Therefore, optimum processing variables, i.e. temperature and time of each step, were initially determined to obtain desired microstructure.

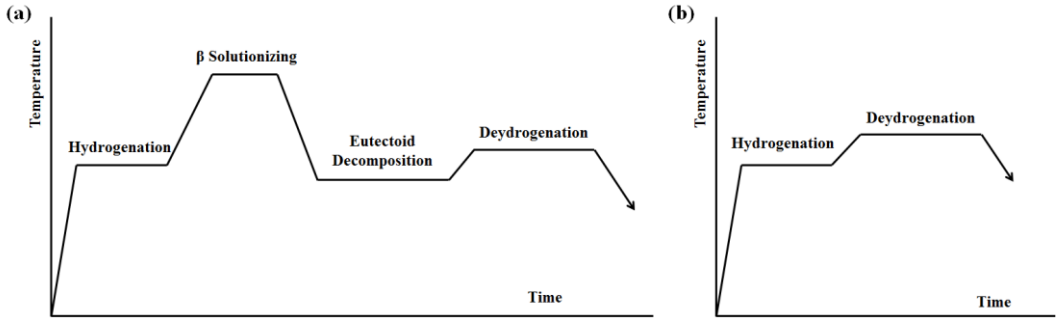

Figure 3. 4: THP treatments with; (a) 4 steps, (b) 2 steps.

3.2.1. Sample Preparation for TCP

Before SLM fabricated Ti-6Al-4V specimens were charged into the furnace, disk samples, 10 mm in diameter and 2 mm in length, had been cut precisely from cylindrical 3D-printed bars having 10 mm diameter and 50 mm length. Then, both sides of the samples were ground with SiC papers to remove possible surface contamination and oxide layer that may be an obstacle during hydrogen penetration and dehydrogenation. Subsequently, following cleaning cycles were performed in an ultrasonic bath;

1. Soaking in distillated water for 10 minutes,
2. Acetone bath for 15 minutes,
3. Immersing into ethanol and keeping for 15 minutes,
4. Cleaning with distillated water for 15 minutes.

Ultrasonically cleaned specimens were then charged into the furnace right after they were dried in warm air.

3.2.2. Hydrogenation Process

Hydrogenation treatments were done to get information about the temperature dependent hydrogen solubility of the specimens at constant pressure.
Before starting the hydrogenation treatment, the test pieces were placed into furnace at room temperature. Next, the horizontal furnace shown in "3.3.1. Hydrogenation System" underwent a vacuum approximately 10^{-5} torr. Next, the furnace was filled with high purity argon gas (99.999% purity, N_2: 6.2 volume per million (vpm), O_2: 2.2 vpm, humidity: 2vpm) to create an inert environment. Subsequent to repeating two vacuum and argon purging cycles, the furnace was heated under flowing argon (0.30 lt/min) gas environment up to certain hydrogenation temperatures between 550 and 850 °C with 50 °C intervals.

When the furnace reached to targeted temperatures, hydrogenation temperatures, a flowing gas mixture containing 25 vol. % hydrogen and 75 % vol. argon gases was fed to the furnace (0.07 lt/min H and 0.21 lt./min. Ar). After keeping the samples for 1 hour at each hydrogenation temperature under gas mixture, the furnace was switched-off to cool down to room temperature naturally (10°C/min) under high purity argon gas flow. The gas pressure inside the furnace was kept constant at 2.64 atm . The method of pressure calculation is also presented in Appendix A section.

3.2.3. β Solutionizing Process

After hydrogenation step for 1 h, the sample was heated up to a solutionizing temperature with a heating rate of 10°C/min and under the same flowing gas mixture used in hydrogenation step (25 vol. % H_2 and 75 vol. % Ar). In this step, heating in β phase region shown in Ti-6Al-4V-Hx phase diagram (Figure 2.21) has a major importance to obtain 100 % β phase for accomplishing subsequent homogenous eutectoid decomposition. Therefore, specimens were held at 800, 850 and 900 °C for 15 minutes to determine the temperature for 100 % β formation by the examination of subsequent transformation upon cooling. After betatizing treatment, all the samples were cooled down to room temperature under argon gas flow with a cooling rate of 10 °C/min.

3.2.4. Eutectoid Decomposition Process

In order to obtain fine microstructure consisting of equiaxed α, β and δ phases, a certain cooling rate is required during cooling from β-phase region. According to the study made by Qazi et al., increasing hydrogen content favors the martensitic decomposition with lowering the nose temperature and increasing the aging time in Ti-6Al-4V alloy which previously shown in Figure 2.25 [103]. The cooling rate from β-phase region should be neither high enough to allow martensitic transformation nor slow to cause grain boundary α-phase formation [101]. Therefore, to avoid both α phase diffusion at grain boundaries and martensitic decomposition, eutectoid decomposition temperature was selected as 600 °C with respect to the previous studies [95]. After 100 % β phase at β-solutionizing step, the furnace was continuously cooled down to 600 °C with a 10 °C/min cooling rate under the same hydrogen/argon gas mixture and it was held at this temperature for 3 hours. Eutectoid decomposition temperature must be long enough to allow decomposition of δ phase [82]. In this step, hydrogen charging was continuously maintained to provide precipitation of δ phase along with α and β phases.

3.2.5. Dehydrogenation Process

Specimens were underwent a vacuum dehydrogenation at an elevated temperature in order to allow transformation of δ phase to fine α phase.. Besides, hydrogen content must be lowered due to avoid hydrogen embrittlement and to provide the ductility. In this step, the aim is to lower the residual hydrogen content and to obtain fine microstructure consisting of equiaxed α + β grains. Due to the higher mobility of hydrogen atoms at higher temperatures, the outward diffusion rate is higher at elevated temperatures [104]. Therefore, various dehydrogenation treatments were applied to observe the impact of time and temperature on hydrogen removal and subsequent microstructure change. After hydrogenation, specimens were heat-treated at constant temperatures 600, 700 and 800 °C for 6, 18 and 24 hours. Around 10^{-5} torr vacuum level was maintained throughout the dehydrogenation step with help of a turbo-molecular vacuum pump, which is shown in Figure 3.6. At the end of elevated temperature dehydrogenation step, the heating furnace was cooled down to room temperature while vacuum pump was still operating.

3.3. Experimental Set-Up

In order to perform safe and effective hydrogenation and dehydrogenation treatments for Ti-6Al-4V samples, a THP apparatus was designed precisely to fulfill safety and THP requirements. All of the components of THP apparatus were consistently sealed from the external environment to prevent possible hydrogen or oxygen leakages from furnace or surrounding air environment.

3.3.1. Hydrogenation System

To hydrogenate the samples, a completely isolated THP system was used. The system had the capability of allowing controlled gas flow, analyzing residual gases and maintaining positive gas pressure inside the furnace. 1000 mm long quartz tube

having 50 mm internal diameter was mounted into a horizontal furnace. To ensure a successful hydrogenation, it is ultimately important to isolate the quartz tube from external environment. In this context, high temperature o-ring supported flanges with cooling fans above were attached to both left and right hand ends of the quartz tube. The temperature of the hydrogenation was measured with a K-type thermocouple placed just over the sample in the hot zone of the furnace. The layout of the heating furnace system is shown in Figure 3.5.

Figure 3. 5: (a) Photos of the heating furnace and the quartz tube; (b) Right hand-end enclosure flange.

At a particular temperature, the diffusion of hydrogen into Ti-6Al-4V alloy is very sensitive to the hydrogen flow rate and the partial pressure. Therefore, digital flow meters, shown in Figure 3.6, were used to maintain 25 vol. % hydrogen + 75 vol. % argon during THP. Additionally, purging via argon gas before reaching hydrogenation temperature was controlled by the argon gas digital flow meter.

Figure 3. 6: A photo of the digital flow meter

3.3.2. Dehydrogenation System

The desired vacuum level during dehydrogenation step was attained by using a turbo-molecular vacuum pump (Nano-Vak, Turkey), Figure 3.7, capable of reaching down to 10^{-9} torr.

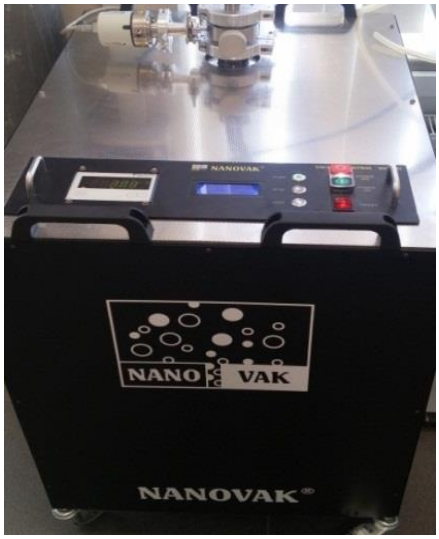

Figure 3. 7: A photo of the vacuum system consisting of rotary and turbo-molecular pump.

3.3.3. Other Components Required for THP

Various linking components were used to carry hydrogen/argon gas mixture in and out of the furnace and they used as connectors/flanges in furnace and vacuum system. The following additional components are required to ensure a safe THP as shown in Figure 3.8;

- A valve attached to outlet of the turbomolecular vacuum pump which is used for interrupting the vacuum,
- A stainless steel hose between quartz tube and turbomolecular vacuum pump,
- A residual gas analyzer (RGA) to perform kinetic measurements via outgassing differences in vacuum environment,
- A gas controlling valve that makes connection between the flow meter and rest of the system,
- A gas outlet valve used under positive pressure to ensure the escape of hydrogen and argon gases,
- A vacuum gauge that detects the vacuum in front of the quartz tube,
- 9 pieces o-ring and ring-joint gasket set for connection of stainless steel parts,
- Manually adjustable supporting legs to carry the quartz tube and installed flanges.

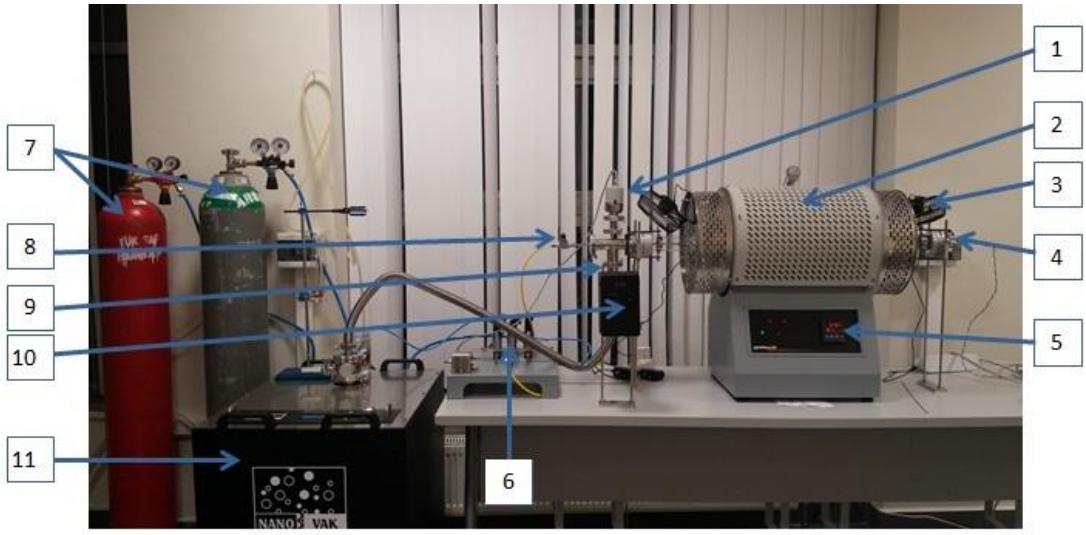

1- Vacuum Gauge
2- Heating Furnace
3- Cooling Fan
4- Sample Holder Enclosure
5- Furnace Option Display
6- Flow Meter
7- Argon and Hydrogen Source
8- Gas Inlet Valve
9- Gas Outlet Valve
10- RGA
11- Vacuum Pump

Figure 3. 8: Complete layout of the THP experimental set-up.

3.3.4. Safety Precautions

Some safety precautions are essential to prevent potential accidents and destructions since hydrogen is explosive and flammable at higher temperatures and pressures when in direct contact with air. A copper-coiled cooling system was directly attached to the outgassing valve of the system so as to ensure the critical temperature drop before hydrogen escapes to the atmosphere. A high precision hydrogen alarm device is very useful to detect hydrogen leakages and for warning to prevent potential destructions.

3.4. Characterization

Several characterization techniques were done on both as-received and THP treated specimens. This section gives detailed information about all of the experimental techniques used for characterization of samples.

3.4.1. Chemical Composition Analysis

Elemental Analysis

Inductively coupled plasma optical emission spectroscope (ICP-OES) "Perkin Elmer Optima 4300DV" device was used in order to measure elemental composition of the SLM produced Ti-6Al-4V as-received bars. This technique mainly based on the emission of photons from atoms and ions that have been excited using argon plasma. The plasma has high temperature (10000 K) and high electron density to excite the atoms. When excited atoms reach to low energy position, corresponding emission rays (spectrum rays) of the photon wavelength are measured. While the element type analysis is done with respect to position of the photon rays released from the excited atoms, the element content is determined based on the photon rays intensity. Bulk Ti-6Al-4V specimens were required to extraction or acid digestion so as to present in solution. Averages of three ICP-OES measurements were taken to calculate elemental analysis results.

O, H, N, C Contents

Quantitative analysis of elements ranging from ppm to weight percent levels, especially hydrogen, is crucial for evaluation of the success of THP. Therefore, oxygen, nitrogen and hydrogen contents of as-received, hydrogen treated and dehydrogenated Ti-6Al-4V alloys were determined with LECO TCH600 using IR and thermal conductivity. On the other hand, the carbon content determination was carried out with LECO CS230 using combustion method.

3.4.2. Metallographic Examinations

For metallographic examination, specimens were firstly mechanically ground using SiC papers up to 2000 grit sizes to prepare smoother surfaces and to remove possible oxide layer. Subsequently, samples were polished using polishing diamond pastes containing 6, 3 and 1 μm size diamond particles. Next, polished specimens were dip etched for 15-30 seconds in Kroll's Reagent (Table 3.3).

Table 3. 3: The components of Kroll's reagent.

Components	Volume
Hydrogen fluoride (HF)	10 ml
Nitric acid (HNO_3)	5 ml
Distillated water (H_2O)	85 ml

After etching, surfaces of the specimens were rinsed with water and ethanol. Finally, the specimens were dried in hot air.

Microstructural examination was carried out using both Huvitz HDS-5800 digital micrograph and scanning electron microscopy (SEM). Topographical and quantitative examinations in SEM were carried out using FEI 430 Nano Scanning Electron Microscope equipped with an energy dispersive X-ray spectroscopy (EDS) analysis system.

3.4.3. X-Ray Diffraction (XRD)

X-ray diffraction (XRD) was carried out to examine the differences between phase constituents of the as-received, the hydrogenated and the dehydrogenated test pieces. All specimens were ground using SiC papers prior to XRD analysis. XRD was

performed using a Bruker D8 Advance Eco X-Ray Diffractometer supplying CuKα radiation. The scanning measurements were done under the following conditions: The 2θ scan angle between 25° and 85°,

- The continuous x-ray generator scanned at 40kV,
- Scan speed was fixed at 0.5°/min.

3.4.4. Mechanical Characterization

Microhardness Measurements

The Shimadzu HMV-2T microhardness device was utilized at a load of 500 g for 20 seconds to determine the Vickers hardnesses of the specimens. At least 15 measurements were done for each sample.

Tensile and Compression Tests

Two kinds of dumbbell shaped SLM fabricated tensile test specimens were used to perform tensile tests. On the other hand, compression test samples having height/diameter ratios of 1.5, which were cut from SLM fabricated bars, were used during quasi-static compression tests. The dimensions of the tensile bars and the compressive test samples were as follows:

- Compression test specimen: 6 mm height and 4 mm diameter (Figure 3.9(a))
- 1st type of tensile specimen: 30 mm gage length, 6 mm diameter and 20 mm in both ends to fix the specimen to the holding grips. (Figure 3.9(b)), Figure 3.10(a))
- 2nd type of tensile specimen: 16 mm gage length, 2.5 mm diameter and 20 mm in both ends to fix the specimen to the holding grips. (Figure 3.10(b))

The 100 kN capacity Instron 5582 Universal Testing Machine equipped with the Instron 2663-821 video extensometer device was used with a constant cross head speed of 0.5 mm min^{-1} to determine the stress-strain behavior during both tensile and compression testing.

Both tensile and compressive yield strengths were determined by using 0.2% offset method. Elastic modulus of the specimens was calculated from the slopes of the linear regions of the stress-strain diagram.

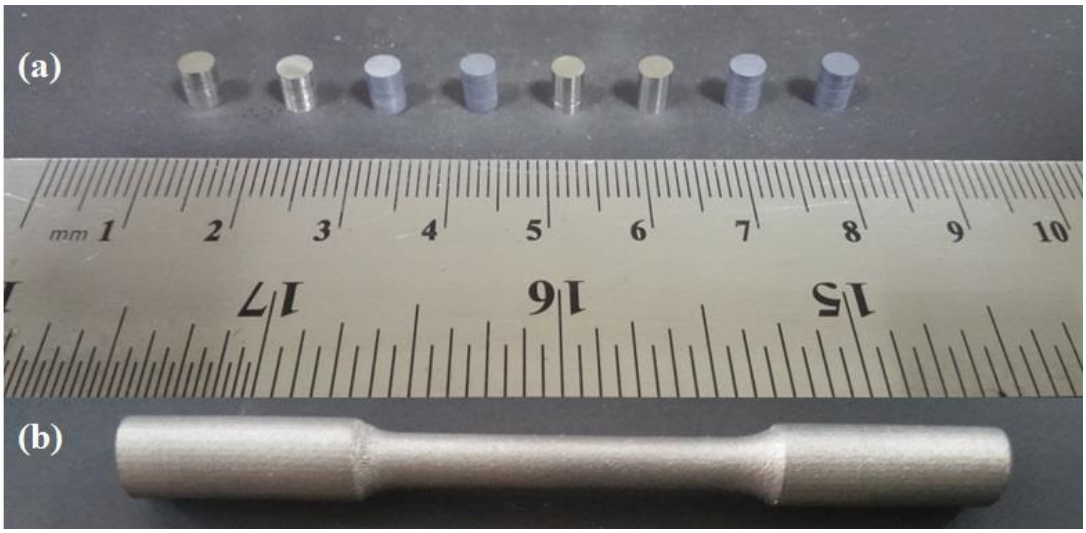

Figure 3. 9: Photos of the; (a) compression test specimens, (b) tensile test specimen.

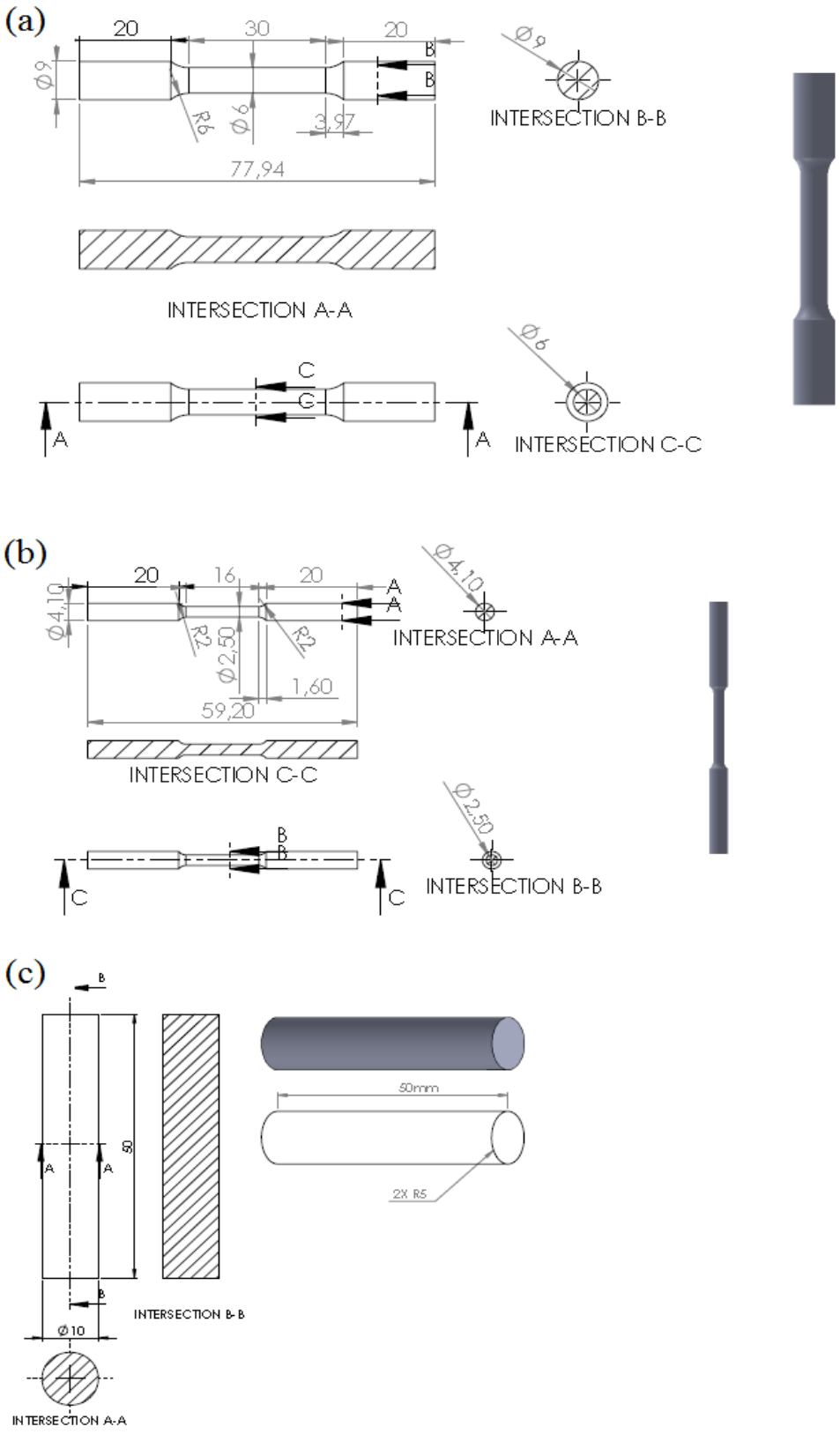

Figure 3. 10: Drawings of; (a) 1st type tensile test, (b) 2nd type tensile test, (c) type 3 specimens.

3.4.5. Other Characterization Techniques

Density Measurement

Density and porosity measurements of SLM fabricated as-received specimens were done according to Archimedes' principle. For density evaluation xylol solution ($CH_3C_6H_4CH_3$) with a density of 0.861 g/cm^3 was used by PRECISA XB220A balance with a density measurement kit. The specimens were firstly weighed in air and then dipped into xylol for 24 hours to allow impregnation of xylol into open pores. Subsequently, specimens were replaced to another container filled with xylol and weighed when they were in the solution. Then, specimens were weighed in air right after they had been taken out of the solution. Densities and porosities of the samples were calculated using equations 3.4-3.8.

$$V_{specimen} = \frac{\left(m_{s,a/x} - m_{s,x/x} \right)}{\rho_x} \tag{3.4}$$

$$\rho_{specimen} = \frac{m_{s,a}}{V_{specimen}} \tag{3.5}$$

$$P\%(total) = \left(100 - \left(\frac{\rho_{specimen}}{\rho_{Ti6Al4V}} \right) \times 100 \right) \tag{3.6}$$

$$P\%(open) = \frac{\text{Volume of xylol in pores}}{V(specimen)} = \frac{\left(\frac{m_{s,a/x} - m_{s,a}}{0.861} \right)}{V(specimen)} \tag{3.7}$$

$$P\%(closed) = P\%(total) - P\%(open) \tag{3.8}$$

where;

$m_{s,a/x}$: Mass of the xylol impregnated specimen in air

$m_{s,x/x}$: Mass of the xylol impregnated specimen in xylol

$m_{s,a}$: Mass of the dry specimen in air

P% (total) : Percentage of the total porosity

P% (closed) : Percentage of the closed porosity

P% (open) : Percentage of the open porosity

$\rho_{xylol} = 0.861 \ \ gr/cm^3$

$\rho_{Ti6Al4V} = \text{density of wrought Ti6Al4V alloy } (4.43 \ \ gr/cm^3)$

CHAPTER 4

RESULTS AND DISCUSSION

4.1. Introduction

In this chapter, the experimental findings of hydrogen content measurements, structural analyses, microstructural evaluations and mechanical property examinations and discussions are given in detail. The effect of hydrogenation and dehydrogenation steps on microstructural evolution of SLM fabricated Ti-6Al-4V alloy is also presented.

As presented in experimental section, two different THP treatments (4 steps and 2 steps) were performed to SLM and SLM+HIP fabricated specimens. First type of THP was conducted in 4 steps as referred by Fang et al. [82]. In this treatment, firstly, hydrogenation treatments were applied to samples to determine the maximum hydrogen absorption temperature. Next, prior to dehydrogenation step, specimens were undergone several treatments such as solutionizing so as to get 100% β-phase and eutectoid decomposition to allow hcp-α and TiH_2, δ phase transformation from β-phase. Finally, hydrogen contents of the samples were reduced to desired level according to ASTM F2924 standard for refinement of the microstructure via $\delta \rightarrow \alpha$ phase transformation. In the second type of THP, the treatment was done only in two steps, namely, hydrogenation and dehydrogenation. In 2-step process solutionizing and subsequent eutectoid decomposition treatments were eliminated to overcome β-phase grain growth problem. The mechanical behavior of thermo hydrogen processed (THP) alloys were investigated by using hardness testing, and quasi-static tensile and compression tests to reveal the

differences between mechanical responses of SLM and SLM+HIP processed samples which were undergone 2- and 4-steps THP.

Initially, in this chapter, hydrogen contents and phase evolution by XRD during hydrogenation and dehydrogenation processes of 4- and 2-step THP treatments were presented. Next, the microstructural evolution at each step of 4- and 2-step THP treatments was examined. Finally, the work about investigating the structure-property relation by mechanical testing was given.

4.2. Chemical Composition

4.2.1. Hydrogen Content After Hydrogenation Treatment

Ti-6Al-4V specimens were kept under flowing hydrogen and argon (25% H_2 + 75% Ar) gas mixture at a constant pressure and temperatures. Figure 4.1 and Table 4.1 illustrates the LECO hydrogen contents of specimens after hydrogenation treatments at various temperatures for 1 hour. At least three hydrogen content measurements were done for each sample in order to get accurate results.

The hydrogen concentrations of as-received samples were measured as 0.0042 wt. % and 0.0139 wt. % for SLM fabricated and SLM+HIPped samples, respectively. The responses of two samples to hydrogen containing atmosphere were more or less the same such that they displayed similar hydrogen solubility at various temperatures.

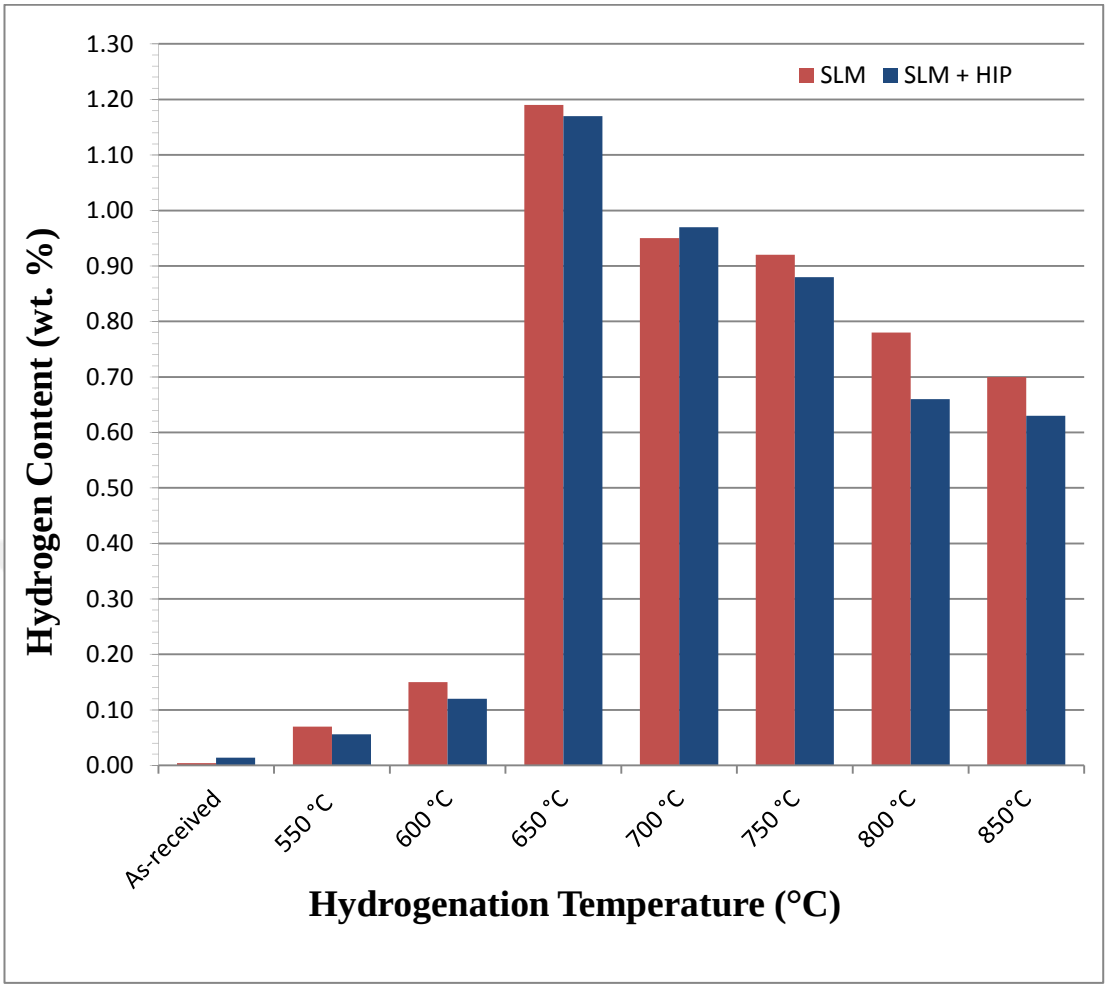

Figure 4. 1: Hydrogen contents of hydrogenated samples.

Hydrogen measurements have shown that temperature dependent hydrogen solubility was not changed notably until the hydrogenation temperature reached up to 650 °C. Furthermore, a drastic increase in hydrogen content was observed when specimens were held in hydrogen gas environment at 650 °C. However, hydrogen concentration decreased continuously for both samples above 650 °C. The decreasing regime of hydrogen concentration with increasing temperature is because of low solubility of hydrogen in Ti-6Al-4V alloy at higher temperatures as displayed in Equation 2.4. Accordingly, hydrogen solubility tends to diminish after hydrogenation temperature is increased above a certain temperature. This certain temperature that corresponds to maximum hydrogen absorbed treatment was found to be 650 °C in the present study. Similar results also have been revealed by several previous authors in the literature [78, 84 - 86].

Table 4. 1: Hydrogen concentrations of samples after hydrogenation at various temperatures.

Hydrogen Concentration (wt. %)								
	As-received	550°C	600°C	650°C	700°C	750°C	800°C	850°C
SLM	0.0042	0.07	0.15	1.19	0.95	0.92	0.78	0.70
SLM + HIPped	0.0139	0.06	0.12	1.17	0.97	0.88	0.66	0.63

4.2.2. Hydrogen Content After Dehydrogenation

According to ASTM F2924 standard (standard specification for additive manufacturing Ti-6Al-4V with powder bed fusion), the hydrogen content of SLM fabricated Ti-6Al-4V alloy must not be higher than 0.015 wt. % in order to obtain a structure without having a residual δ hydride phase. Grain refining with stable α + β phases and avoiding further hydrogen embrittlement are also maintained when the hydrogen content is lowered below 0.015 wt. %. Additionally, microstructural refinement of the alloy depends on the transformation of TiH_2, δ-phase to α-phase via dehydrogenation.

As illustrated in Figure 4.2 and presented in Table 4.2, hydrogen contents of the specimens which had been previously hydrogenated at 650 °C, were lowered considerably when specimens were hold at various temperatures (below α/β phase transition temperatures) for 6, 18, 24 h under 10^{-5} torr vacuum. Starting samples used in dehydrogenation step were the SLM and SLM+HIPped specimens which were previously hydrogenated at 650 °C for h to get maximum hydrogen concentrations of 1.19 wt. % and 1.17 wt. %, respectively.

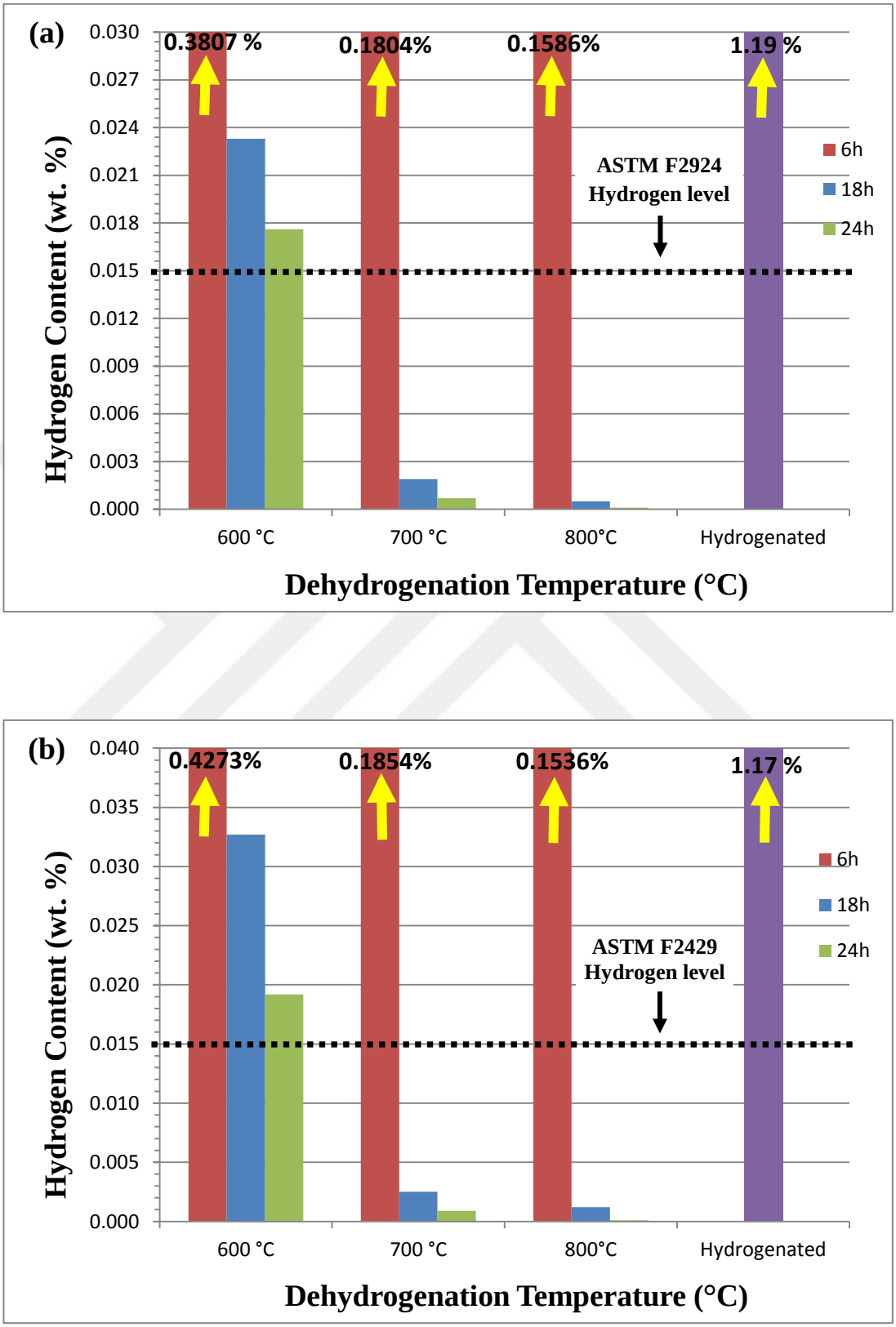

Figure 4. 2: Hydrogen contents of dehydrogenated Ti-6Al-4V samples fabricated by; (a) SLM, (b) SLM + HIP.

Table 4. 2: Hydrogen concentrations after dehydrogenation treatments.

	SLM samples (wt. %)			SLM + HIPped samples (wt. %)		
Temp. / Time	6h	18h	24h	6h	18h	24h
600°C	0.3807	0.0233	0.0176	0.4273	0.0327	0.0192
700°C	0.1804	0.0019	0.0007	0.1854	0.0025	0.0009
800°C	0.1586	0.0005	0.0001	0.1536	0.0012	0.0001
	*1.19 wt. % H before dehydrogenation			*1.17 wt. % H before dehydrogenation		

Although outgassing of hydrogen was accomplished at 600, 700 and 800 °C, vacuum treatment at 600 °C did not result a considerable hydrogen decrease neither in SLM samples nor in SLM+HIPped samples. Moreover, 6 h dehydrogenation time was not appropriate at any temperature between 600 and 800 °C in order to lower the hydrogen concentration below 0.015 wt. %. However, the decrease in hydrogen level was significant at 700 and 800 °C when dehydrogenation time was extended to 18 and 24 hours mainly due to kinetics of dehydrogenation process. After dehydrogenation at proper temperature for sufficient time, hydrogen contents of the samples were reduced even below those of as-received SLM and SLM+HIPped samples, which were 0.0042 wt. % and 0.0139 wt. %, respectively. At least 700 °C temperature and 18 hour operation is required with the purpose of lowering the hydrogen content of the disk shape specimens below a critical value as determined by ASTM F2924 standard.

4.3. Structural Analysis

In this section, phase compositions of as-received, hydrogenated and dehydrogenated specimens are evaluated using X-ray diffraction (XRD) data. Yet, due to overlapping of especially alpha (α), martensite (α') and hydride (δ) phase peaks at some 2θ angles, the structural analysis and phase determination in THPed Ti-6Al-4V samples became difficult. Additionally, peak broadening was observed at various hydrogenation temperatures and time mainly due to increased amount of dissolved hydrogen in hcp-α and bcc-β solid solutions, which may create lattice expansion. The lattice parameter (a) of the bcc-β phase varied with increasing hydrogen content according to Zhu et al. [110]. Hence, making interpretation on diffraction patterns becomes more challenging for hydrogenated samples.

The effect of hydrogenation at various temperatures for one hour on phase evolution of SLM and SLM+HIP samples is shown in X-ray diffraction patterns, Figure 4.3. All the samples were furnace cooled after hydrogenation was completed. Although only non-equilibrium α' (hcp-martensite) phase was observed in as-received SLM sample, as-received SLM+HIP sample, on the other hand, contained α and β equilibrium phases. Formation of δ (TiH_2) phase during hydrogenation is critical as the microstructure of the alloy is refined by δ to α phase transformation during dehydrogenation step. The critical dissolved hydrogen content for the formation of δ (TiH_2) phase is close to 15 at.% (0.385 wt.%) between 600 and 850°C as it is seen in the Ti-6Al-4V-Hx phase diagram suggested by Qazi et al, Figure 2.21(c) [81]. XRD findings supported findings of Qazi et al. and no δ phase formation was detected till 650 °C due to low hydrogen concentrations (given in Table 4.1). However, a slight peak broadening was observed particularly at 40° for samples hydrogenated at 500 and 600 °C and it became more evident when hydrogenation temperature was increased, Figures 4.3(a) and (b). According to the XRD patterns given in Figure 4.3, the peak broadenings were relatively greater in samples hydrogenated at 650, 700 and 750 °C possibly due to relatively higher hydrogen solubility in samples as presented in Figure 4.1. The hydrogen solubility of samples hydrogenated at relatively low (550, 600 °C) and high temperatures (800 and 850 °C) were less

compared to those of hydrogenated at moderate hydrogenation temperatures (650, 700 and 750 °C). Therefore, fcc-δ hydride phase did not appear due to insufficient hydrogen content in the samples hydrogenated at 550 and 600 °C temperatures. The amount of δ phase reached its maximum value after the hydrogenation at 650 °C and decreased continuously with increasing hydrogenation temperature. The LECO hydrogen measurements displayed in Figure 4.1 were relevant to XRD findings. However, further TEM studies must be conducted in order to verify the presence of fcc-δ phase for both hydrogenated and dehydrogenated samples.

Increasing hydrogen content promotes the β phase transformation, besides; the hydrogen solubility in SLM samples is restricted to α and/or α' phase(s) only up to a critical temperature since starting sample is composed of α' martensitic phase (Figure 3.1(a)). However, after certain temperature, by increasing hydrogen content, formation of β phase was observed at 39° and 56° 2θangles. In addition to effect of hydrogen, it is known that upon prolonged tempering of α'-phase at higher temperature, close beta transition temperature (above Ti_3Al formation temperature, 550 °C), i.e. 24 h, fine α+β phase mixture is formed. As can be seen in Figure 4.3(a), β-phase appeared in α'-martensitic matrix with high temperature hydrogen treatment probably due to combined effect hydrogen content and tempering of α'-phase. On the other hand, starting SLM+HIP samples were composed of lamellar structure containing equilibrium α and β-phases as seen in Figures 4.3(b) and 3.1. In both types of samples, namely, SLM and SLM+HIP samples there was a pronounced shift in 2θ values of α and β-phases towards low 2θ angles depending on the hydrogenation temperature. The shifts were more evident in β-phase peaks in both samples and they reached their maximum value especially between the hydrogenation temperatures of 650 and 750 °C, which correspond to samples containing relatively higher hydrogen, Figure 4.1. Therefore, the shifts through lower 2θ angles were attributed to crystal expansions due to increased dissolved hydrogen. On the other hand, the shifts in α-phase was not as evident as those observed in β-phase mainly due to relatively low hydrogen solubility of α-phase. The solubility difference between these phases can be seen in the phase diagram

shown in Figure 2.20. At the eutectoid temperature (300 °C), the terminal hydrogen solubility of hcp-α and bcc-β phases are 6.72 at.% (0.172 wt.%) and 39 at.% (1 wt.%), respectively [88]. Moreover, according to Paton et al., the terminal hydrogen solubility of hcp-α phase is not more than 7 at.% at the eutectoid temperature in the binary Ti-H phase system and the hydrogen content in α phase decreases drastically with decreasing temperature. The hydrogen content in the hcp-α phase is about 0.04 at.% (0.001 wt.%) which is quite negligible [89]. In contrast, the maximum hydrogen solubility without formation of hydride (fcc-δ) phase is about 50 at.% (1.28 wt.%) in the bcc-β phase at higher temperatures above 600 °C [90]. These studies reveal considerable hydrogen solubility of β phase and limited solubility of α phase, which is consistent with the present X-ray diffractions showing the broadening in the peaks which correspond to bcc-β phase. However, some peaks of α and α' phases were also broadened possibly due to introduction of δ phase which induce internal stresses.

As previously stated, hydrogen addition to titanium alloys lowers the β-phase transition temperature, thereby making presence of β phase possible at lower temperatures. Furthermore, the nose temperature in continuous-cooling-transformation (CCT) diagram decreases and the critical cooling rate (CCR) increases for α' (hcp martensite) and α'' (orthorhombic martensite) transformation with addition of hydrogen as shown in Figure 2. 25 [103]. As Figure 4.3(b) illustrates, although as-received SLM+HIP samples contained only equilibrium α and β phases, hydrogenation treatments at especially 750, 800, 850 °C caused α' martensite formation. Possibly, at specific temperatures due to effect hydrogen additional β-phase formation occurred in the matrix and subsequent cooling of the samples resulted partial transformation of beta phase to α'-martensitic phase.

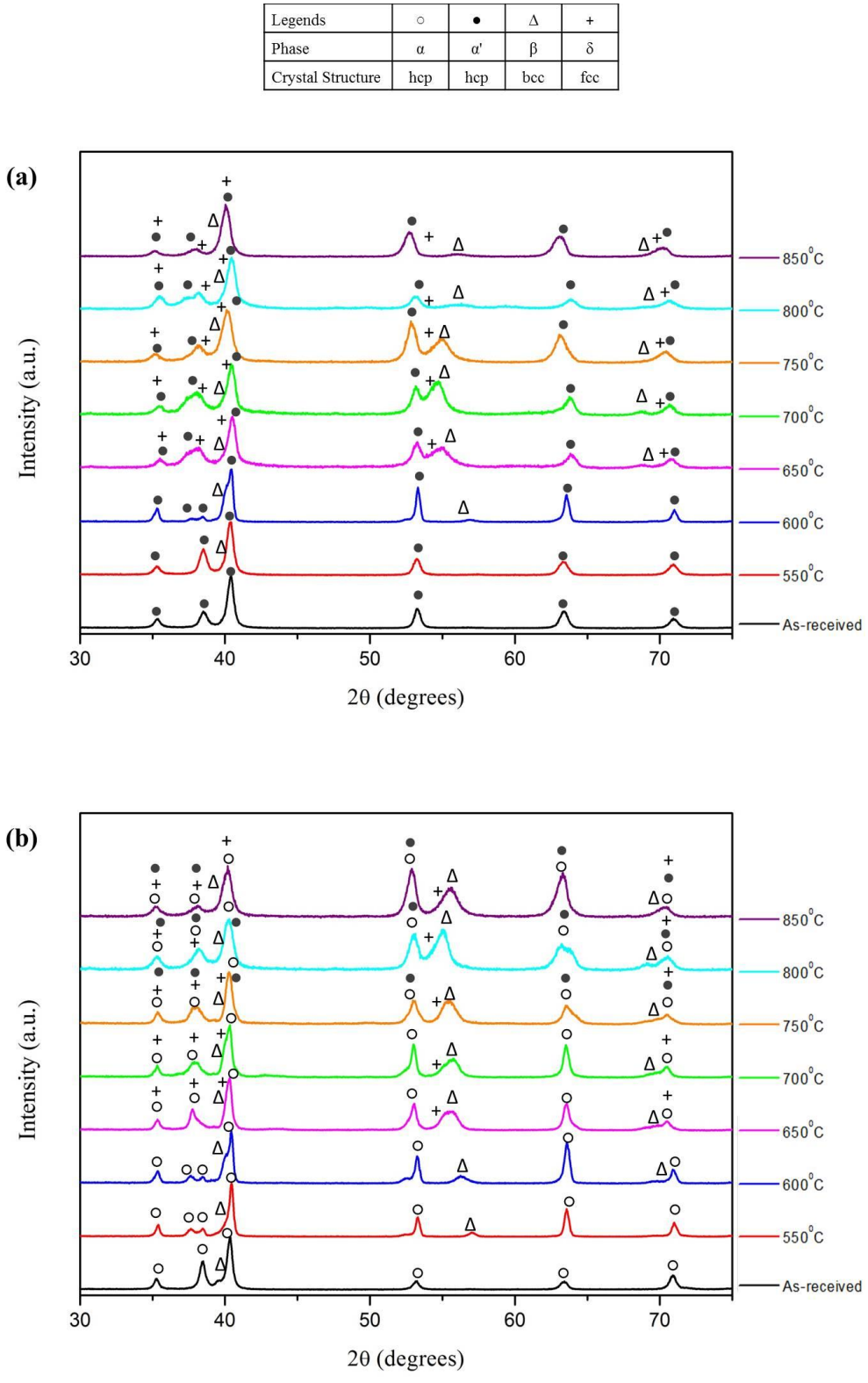

Figure 4. 3: XRD analysis of hydrogenated Ti-6Al-4V samples fabricated by; (a) SLM, (b) SLM + HIP.

In the dehydrogenation step, SLM and SLM+HIP samples hydrogenated at 650 °C with hydrogen contents of 1.19 wt.% and 1.17 wt.%, respectively, were underwent a dehydrogenation treatment at various temperatures and times within a vacuum chamber. The dehydrogenation process in vacuum was followed by furnace cooling down to the room temperature. X-ray diffraction patterns of dehydrogenated specimens are shown in Figure 4.4, during dehydrogenation due to decreased hydrogen content, δ (TiH_2) to α-phase transformation is expected as well as the decreased hydrogen levels of α- and β-phases. The critical level of hydrogen for the formation of δ-phase is 15 at.% (0.385 wt.%) as shown in Ti-6Al-4V-Hx phase diagram suggested by Qazi et al [81]**.** Therefore, below the critical hydrogen content, transformation of δ (TiH_2)-phase to α-phase is expected. All the dehydrogenation treatments except at 600 °C for 6 h resulted a significant decrease in the hydrogen contents below 0.385 wt.% (Table 4.2). Although, vacuum processing at 600 ^{o}C for 6 h decrease the hydrogen level to 0.3807, close to limit for formation of δ, no δ-phase peaks were detected in XRD patterns.

Dehydrogenation treatments which were performed at 600, 700 and 800 °C for 6 hours were not very effective in lowering the hydrogen contents. However, increased dehydrogenation temperature and time induced lower hydrogen contents as expected, (Table 4.2). Therefore, with a few exceptions, both peaks of α and β-phases shifted to higher 2θ values mainly due to crystal contraction occurred by decreased hydrogen content. As in the hydrogenation X-ray results, the shifts were more evident in β-phase as it is capably of dissolving more hydrogen. Although dissolved hydrogen may affect the peak widths and cause broadening, there was no clear difference between the peak widths.

Once sufficient dehydrogenation temperature and time are maintained under vacuum, δ phase transforms to α phase, and α, β phases lose its hydrogen content. As dehydrogenation temperature was increased to 800 °C, the relative intensity of β phase peaks were slightly increased due to formation of more β phase at higher temperatures.

Legends	○	●	Δ	+
Phase	α	α'	β	δ
Crystal Structure	hcp	hcp	bcc	fcc

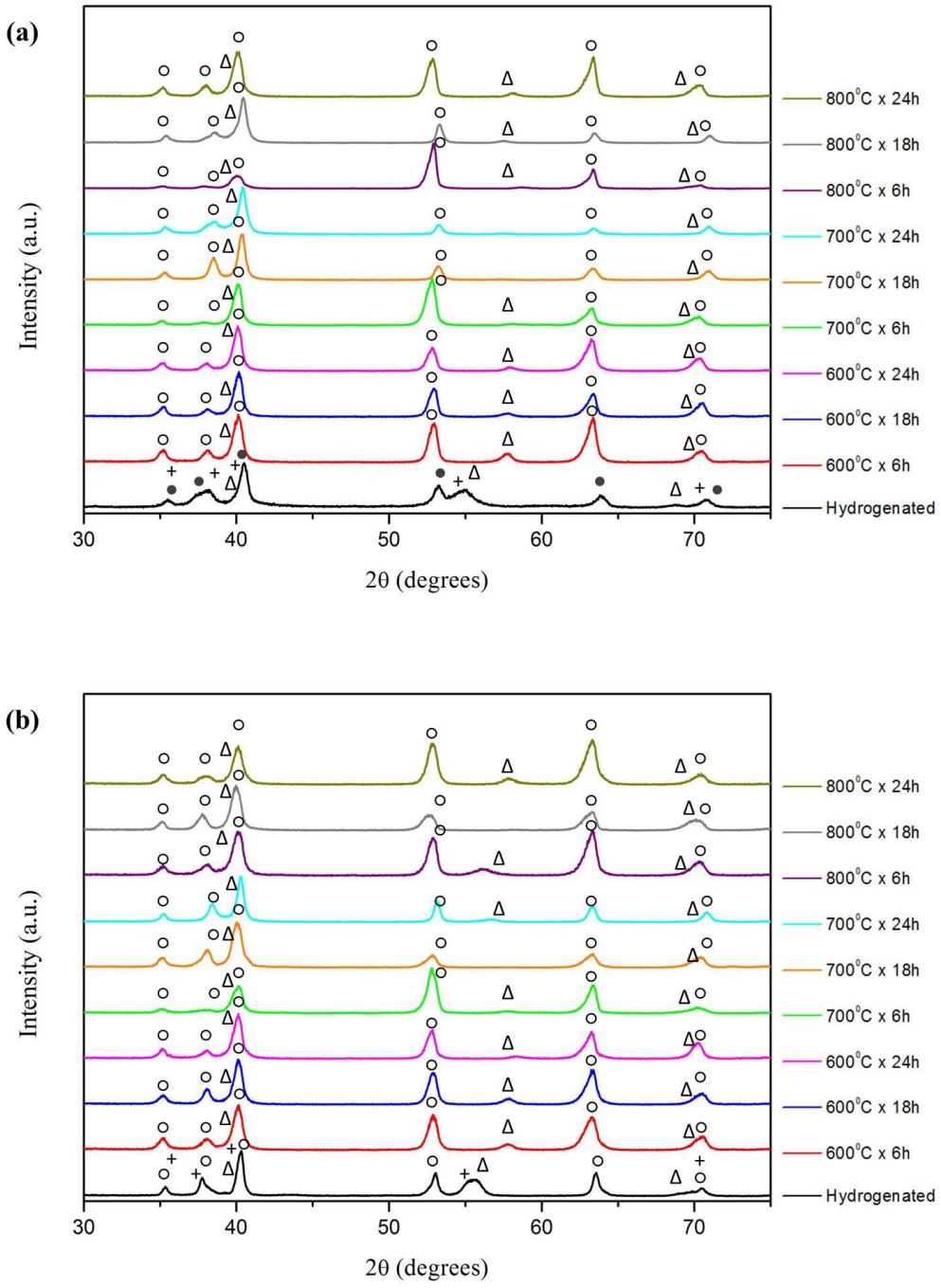

Figure 4. 4: XRD analysis of dehydrogenated Ti-6Al-4V samples fabricated by; (a) SLM, (b) SLM + HIP.

Hydrogen desorption was accomplished more effectively when dehydrogenation was conducted at higher temperatures for longer durations. However, with increasing temperature and time, more α precipitates occurs along grain boundaries. Grain boundary α and α grain growth is not desired in Ti-6Al-4V due to the decreased ductility and strength. Therefore, moderate temperature dehydrogenation temperature and time should be determined so as to eliminate the drawbacks of high temperature dehydrogenation.

4.4. Microstructural Evaluation

4.4.1. Microstructures of Starting Materials

The initial microstructures of additive manufactured samples affect subsequent phase transformations during THP and the final microstructure. In the present study, SLM and SLM + HIPped starting materials were fundamentally differs from each other due to thermal background of the materials that have been derived by fabrication processes. Upon slow cooling during solidification of a Ti-6Al-4V alloy, primarily β phase precipitates and subsequently partially α phase formation occur in the microstructure. The type and relative amounts of phases in the starting material changes the type and amounts of phases and their hydrogen solubility at hydrogenation temperature. Therefore, although the starting chemical composition of the alloys may be the same, their phase transformation kinetics and resultant microstructure may differ. The approximate relative amounts of α and β phases in a slowly cooled cast Ti-6Al-4V alloy are 90:10 percent [13]. Likewise, equilibrium cooled wrought Ti-6Al-4V alloys also display similar ratio of phases with a significantly higher amount of α-phase. However, because of large thermal input and rapid solidification during SLM process, a non-equilibrium α'-martensitic phase needles formed instead of α and β phases, Figure 4.5. Very high cooling rate is needed to prevent formation of equilibrium lamellar α and β phases and grain boundary α. CCR was estimated to be around 10^4 K/s according to Vilaro et al. [69]. Although the yield strength is higher in SLM fabricated Ti-6Al-4V alloys, the initial

metastable α' microstructure leads to a degradation particularly in ductility when compared to conventionally manufactured Ti-6Al-4V alloy. This fact will be discussed further in the mechanical properties part. A microstructure which consists of α' martensite is undesirable due to loss of ductility; therefore, SLM fabricated Ti-6Al-4V parts must be subjected a post process to transform the starting metastable microstructure to stable phases to increase ductility.

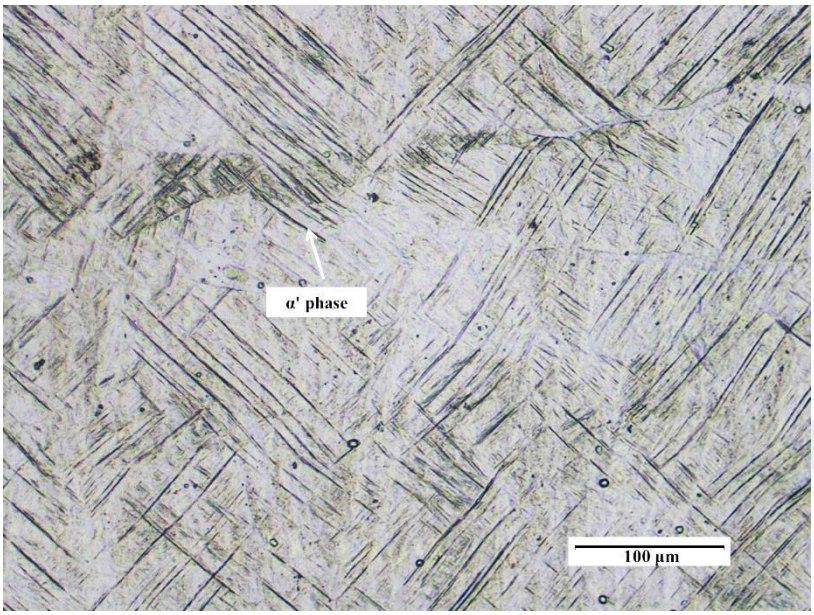

Figure 4. 5: Optical micrograph of SLM fabricated starting Ti-6Al-4V alloy.

The SLM fabricated and subsequently HIPped sample (HIP parameters were given in 3.2) shown in Figure 4.6. This sample has a lamellar microstructure which contains α and β phases in Widmanstätten structure. In the optical micrograph, the bright regions correspond to α phase and the dark ones between α Widmanstätten plates are β phases. Subsequent HIPping in this samples were conducted for elimination of residual porosity left from SLM process and to convert non-equilibrium α' to equilibrium phases. HIPping conducted at 920 °C, close to α+β/β phase boundary, caused transformation of α' to α and nucleation of β-phase between α-plates.

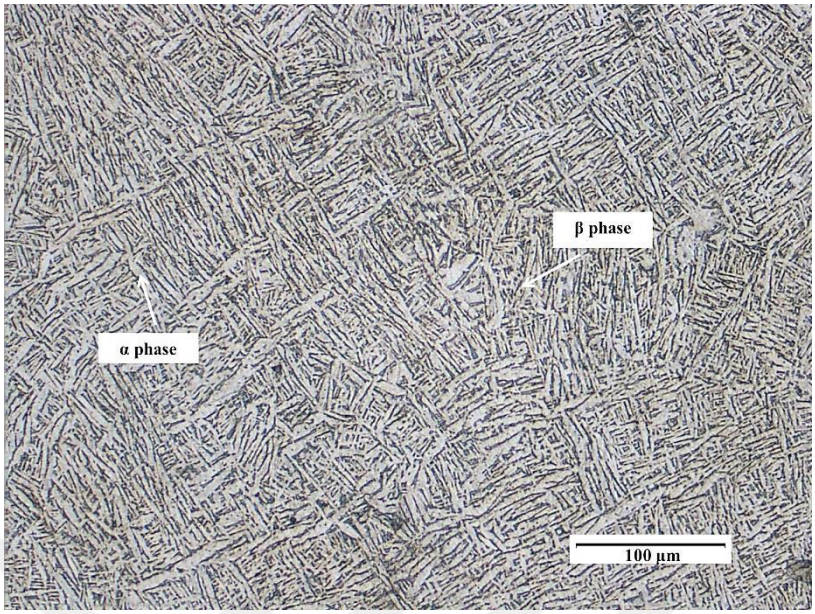

Figure 4. 6: Optical micrograph of SLM fabricated and HIPped starting Ti-6Al-4V alloy.

SEM images shown in Figure 4.7 reveal the phases in both types of samples more clearly. α'-martensitic phase appears as white needles in SLM fabricated samples, Figure 4.7 (a), and α and β phases in lamellar structure in SLM+HIPped samples correspond to dark and bright regions respectively, Figure 4.7 (b).

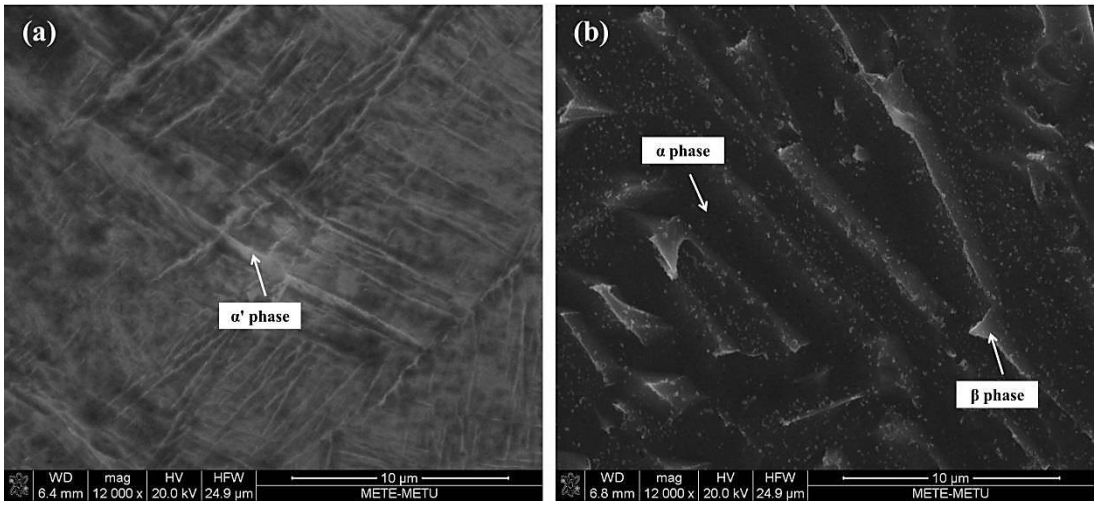

Figure 4. 7: SEM images of starting; (a) SLM, (b) SLM + HIPped Ti-6Al-4V alloys.

Although elemental distribution in SLM sample containing α'-martensitic phases was more or less homogenous throughout the samples, alloying element partitioning was observed in SLM+HIPped sample. The differences in elemental composition distribution also affect the response of samples to thermo-hydrogen treatment and phase transformation kinetics. Elemental analysis of each existing phase in SLM+HIPped sample is shown in Figure 4.8. EDX analysis revealed that dark regions (α phase) shown in Figure 4.7(b) consisted of relatively higher aluminum content and less amount of vanadium (Figure 4.8(a)). Conversely, the bright areas (β phase) seen in Figure 4.7(b) contained more vanadium and less aluminum elements, (Figure 4.8(b)).

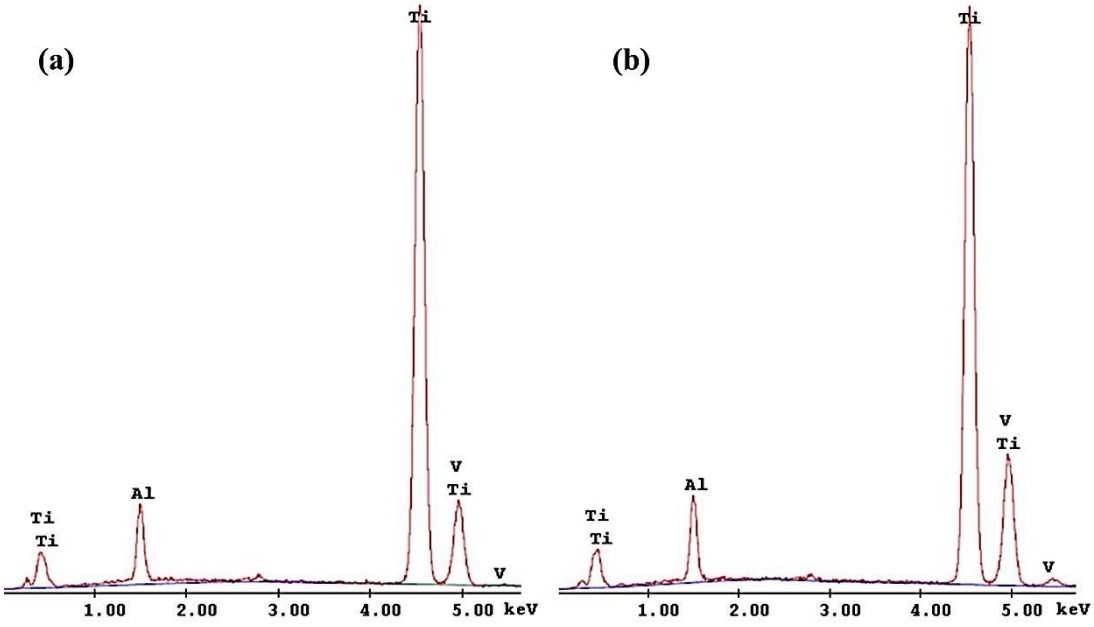

Element	Wt. %	At. %
Al	7.24	12.19
V	2.03	1.81
Ti	90.72	86.00

Element	Wt. %	At. %
Al	5.12	10.57
V	10.06	9.02
Ti	84.82	80.41

Figure 4. 8: EDX results of SLM + HIPped Ti-6Al-4V sample consisting of; (a) α phase, (b) β phase.

In SLM, laser scanning parameters affect various features including microstructure, texture, porosity content and surface roughness of the sample. In order to develop non-porous and fine microstructure for the samples of the present study, the

volumetric energy density (E) was kept as 10.8 J/mm^3. The volumetric energy density is determined by several scanning patterns which were previously discussed in Chapter 3.1. The hatch spacing, which is basically defined as the distance between adjacent laser scanning tracks, is one of the critical process variables effecting the E. In Figure 4.9, an optical micrograph (200x magnitudes) of SLM fabricated Ti-6Al-4V can be seen. The scan track width between neighboring layers was roughly measured about 72 μm which is equal to hatch spacing. Moreover, because of the zigzag scanning strategy, each track was formed after 90° rotation of each layer (Figure 4.9). The hatch spacing determines the α/β colony size and sometimes α-phase may be formed in the boundary of each regions due to oxidation of layers. Although THP changes the microstructure of each layer it is ineffective on changing the directional layered structure. On the other hand, the SLM + HIPped sample does not exhibit a track trace in the microstructure mainly due to post treatment including hydrostatic pressure and high temperature.

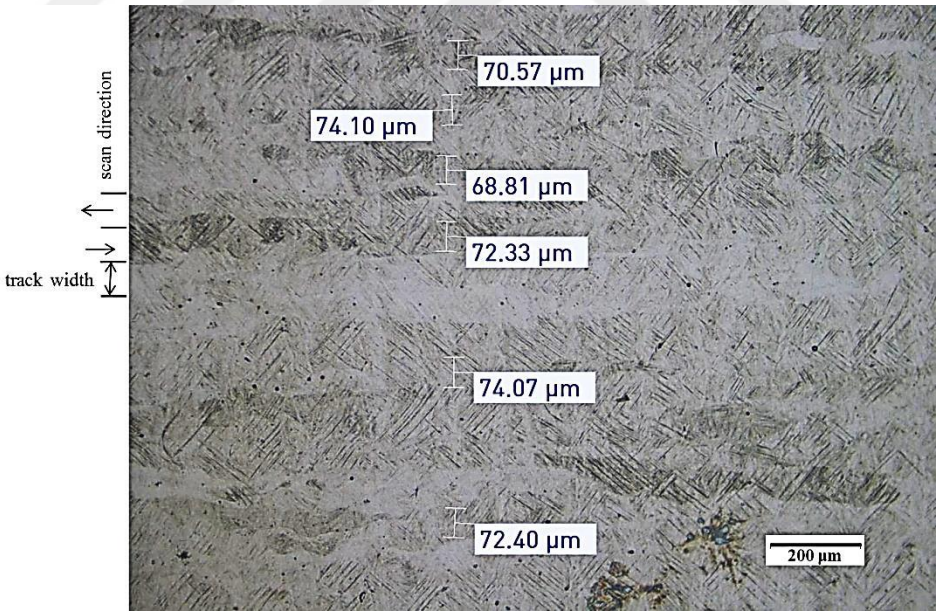

Figure 4. 9: Optical micrograph illustrating the hatch spacing on SLM fabricated specimen.

4.4.2. Microstructural Evaluation of Hydrogenated Samples

In this part, microstructural evolution is presented for SLM and SLM+HIPped hydrogenated at temperatures between 550-850 °C with 50 °C intervals. For both types of samples, the hydrogenation treatments conducted at 550°C and 600 °C did not change the microstructure significantly, Figures 4.10 and 4.11. The SLM samples contained α' needles, Figures 4.10 (b) and (c), and SLM+HIPped samples consisted of Widmanstätten structure with lamellar α and β phases similar to starting sample, Figures 4.11 (b) and (c). Therefore, hydrogen treatments at 550°C and 600°C for 1 hour did not have significant influence on the microstructure of the alloys. These treatments conducted at 550 °C and 600 °C did not induce formation of phases that is different from starting samples as presented in X-ray diffraction patterns, Figure 4.3. However, introduction of hydrogen at and above 650 °C drastically changed both the microstructure and hydrogen content. The relatively high diffusivity of hydrogen at the temperatures of 650 and 850 °C was also revealed by previous LECO hydrogen measurements (Figure 4.1). The effect of hydrogen is also clearly seen in the microstructures of various hydrogenation temperatures, Figures 4.10 (d)-(h) and 4.11 (d)-(h). The starting fine needle-like morphology of SLM samples were coarsened especially at the temperatures of 650, 700 and 750 °C, Figures 4.10 (d)-(f). According to X-Ray results (Figure 4.3 (a)), β-phase nucleated within the α'-martensitic matrix possibly due to exceeded hydrogen solubility limit of α'-martensitic phase. Additionally, δ-phase formation was observed as hydrogen level reached a critical level in the alloy. However, neither optical microscope nor scanning electron microscope was able to distinguish each phase. Therefore, High-Resolution Transmission Microscope (HR-TEM) examinations are needed to correlate microstructure and X-Ray results. Although the types of phases at 800 and 850°C were similar (XRD patterns in Figure 4.3(a)), at 800 °C, needle like morphology disappeared completely and microstructure became relatively finer with the formation of nearly equiaxed grain boundaries. On the other hand, hydrogenation at 850 °C and subsequent cooling resulted with single-phase regions together with very fine martensitic structure within large equiaxed grains.

As stated previously, increasing hydrogen content lowers the β-phase transition temperature of the alloy. When hydrogen solubility of the alloy reaches to 15 at.% (0.385 wt.%), the temperature for 100% β-phase formation decreases to a temperature between 800 and 850 °C (Figure 2. 21). In the present study, the hydrogen contents of the SLM samples hydrogenated at 850°C were around 0.7 wt.% hydrogen. This hydrogen concentration also corresponds to the same β-phase transition temperature of between 800-850 °C. Therefore, SLM samples hydrogenated at 850°C was possibly composed of only β-phase (hydrogen loaded) at hydrogenation temperature. Because of that, substantial β-phase grain growth occurred as can be seen by previous beta phase grain boundaries in Figure 4.10 (h). Upon cooling of the hydrogen loaded β-phase, due to alloying element partitioning α-phase nucleates along the grain boundaries and within the grains of β-phase. Further cooling causes formation of δ-phase on α-phase boundaries due to decreased hydrogen solubility of hcp-α as shown in Figure 2.24. However, since increased hydrogen content of the alloy increases CCR it becomes easier to form α'-martensitic structure as detected formation of needle-like structure in Figure 4.10 (h). Therefore, the microstructure obtained at 850 °C hydrogenation is not the true microstructure of sample when it was at 850 °C hydrogenation temperature; conversely, it is the microstructure obtained by the transformation of hydrogen loaded high temperature β-phase. Although α'-martensite was observed in the samples, there were untransformed β-phase regions as well due to shifted beta phase composition, which changes martensite start temperature. If the alloy were in the 100% β-phase region, the microstructure would contain 100% martensitic phase. Therefore, it can be concluded that 850°C was high enough to form mainly beta phase, but not 100%.

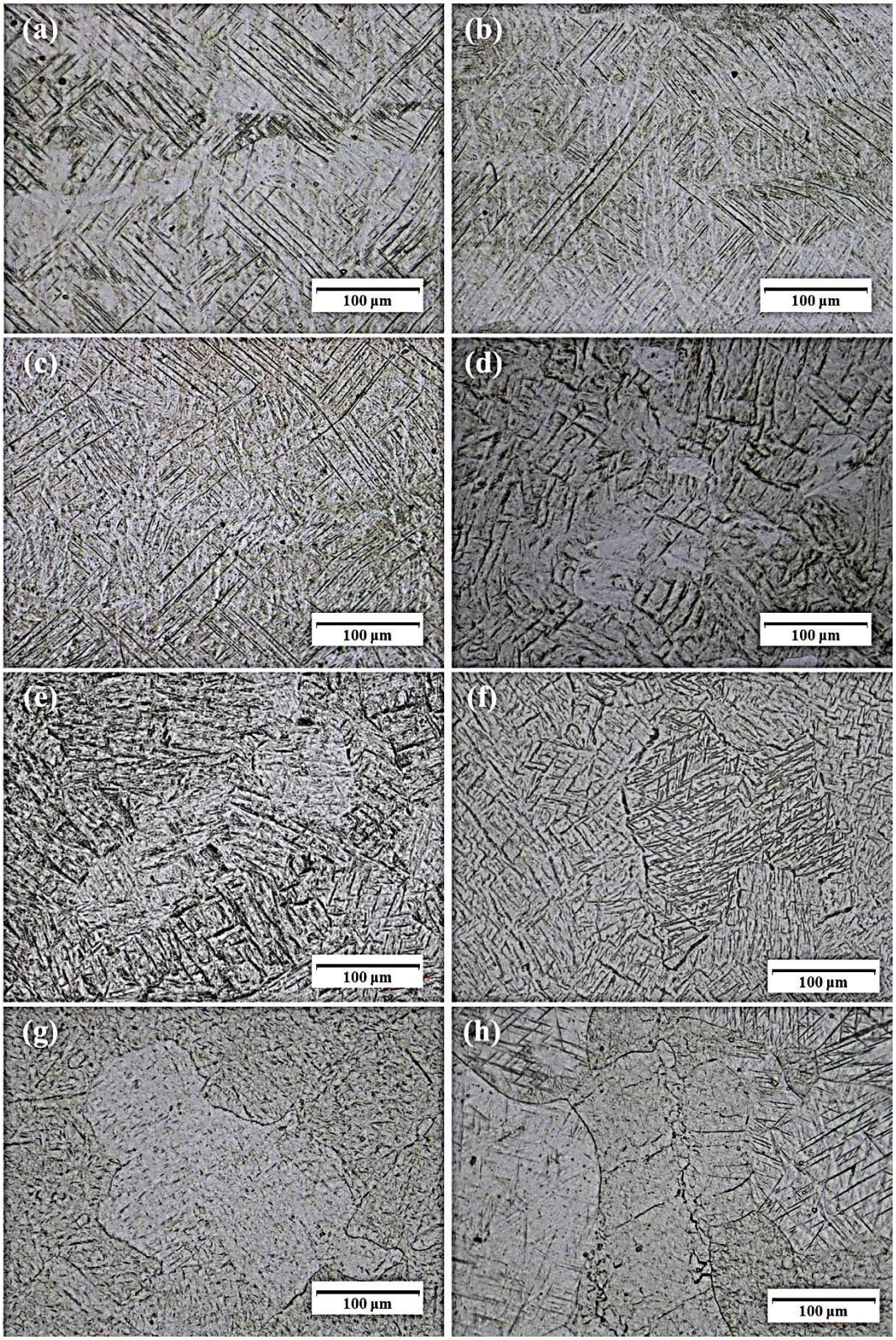

Figure 4. 10: Optical micrographs after 1 hour hydrogenation of SLM fabricated specimens at various temperatures; a) as-received, b) 550 °C, c) 600 °C, d) 650 °C, e) 700 °C, f) 750 °C, g) 800 °C, h) 850 °C.

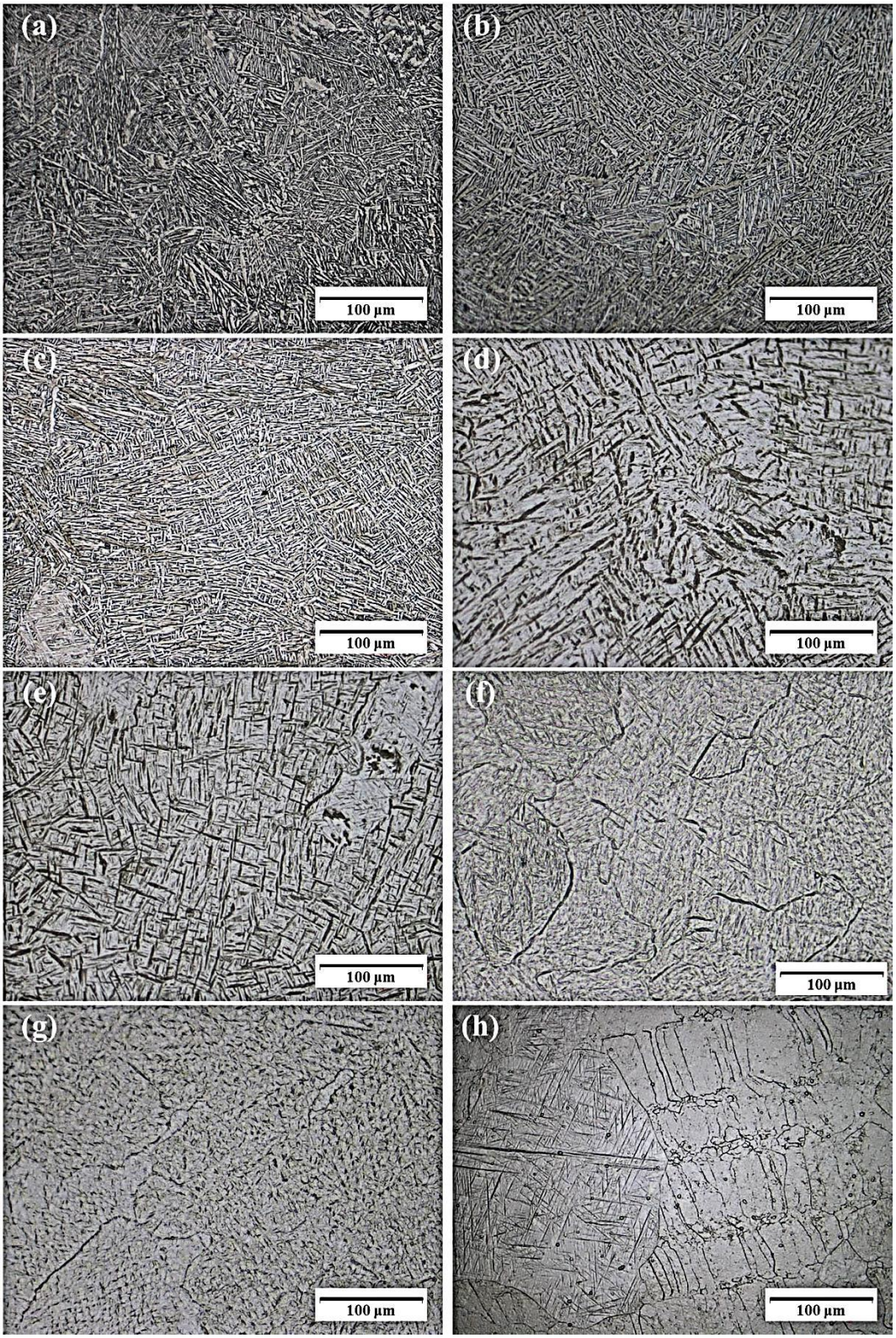

Figure 4. 11: Optical micrographs after 1 hour hydrogenation of SLM + HIPped specimens at various temperatures; a) as-received, b) 550 °C, c) 600 °C, d) 650 °C, e) 700 °C, f) 750 °C, g) 800 °C, h) 850 °C.

Another remarkable finding attained from the optical micrographs is that in SLM+HIPped samples hydrogenated at and above 650 °C temperatures displayed microstructures similar to those of SLM samples, Figure 4.11. Although SLM+HIPped samples starting microstructures were composed of lamellar α+β phases, they displayed a response to hydrogen atmosphere similar to SLM samples with α'-martensitic starting microstructures. Actually, in SLM samples, β-phase started to form in martensitic matrix above 600 °C (Figure 4.3(a)) as stated previously and microstructure became similar to SLM+HIPped samples. The SEM images of the specimens, which were hydrogenated at 650°C, can be seen in Figure 4.12. Figure 4.12(a) belongs to SLM fabricated specimen while Figure 4.12(b) corresponds to SLM + HIPped specimen. In this figure, the titanium hydride phase (δ) seems darker because of the electron radiation transmitted along the matrix. The δ plates distributed in the same form and shape for both images shown in Figure 4.12. The analogous SEM findings that reveal the presence of darker δ phase were also studied by Oguh et al. previously [97].

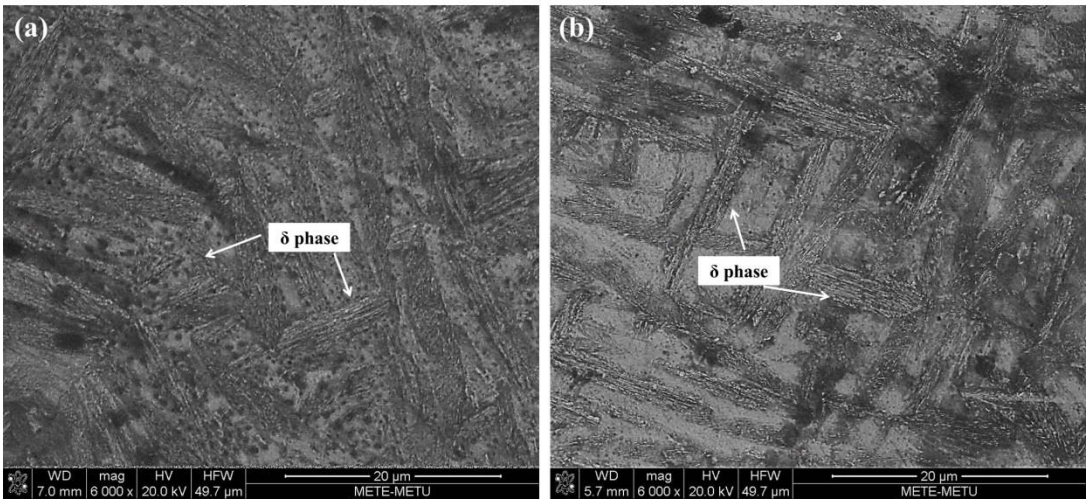

Figure 4. 12: SEM images of the specimens hydrogenated at 650 °C; (a) SLM, (b) SLM +HIPped.

4.4.3. The Effect of β Solutionizing Treatment on the Microstructure

The β solutionizing experiments were conducted at 800, 850 and 900 °C temperatures for 15 minutes in order to determine the critical temperature which induces 100% β phase formation. β solutionizing treatments were carried out using samples hydrogenated at 650 °C since they possessed maximum amount of hydrogen. During β solutionizing, hydrogenated samples were held for 15 minutes at certain solutionizing temperatures after they were heated slowly. The samples were furnace cooled naturally down to room temperature under argon atmosphere for microstructural examination. Figures 4.13 and 4.14 show the microstructures of β-solutionized SLM and SLM + HIPped specimens at various temperatures. It must be primarily noted that microstructures of both solutionized SLM and SLM + HIPped specimens were similar independent of the initial fabrication method. As suggested before, β transition temperature in Ti-6Al-4V-Hx system decreases suddenly with increasing hydrogen content. In the present study, microstructure of β solutionized samples, Figures 4.13(a) and 4.14(a), at 800 °C was as same as those hydrogenated samples at 800 °C, Figures 4.10 (g) and 4.11(g). Since the samples were heated to 800 °C solutionizing temperature in 25%H_2+75%Ar gas mixture after hydrogenation at 650 °C, the solubility of hydrogen possibly decreased during heating and thus, the alloy had similar microstructure to that of hydrogenated at 800 °C. There was no clear evidence of 100 % beta phase formation since beta grains was not resolved in the microstructures. However, solutionizing at 850 and 900 °C led to formation of β phase, which was identified by clear beta phase grain boundaries. Although subsequent cooling from 850 °C resulted partial transformation of beta phase to martensitic phase, nearly 100% martensitic transformation appeared after 900 °C solutionizing Figures 4.13(b), (c) and 4.14 (b), (c). Therefore, 100% beta phase formation temperature was identified as a temperature close to 900 °C.

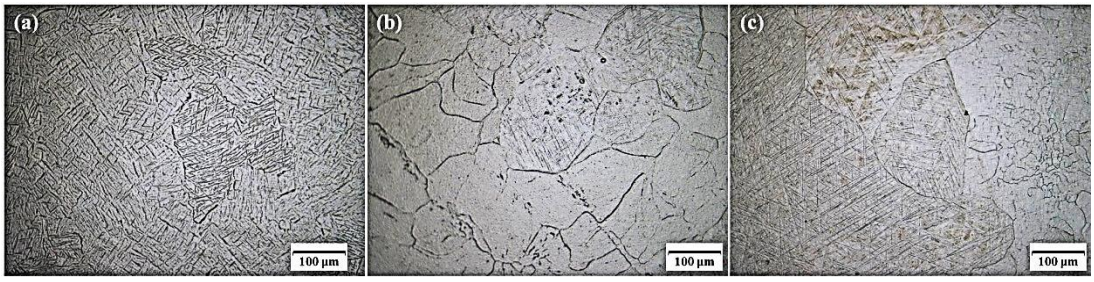

Figure 4. 13: Optical micrograph (500X) of β solutionized SLM specimens at; (a) 800 °C, (b) 850 °C, (c) 900 °C.

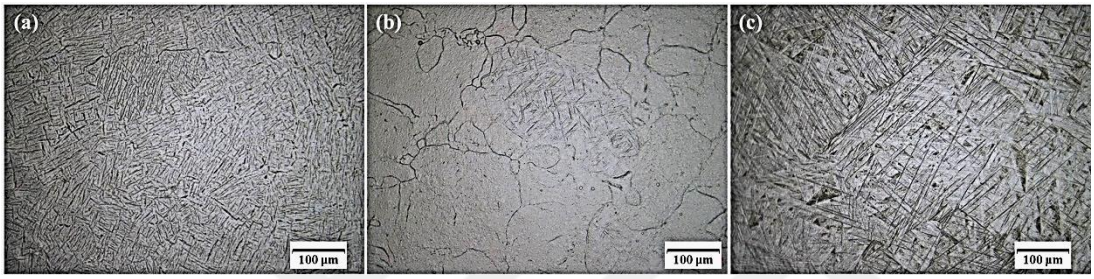

Figure 4. 14: Optical micrograph of β solutionized SLM + HIPped specimens at; (a) 800 °C, (b) 850 °C, (c) 900 °C (500X).

4.4.4. Microstructural Evaluation After Eutectoid Decomposition

Eutectoid decomposition was carried out by cooling the samples down to 600 °C which were previously hydrogenated at 650 °C for 1 h and β-solutionized at 900°C for 15 mins. Samples were hold for 3 h at the eutectoid decomposition temperature (600 °C) so as to allow transformation of β phase to a fine microstructure containing α, α' and δ-phases together with some residual β-phase. In this process step, β phase transformed to α and needle like α'-martensitic phases, Figure 4.15. Although formation of δ phase was also expected, it could not be resolved either from the optical or electron microscope images. Once Ti-6Al-4V was cooled down from β transition temperature, α phase formed and grown at primary β phase grain boundaries, which is detrimental to ductility of the alloy. This condition can only be avoided by rapid cooling from β phase region. α plates at grain boundaries can be

seen in Figures 4.15(a) and (b), which occur as a result of eutectoid decomposition at relatively slow cooling rates.

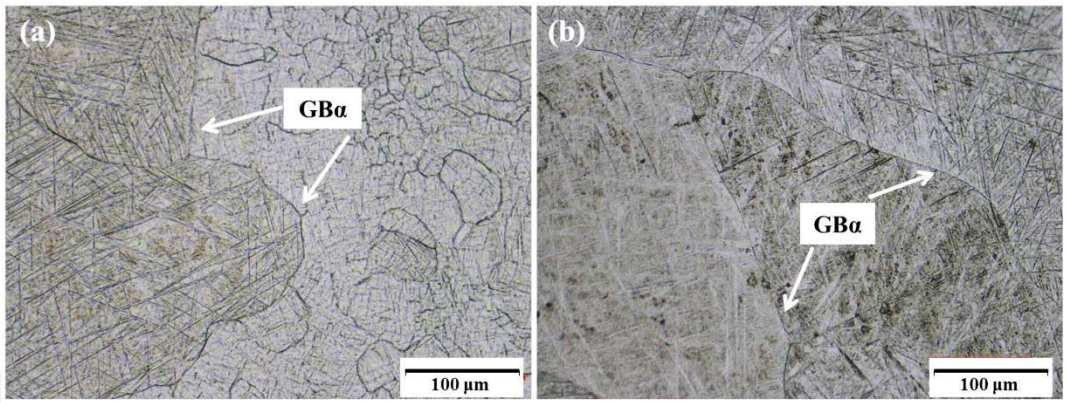

Figure 4. 15: Optical micrograph illustrating grain boundary α-phase formation after eutectoid decomposition treatment of; (a) SLM, (b) SLM + HIPped samples.

4.4.5. Microstructures of Dehydrogenated Samples

In THP, microstructural refinement depends on decomposition of fine δ hydride phase to fine equilibrium α phase and loss of hydrogen in α and β phases. Therefore, in order to transform δ phase to α phase and to avoid the hydrogen embrittlement, specimens, which were previously decomposed by eutectoid transformation, were kept at an elevated temperatures under high vacuum (~10^{-6} Torr).

Various dehydrogenation treatments were applied to observe the impact of time and temperature on microstructure and residual hydrogen contents. Since the hydrogen levels in dehydrogenated samples at 700 and 800 °C were similar and also in the desired range, Figure 4.2, specimens were underwent vacuum dehydrogenation at relatively low constant temperature of 700 °C for 6, 18 and 24 hours. Optical micrographs of both SLM and SLM + HIPped samples were compared in the same figure due to their analogous microstructures attained after dehydrogenation treatments. Figure 4.16 (a) and (b) illustrate the microstructures of samples dehydrogenated at 700 °C for 6 hours. Both samples consisted of relatively coarser α

and β phases because of insufficient time for refinement. Besides, at 700 °C, prolonged dehydrogenation time, i.e. 18 h, led to more equiaxed, finer and well dispersed phases as shown in Figures 4.16 (c) and (d). Holding the specimens at 700 °C for 24 hours also caused equiaxed grains, however, a slight coarsening of phases was observed, Figures 4.16 (e) and (f). As a result of dehydrogenation, neither α' phase nor δ-phase remained in the structure. Fine microstructure seen in Figure 4.16 (c)-(f) was composed of only α and β-phases as detected in XRD patterns, Figure 4.4.

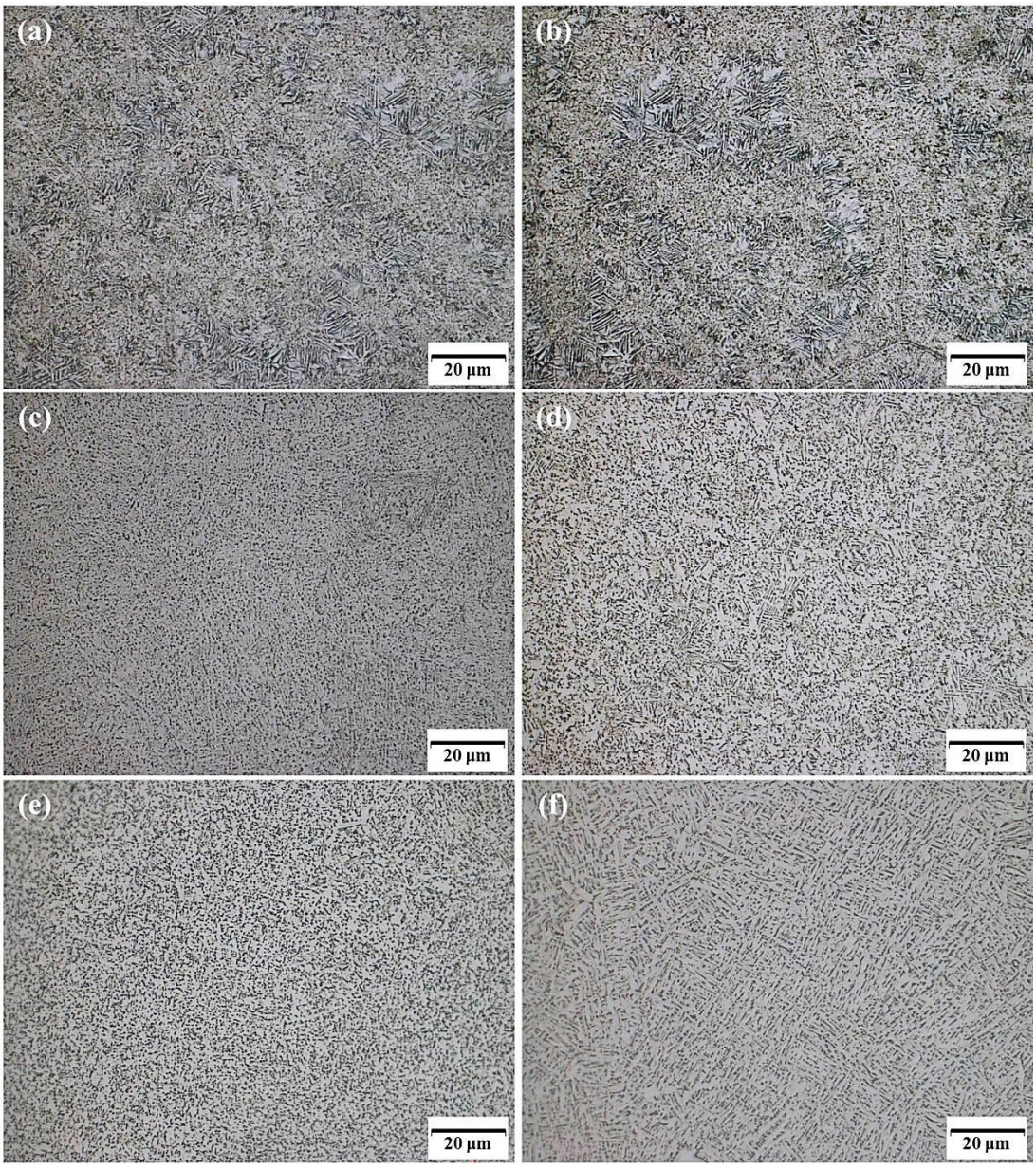

Figure 4. 16: Optical micrographs of the specimens dehydrogenated at 700 °C for various times; (a) SLM: 6 h, (b) SLM +HIPped: 6 h, (c) SLM: 18 h, (d) SLM + HIPped: 18 h, (e) SLM: 24 h, (f) SLM + HIPped: 24 h.

Furthermore, dehydrogenation experiments were conducted at different temperatures (600 and 800 °C) for comparison by keeping the dehydrogenation time at 18 h. Vacuum treatment at various temperatures induced similar microstructures obtained

at 700 °C vacuum treatment, Figure 4.17. However, 600°C vacuum treatment for 18 hours was not enough to get fine microstructure, Figures 4.17(a) and (b).

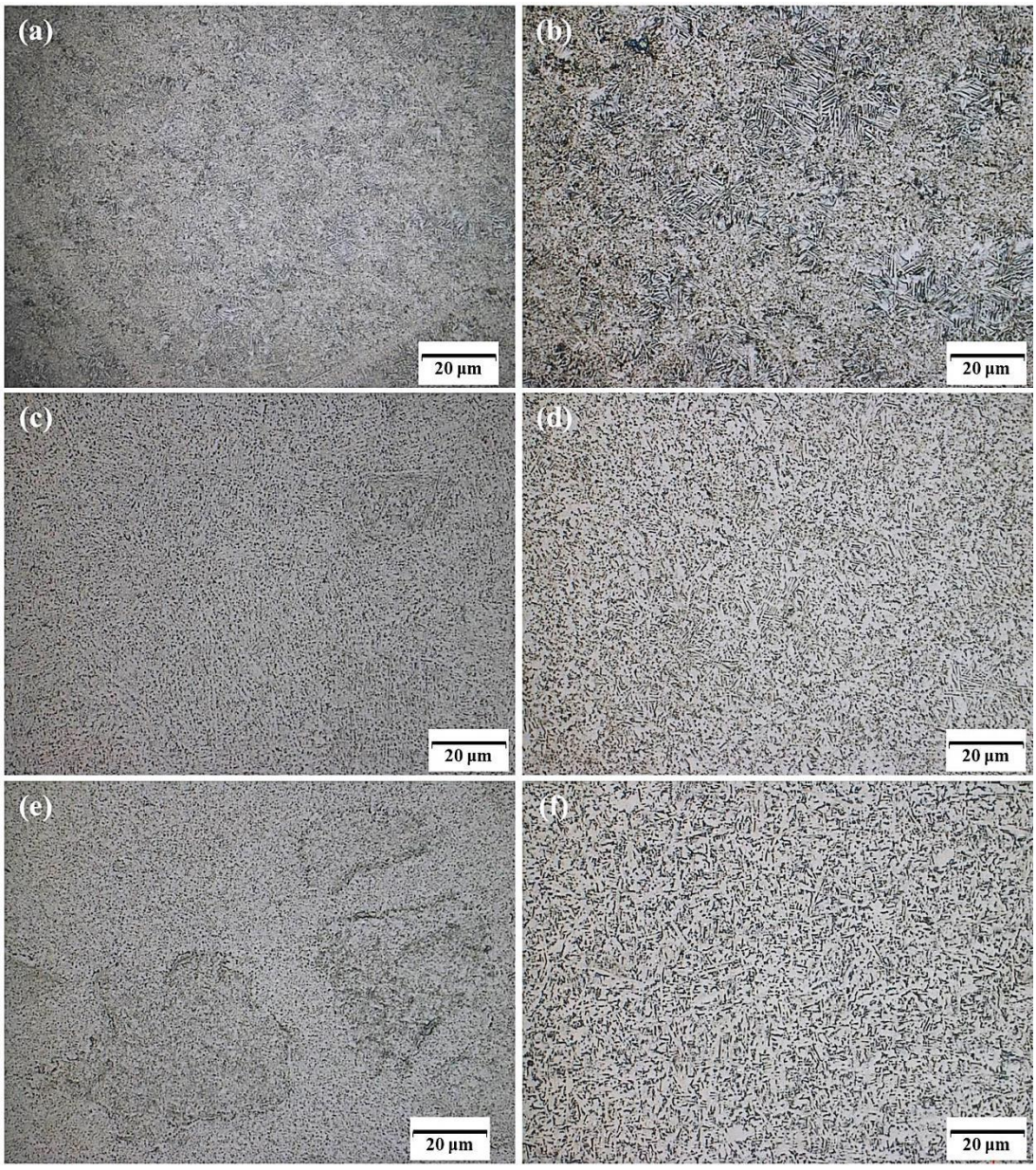

Figure 4. 17: Optical micrographs of the specimens dehydrogenated for 18 hours at various temperatures; (a) SLM: 600 °C, (b) SLM +HIPped: 600 °C, (c) SLM: 700°C, (d) SLM + HIPped: 700 °C, (e) SLM: 800 °C, (f) SLM + HIPped: 800 °C.

As the dehydrogenation temperature increases more equiaxed and finer grains were observed (Figure 4.17(c) and (d)), however, grain growth occurs with substantial

increase in temperature. Accordingly, 800 °C treatment for 18 hours resulted coarser α and β phases as shown in Figures 4.17(e) and (f).

Although α-phase formation along previous β-phase grain boundaries is not desired, almost all samples had α-phase formation after 4-step THP. The micrographs of dehydrogenated samples shown in Figure 4.18 reveals the α phase formation along previous β phase grain boundaries. As schematically illustrated in Figure 2.24, primary α grains forms along β grain boundaries especially when the cooling rate from β transus is too slow to prevent α phase accumulation [100]. In the present study, the cooling rate of 10°C/min during cooling from β solutionizing temperature (900 °C) to eutectoid decomposition (600 °C) treatments was not rapid enough to avoid α phase formation along the grain boundaries as shown in both Figures 18(a) and (b).

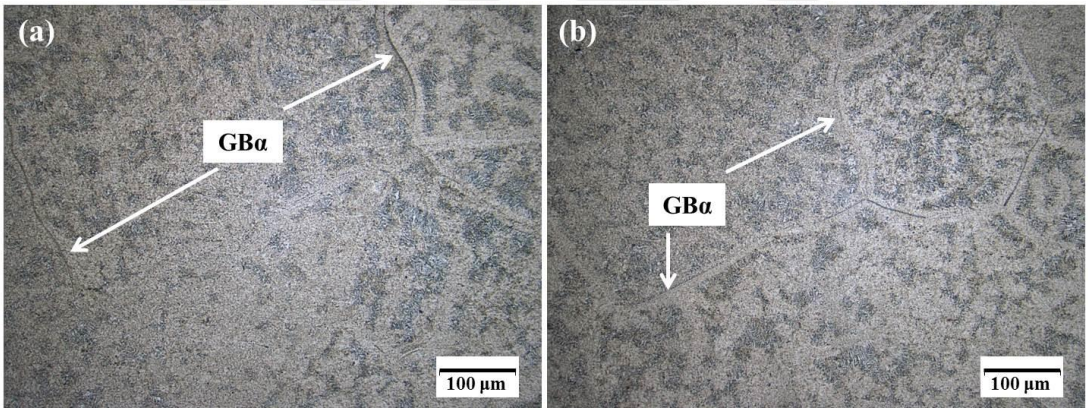

Figure 4. 18: Optical micrographs illustrating α phase accumulation at grain boundaries after dehydrogenation at 600 °C for 18 h; (a) SLM, (b) SLM+HIPped.

Previous β-grain size is also effective in determination of the mechanical properties as well as the microstructure observed in grains. Micrographs of dehydrogenated samples, taken at 50X, revealed growth of previous β-phase, Figure 4.19. The previous β-phase grain sizes were measured as 71(±6 and 108±11 µm in starting SLM and SLM + HIPped specimens, respectively. However, previous β-grain sizes of the corresponding samples increased to 496 ± 55 µm and 598 ± 74 µm, respectively, after eutectoid decomposition and dehydrogenation (700 °C for 18 h).

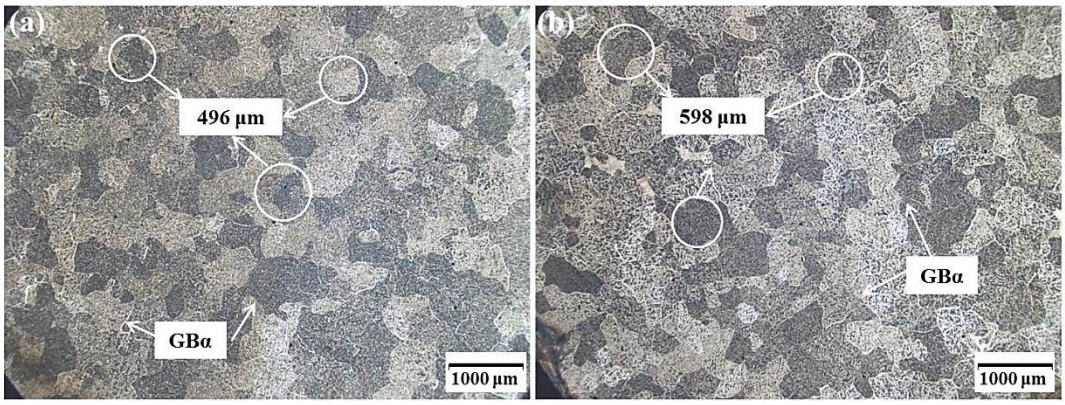

Figure 4. 19: Optical micrographs illustrating the previous β-phase grain size at 50 x magnification of; (a) SLM, (b) SLM + HIPped specimens.

The β-grain growth presumably occurred during β solutionizing at 900 °C. Therefore, as a novel THP in the present study, β solutionizing and eutectoid decomposition steps were eliminated to prevent grain growth and thus THP was performed in 2 steps (hydrogenation and dehydrogenation) to get similar refined microstructures. 2 steps treatment was successful in preventing grain growth problem. The grain sizes of samples remained nearly unchanged as shown in Figure 4.20.

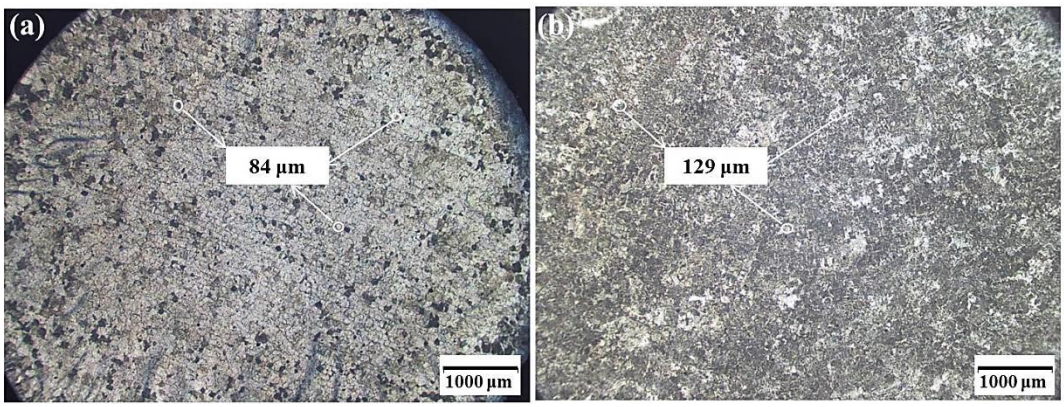

Figure 4. 20: Optical micrographs illustrating the previous β-phase grain size at 50 x magnification of 2 stepped THP; (a) SLM, (b) SLM + HIPped specimens.

In addition to previous grain sizes, microstructural refinement by transformation of previously formed δ-phase to α-phase, α' to α and loss of hydrogen in α and β-

phases is important. For 2 step THP, samples which were previously hydrogenated at 650°C for 1 h were used as the hydrogen loaded samples to be used in the second dehydrogenation step which was conducted at 700 °C for 18 h.

Figures 4.21 and 4.22 compare SEM images of starting and hydrogenated sample with the microstructures after 4- and 2-step THP. Grain refinement was also accomplished and finer grains were obtained without applying β solutionizing and eutectoid decomposition steps for both SLM and SLM + HIPped specimens (Figures 4.21(d) and 4.22(d)). Starting α'-martensitic phase (Figure 4.21(a)) in SLM samples transformed to fine α (dark regions) and β-phases (bright regions), see Figure 4.4. Although the phases in SLM+HIPped samples after dehydrogenation were as same as its starting sample (α and β-phases, Figure 4.22(a)), the microstructure after hydrogenation and dehydrogenation steps was significantly finer as shown in Figures 4.22(c) and (d). The dark needles shown in hydrogenated samples (Figures 4.21(b) and 4.22(b)) were transformed to the fine microstructure which consists of α and β phases when dehydrogenation were conducted at 700 °C for 18 hours for both SLM and SLM+HIPped samples. These microstructural evaluations of dehydrogenated samples were consistent with the phase analysis as illustrated in the XRD patterns in Figure 4.4.

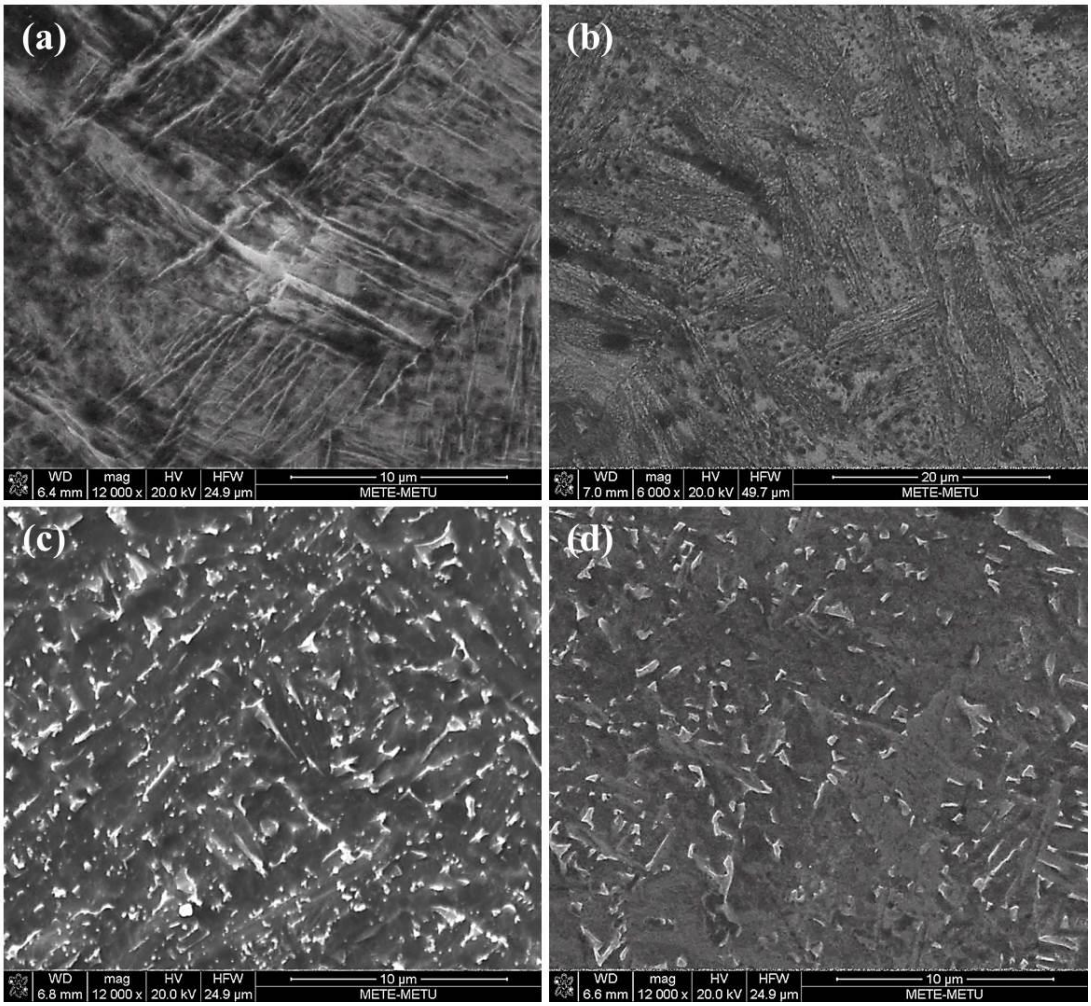

Figure 4. 21: SEM images of SLM specimens; (a) initial, (b) hydrogenated at 650 °C for 1h, (c) THP-4 stepped, (d) THP-2 stepped microstructures.

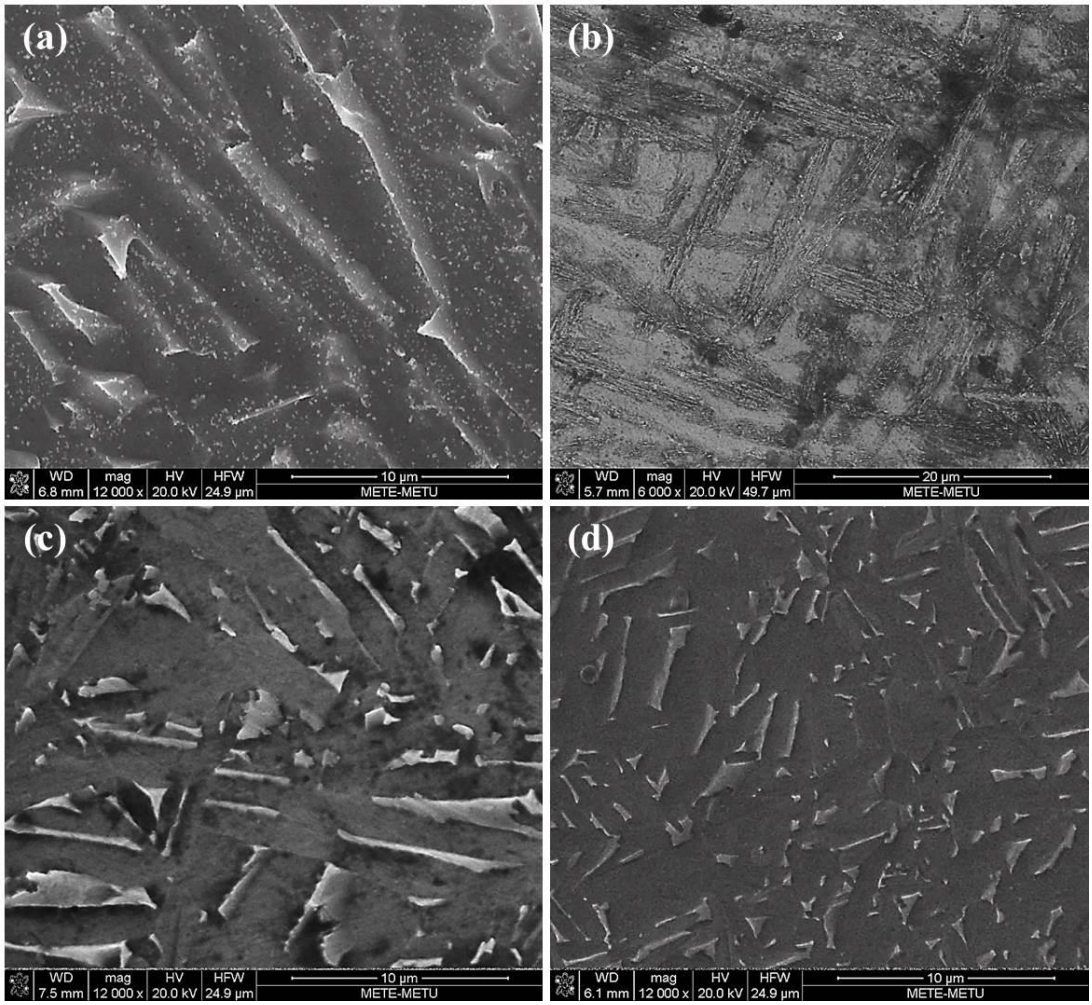

Figure 4. 22: SEM images of SLM+HIPped specimens; (a) initial, (b) hydrogenated at 650°C for 1h, (c) THP-4 stepped, (d) THP-2 stepped microstructures.

4.5. Mechanical Properties

In this chapter, mechanical properties after 2 and 4 steps THP were presented based on compression and tensile test results so as to reveal the yield strength and the elongation values of initial and THPed alloys. Moreover, the tensile fracture surfaces were also presented and the hardness values were displayed in this chapter in order to make a comprehensive analysis on the final mechanical characteristics of both SLM and SLM+HIPped samples.

4.5.1. Compression Test Results

4.5.1.1. SLM Fabricated Samples

The stress-strain curves, which illustrate the influence of 2- and 4-steps THP on the compression behavior of SLM fabricated alloys, are shown in Figure 4.23. The linear elastic region, which is defined as the deformation area where small strains are recoverable until the yield point, was observed to be highest in as-received samples possibly due to differences in hydrogen contents of as-received and dehydrogenated samples. Similarly, THP treatment lowered yield strengths of the alloys as it is also a kind stress-relief process and it lowers hydrogen content and converts hard α'-martensitic phase to relatively soft equilibrium α and β phases, Figure 4.21. Similarly, load carrying capacities of samples were different. Both as-received and 2-step THP samples displayed similar peak strengths, while 4-step THP sample's peak strength was considerably lower. Although both 2 and 4-step THP induced similar refined microstructures including fine α and β-phases, previous β-grain size was significantly higher (~496 μm) in 4-step THP samples with respected to starting alloy (~71 μm) due to coarsening during β-solutionizing treatment. On the other hand, 2-step treatment did not alter the grain size of the starting alloy considerably and around 15 % increment was observed in ductility mainly due to stress-relieving effect.

In Table 4.3, mechanical responses of the samples under quasi-static compression loading are numerically presented with maximum compressive strength, yield strength and compressive strain values at fracture. The compressive strain of 4-step THP sample was quite lower due to the higher β grain size (~496 μm) when compared to the starting (~71 μm) and 2-step THP (~84 μm) samples. Moreover, the compressive strength value was lower for 4-step THP sample because of the grain coarsening and primary α-phase formation along the previous β-phase grain boundaries as shown in Figure 4.19(a).

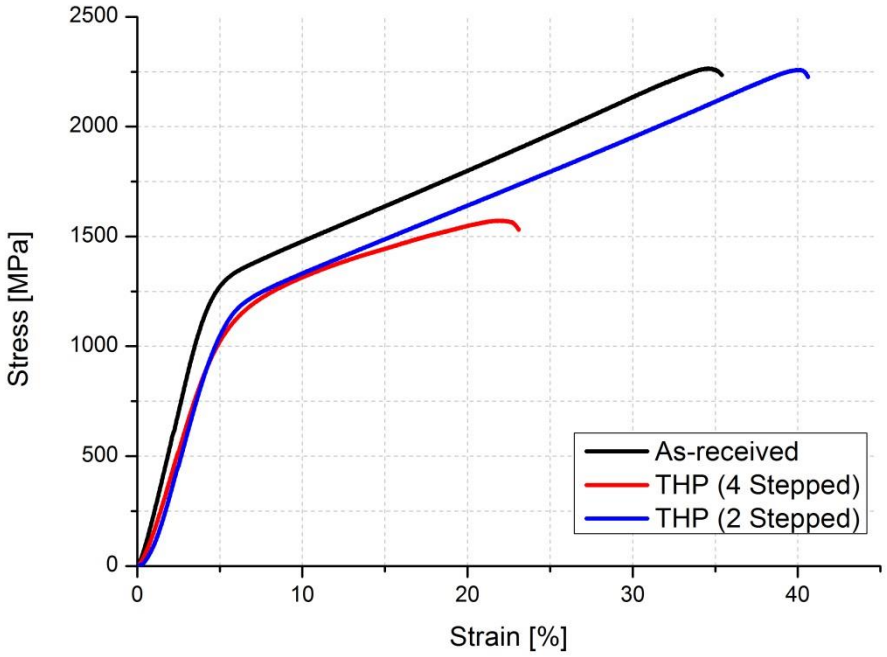

Figure 4. 23: Stress-strain curves of SLM fabricated as-received, THP-4 stepped and THP-2 stepped alloys.

Table 4. 3: Average compression test results of SLM fabricated specimens

Sample	Yield Strength (MPa)	Compressive Strength (MPa)	Compressive Strain at fracture (%)
As-received	1328.4	2265.3	35.4
THP (4 Step)	1200.3	1572.6	23.1
THP (2 Step)	1230.4	2257.9	40.6

4.5.1.2. SLM + HIPped Samples

Figure 4.24 presents stress-strain curves of SLM fabricated and subsequently HIPped samples. The mechanical response of 2 step-THP Ti-6Al-4V alloy was better than the SLM+HIPped as-received sample in terms of maximum compressive strength and ductility. In contrast, the mechanical properties as well as the ductility of the alloy reduced as a result of 4-step THP. However, yield strength slightly increased after 4-step THP. The starting SLM+HIPped alloy was composed of relatively coarser lamellar microstructure (Figure 4.22(a)). Therefore, increase in maximum strength after 2-step treatment was attributed to microstructural refinement; see Figure 4.22(d), while the ductility increment was possibly due to stress-relieving. On the other hand, 4-step treatment including β solutionizing and eutectoid decomposition led to a considerable decrease in the mechanical properties mainly due to excessive grain growth. Average values of the mechanical properties of SLM+HIPped samples are demonstrated in Table 4.4.

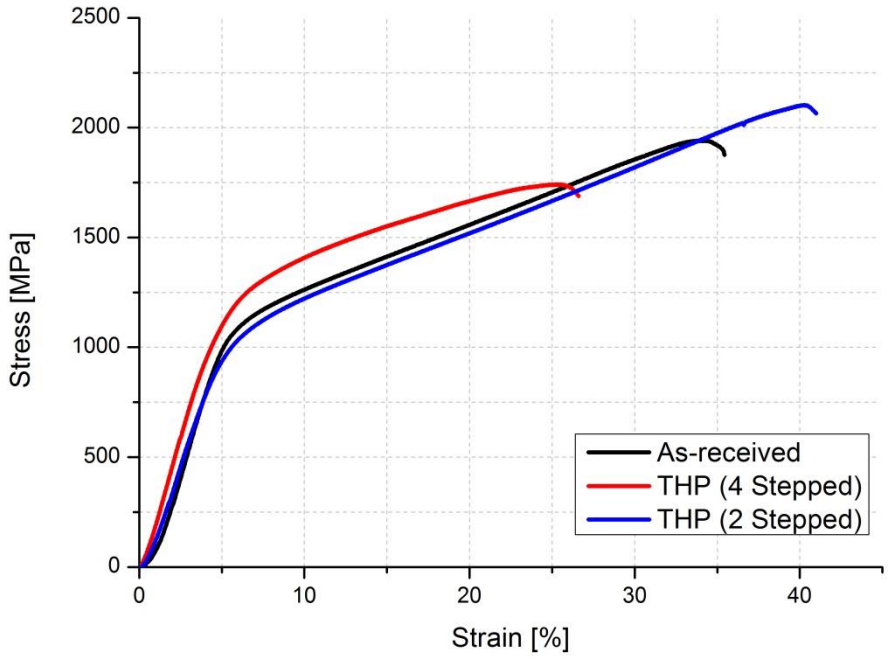

Figure 4. 24: Stress-strain curves of SLM + HIPped as-received, THP-4 stepped and THP-2 stepped alloys.

Table 4. 4: Average compression test results of SLM+HIPped specimens.

Sample	Yield strength (MPa)	Compressive strength (MPa)	Compressive strain at fracture (%)
As-received	1116.0	1941.1	35.4
THP (4 Step)	1216.3	1741.9	26.6
THP (2 Step)	1104.8	2102.7	41.0

4.5.2. Tensile Test Results

The tensile test results were conducted by using dumbbell shaped tensile test specimens as described in Chapter 3.4.4 for two different sets of initial specimens. The nominal stress-strain diagrams were used to determine the tensile mechanical properties such as yield strength, ultimate tensile strength (UTS) and elongation.

4.5.2.1. SLM Fabricated Samples

The stress-strain diagrams obtained from tensile tests reveal that as-received SLM alloy had the highest yield strength along with the relatively moderate ductility as shown in Figure 4.25. The high yield and tensile strength, and low ductility undoubtedly resulted because of the α'-martensitic phase that was initially present in the microstructure of SLM as-received alloy. Furthermore, extremely high thermal inputs during interaction with laser induced internal stresses led lower ductility as compared to defined in the ASTM standard (Table 4.5).

The microstructure containing α'-martensitic phase in as-received samples transformed to fine α and β phases when THP was applied. Therefore, the yield strength of the THPed samples were decreased around 5 and 10 %, respectively, for

4-step and 2-step THP samples. Yet, the yield strengths of THPed samples were still noticeably higher and in the acceptable range defined by ASTM F2924-14 standard, Table 4.5. However, 4-step THP sample had the lowest ductility although its microstructure was found to be similar to that of 2-step THP sample, Figure 4.16(c) and 4.21(b). The only microstructural difference between these two THPed samples was their grain size and the presence of grain boundary α. As stated previously, β-solutionizing in 4-step THP changed initial β grain size of starting sample from ~71 to ~496 μm. This grain growth caused a preposterous decrease in the mechanical properties, particularly in elongation as Figure 4.25 clearly illustrates. In contrary, when dehydrogenation was applied right after the hydrogenation step, ductility of SLM fabricated Ti-6Al-4V increased due to stable grain structure accompanied with transformation of α' martensitic phase to fine α+β phases and stress relieving effect. Although 4-step THP and as-received samples had similar ductility, around 100 % increase was observed in ductility after 2-step THP. The yield strength and UTS of as-received and THP-4 stepped samples were rather higher than the ASTM F2924-14 standard, while elongations of both samples were far below the desired level, Table 4.5. For that reason, an alternative THP method like 2-step THP was required to perform with the purpose of improving the ductility.

Transverse and longitudinal cross sections, shown in Figure 4.26, were examined by cutting the SLM fabricated tensile test specimens in parallel and perpendicular directions to test direction. In Figure 4.26(a), the scanning strategy for tensile test samples was clearly observed from the grains, which were orientated parallel to the scanning direction. This parallel grain orientation was distorted when 4-step THP was applied because of the newly formed equiaxed grains during β solutionizing, Figure 4.26(c). The 2-step THP sample, Figure 4.36(e), was not β solutionized and thus parallel grains were still preserved in the microstructure. The longitudinal cross section evaluations illustrated in Figures 4.26(b), (d) and (e) evidently shows the presence of elongated grains along the building direction. Independent from β solutionizing treatment, the longitudinal cross sections of 4-step (Figure 4.26(d)) and 2-step THP (Figure 4.26(f)) samples contained elongated grains similar to the as-

received sample (Figure 4.26(b)). Also it must be noted that, the uniaxial tensile load direction was parallel to building direction for SLM fabricated samples.

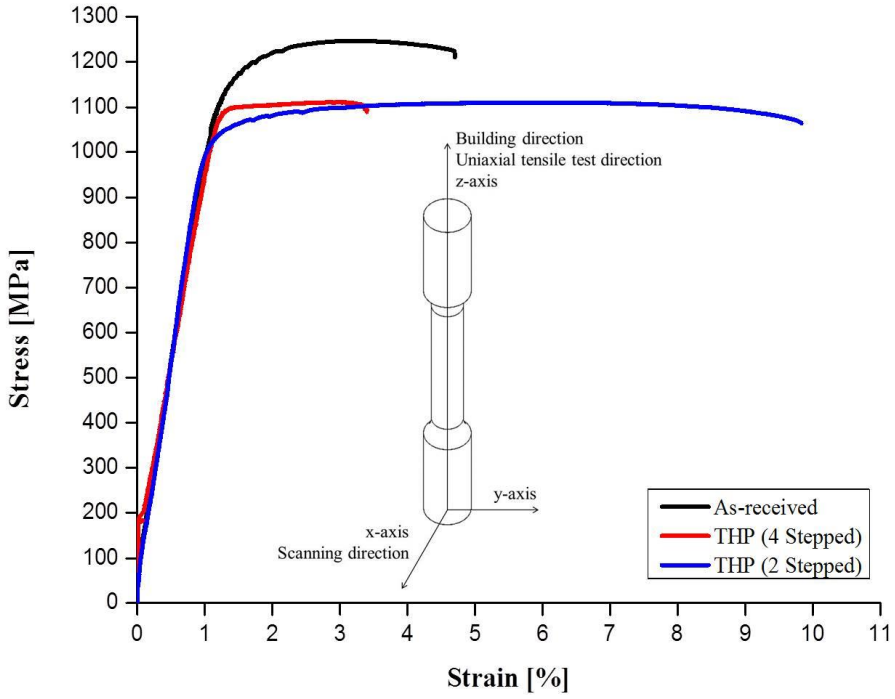

Figure 4. 25: Stress-strain curves of SLM fabricated; as-received, THP-4 stepped and THP-2 stepped alloys.

Table 4. 5: Average tensile test results of SLM fabricated specimens.

Sample	Yield strength (MPa)	Ultimate tensile strength (MPa)	Strain at fracture (%)
As-received	1141.5	1246.7	4.7
THP (4 Step)	1096.1	1110.9	3.5
THP (2 Step)	1035.1	1110.2	9.8
ASTM F2924-14	825.0	895.0	10.0

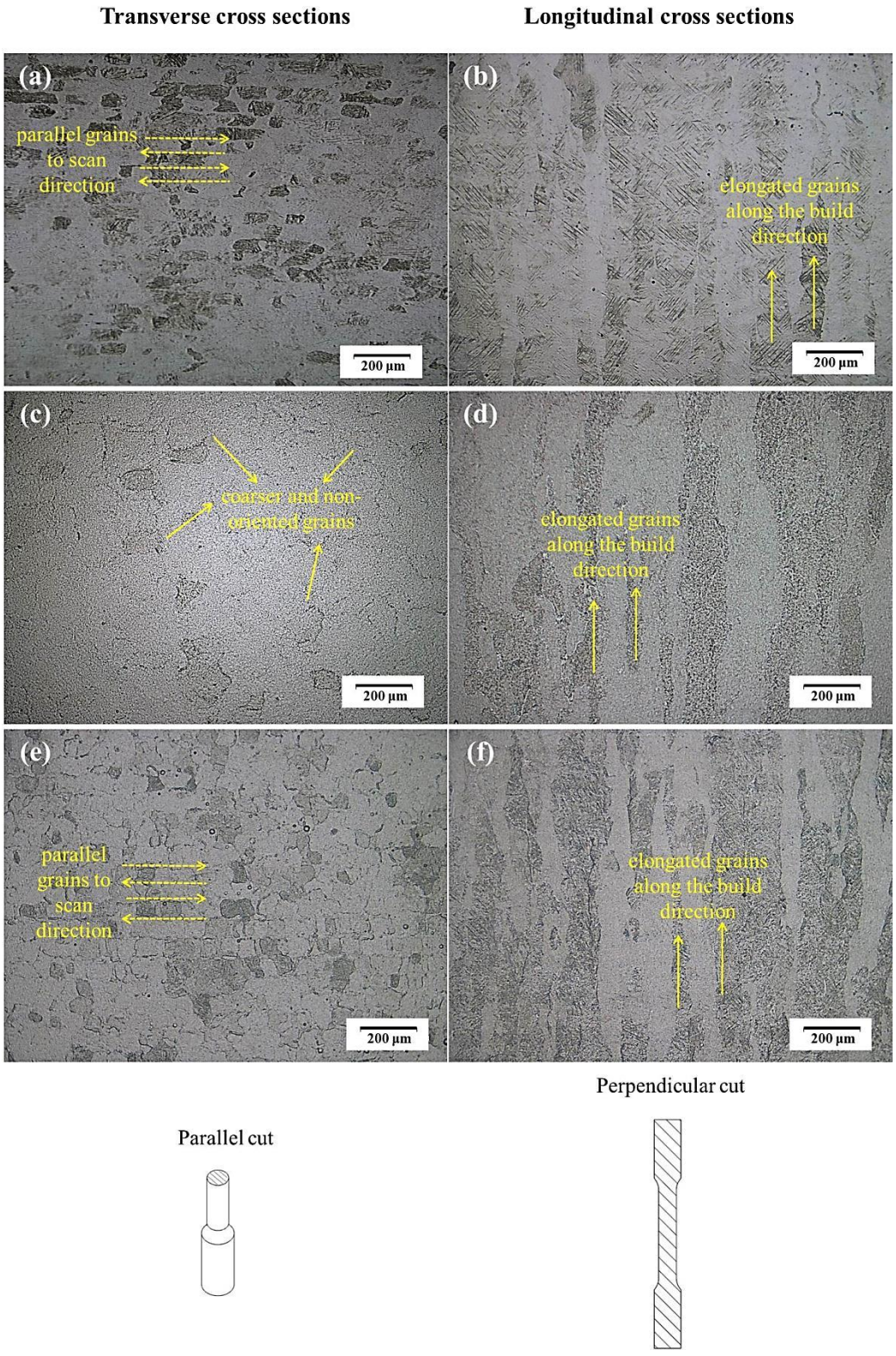

Figure 4. 26: Optical micrographs of; (a) parallel cut as-received, (b) perpendicular cut as-received, (c) parallel cut 4-step THP, (d) perpendicular cut 4-step THP, (e) parallel cut 2-step THP, (f) perpendicular cut 2-step THP tensile test samples.

The tensile test fracture surface morphologies of SLM fabricated samples are shown in Figure 4.27. The fresh fracture surface of SLM as-received alloy confirms its relatively moderate ductility with a shiny shear surface including partly equiaxed dimple regions, Figures 4.27, 4.28(a). Similarly, fracture surface of 4 step THP-4 sample verifies also its relatively brittle behavior with smooth and flat morphology, Figure 4.27(b). Moreover, there was no necking formed in 4-step THP sample, Figure 4.28(b). The fracture surface of 2 step-THP sample shown in Figure 4.27(c), reveals a ductile fracture with its equiaxed dimples as well as formation of necking, Figure 4.28(c). The positive impact of eliminating β solutionizing and eutectoid decomposition treatments on the ductility were proved once again with respect to the fracture surface evaluations on SLM fabricated specimens.

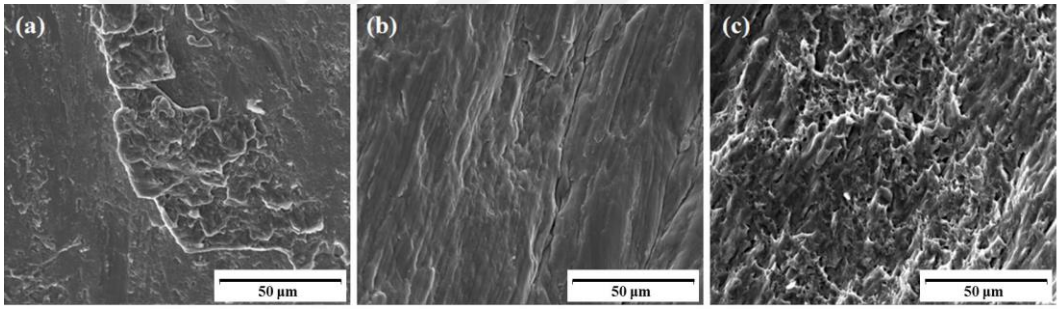

Figure 4. 27: SEM images illustrating the tensile test fracture surfaces of SLM fabricated; (a) as-received, (b) THP-4 stepped, (c) THP-2 stepped samples.

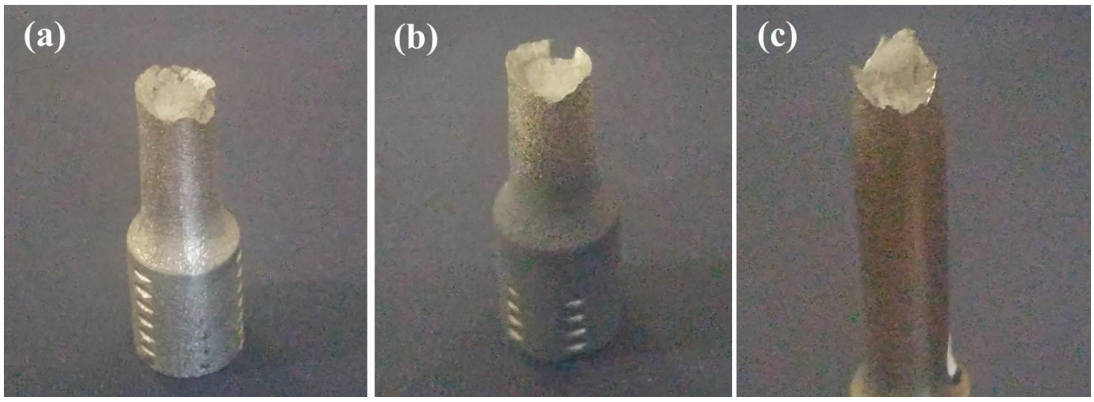

Figure 4. 28: Photos of the macro fracture surface of dumbbell shaped SLM fabricated tensile test; (a) as-received, (b) THP-4 stepped, (c) THP-2 stepped specimens.

4.5.2.2. SLM + HIPped Samples

The engineering stress-strain curve of SLM+HIPped as-received sample is shown in Figure 4.29. As-received SLM+HIPped samples exhibited higher ductility but lower UTS and yield strengths with respect to as-received SLM sample (with α'-martensitic structure) (Figure 4.25) due to their relatively coarser lamellar α+β structure. On the other hand, 4-step processed sample which was additionally β solutionized and eutectoid decomposed had lower strain at fracture since β solutionizing and eutectoid decomposition led to an increase β-phase grain size and formation of primary α grains.. The elongation of 4-step THP sample was only 5.2 % although this value was 12.6 % for as-received samples, as shown in Table 4.6. Eliminating β solutionizing and eutectoid decomposition steps allowed improving the elongation in 2-step THP sample by 10 % when compared to as-received tensile test specimen. However, the yield strength and the UTS of 2-step THP sample did not altered notably with respect to initial conditions. The mechanical properties of SLM + HIPped samples are summarized in Table 4.6.

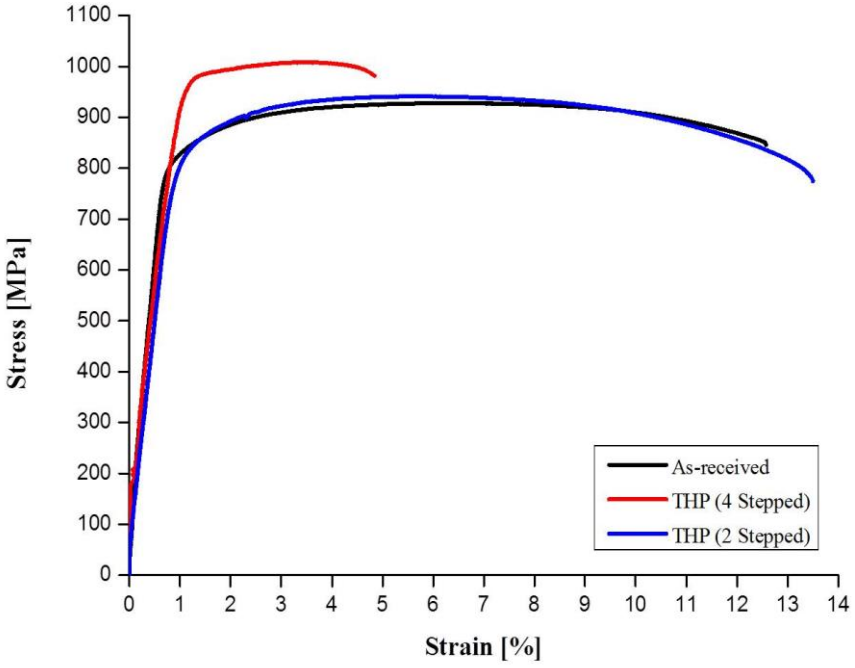

Figure 4. 29: Stress-strain curves of SLM + HIPped as-received, THP-4 stepped and THP-2 stepped alloys.

Table 4. 6: Average tensile test results of SLM + HIPped specimens

Sample	Yield strength (MPa)	Ultimate Tensile Strength (MPa)	Elongation (%)
As-received	814.2	927.9	12.6
THP (4-Step)	960.6	1008.6	5.2
THP (2-Step)	817.0	941.2	13.5
ASTM F2924-14	825.0	895.0	10.0

As shown in Figures 4.30 and 4.31(a), the fracture surfaces of as-received SLM + HIPped sample reveals a ductile fracture with equiaxed dimples. The flat and smooth fracture surface of the 4-step THP samples, illustrated in Figure 4.30(b), exhibits a brittle behavior with no neck formation during testing, Figure 4.31(b). On the other hand, 2-step THP samples' fracture surfaces contained equiaxed dimples indicating ductile behavior similar to starting samples; however, dimples were comparatively coarser, Figure 4.30(c). The slight necking during tensile test, pointed out that 2-step THP sample reveals a ductile fracture, as shown in Figure 4.31(c).

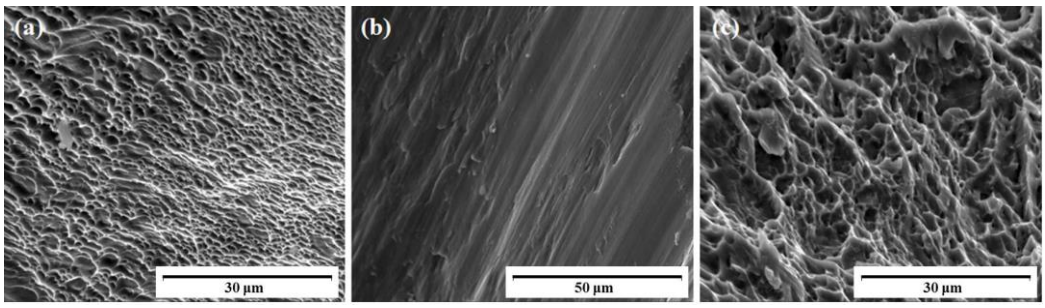

Figure 4. 30: SEM images illustrating the tensile fracture surfaces of SLM + HIPped; (a) as-received, (b) THP-4 stepped, (c) THP-2 stepped samples.

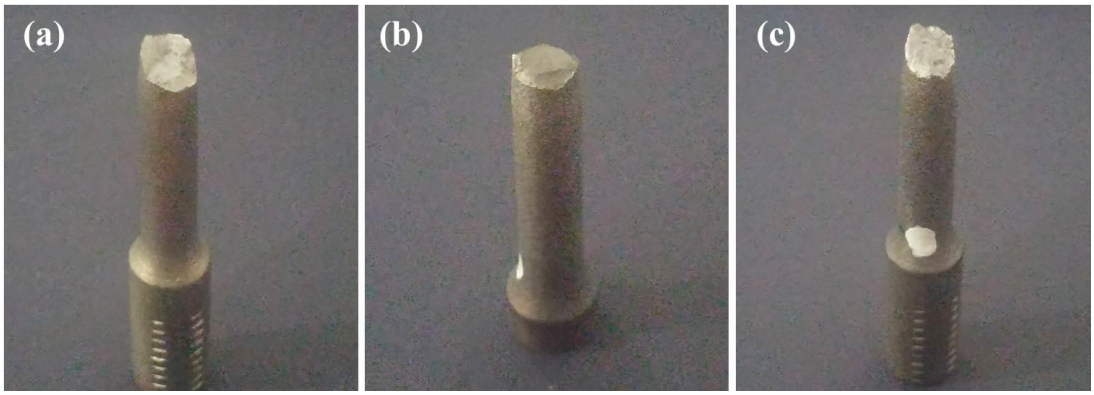

Figure 4. 31: Photos of macro fracture surface of dumbbell shaped SLM+HIPped tensile test; (a) as-received, (b) THP-4 stepped, (c) THP-2 stepped specimens.

4.5.3. Microhardness Measurements

At least 15 measurements were done randomly from the different areas of each sample using Vickers Hardness testing to have reliable results.

4.5.3.1. SLM Fabricated Samples

Figure 4.32 shows the hardness values for SLM fabricated alloys of as-received, hydrogenated, 4-step THP and 2-step THP. Hardness of as-received SLM sample was observed to be highest (400 ± 5 HV) among the SLM samples processed by various techniques. Relatively high hardness in the as-received SLM sample was attributed to α' martensite phase that was present in the starting microstructure. These results also agreed well with the tensile test results which clearly showed highest tensile strength for as-received SLM sample. The hardness measurements in SLM sample that was hydrogen treated at 650 °C for 1 h revealed a relatively lower hardness value with respect to starting sample since stress was relieved and additional δ and softer β-phases formation were observed in the structure (Figure 4. 10(a)) together with the coarsening of needle like structure (Figure 4.10(d)). Dehydrogenation treatment during either 2-step or 4-step THP; however, led to

decrease in hardness values compared to starting alloy and hydrogen treated alloy. Although both microstructure were fine, the δ phase and α'-martensitic phases disappeared completely (Figures 4.3(a) and (b)). Therefore, both THP treated samples displayed similar hardness after dehydrogenation step.

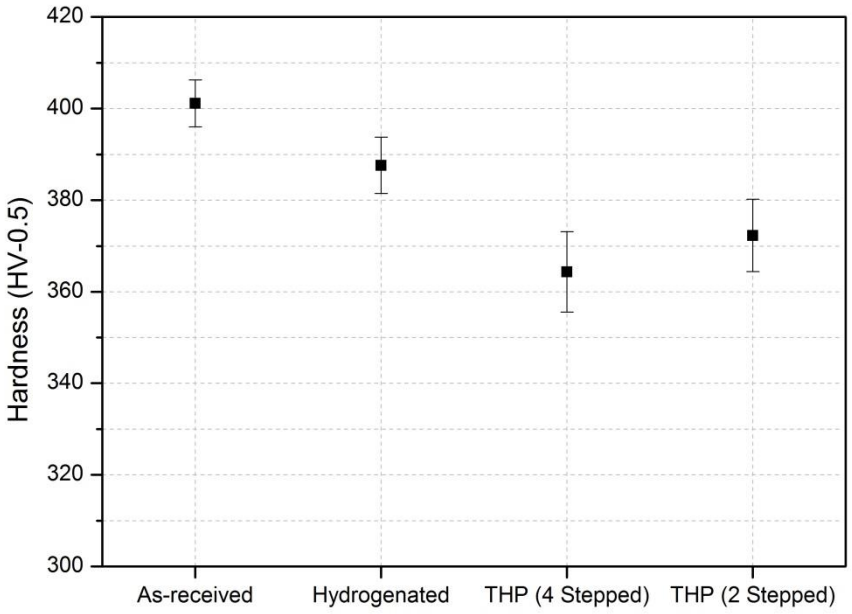

Figure 4. 32: Hardness values of SLM fabricated; as-received, hydrogenated, 4-step THP and 2-step THP samples.

4.5.3.2. SLM + HIPped Samples

Starting SLM+HIPped samples were observed to have lower Vickers hardness values, 340 ± 10, compared starting SLM samples, Figure 4.33. The hardness variation mainly arose from the difference in microstructures of starting samples. As-received SLM sample contained relatively harder α'-martensitic phase while relatively coarser Widmanstätten α+β was present in as-received SLM+HIPped sample. The hydrogen content of the sample was increased up to 1.17 wt.% as a result of hydrogenation at 650 °C for 1 h and thus, the hardness was considerably

increased. This relatively higher hydrogen concentration was sufficient for the formation of hydrogen rich δ phase (Figure 4.3(b)) which leads to an increase in hardness of Ti-6Al-4V. However, additional dehydrogenation in 2 or 4-step THP decreased hardness of samples due to disappearance of δ-phase (Figure 4.4) and formation of α+β phases. However, the hardness at the end of THP process was higher compared to starting alloy since relatively finer microstructure was obtained (Figures 4.16 and 4.22).

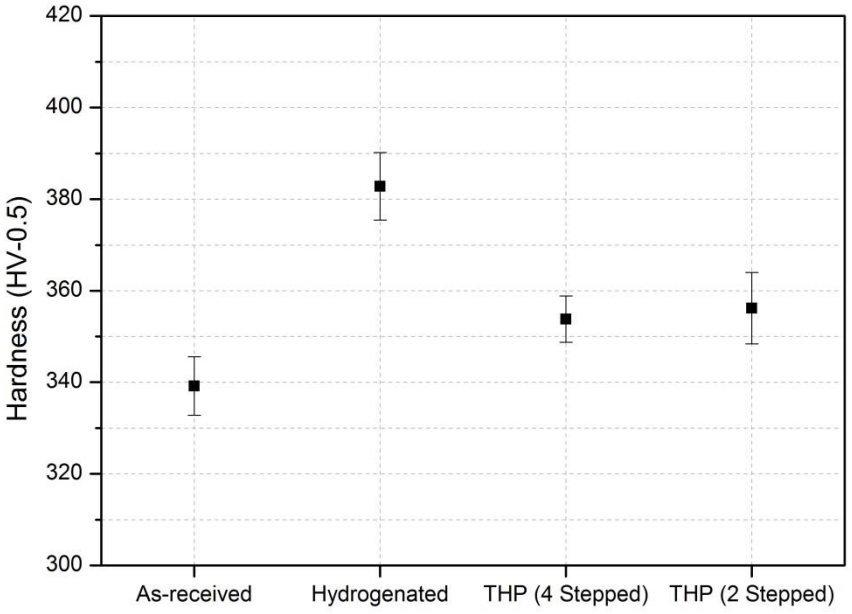

Figure 4. 33: Hardness values of SLM + HIPped; as-received, hydrogenated, 4-step THP and 2-step THP samples.

CHAPTER 5

CONCLUSIONS

The following conclusions can be drawn from the results of the current study:

1. Fabrication type of additive manufactured samples affects their microstructure, thereby, changing their mechanical properties. SLM fabricated as-received alloy composed of only hcp-α' martensitic phase, while the SLM sample which was HIPped additionally consisted of lamellar α and β phases. Therefore, yield strength and UTS of SLM fabricated samples were greater than the SLM+HIPped as-received alloy, and the values were found to be 1141.5, 1246.7 MPa and 814.2, 927.93 MPa, respectively. Besides, SLM samples with martensitic microstructure displayed lower ductility with around 4.70 % compared to 12.58 % ductility seen SLM+HIPped samples.

2. Fcc-δ hydride phase, which is the basic requirement for microstructural refinement, has been observed to occur hydrogenation (under 25 vol. % hydrogen + 75 vol. % argon atmosphere) at and above 650 °C since the necessary hydrogen levels were maintained at that temperatures. Additionally, hydrogen solubility curves obtained at various temperatures revealed a kind of distorted Gaussian curve with a maximum solubility of 1.19 wt.% H for SLM and 1.17 wt.% H for SLM+HIPped samples at 650 °C.

3. Hydride formation leads to a volume expansion of about 17.2 % and these conditions lead to widening and shifting of XRD peaks to lower 2θ

positions. Also, δ-phase peaks overlaps with that of α and α' phases, therefore, coexistence of these phases also broaden and widen the pattern. For that reason, making a structural interpretation from microstructure and diffraction patterns was not sufficient to differentiate each phases.

4. The β transus temperature was observed to decrease with increasing hydrogen content and 100 % β-phase formation was detected at 900 °C which is lower than the standard wrought Ti-6Al-4V alloys (~ 1000 – 1050 °C).

5. During eutectoid decomposition treatment in 4-step THP treatment, precipitation of both α and δ phases occurred together with α'-martensitic phase in some samples due to change in CCR by hydrogen solubility. Moreover, primary α-phase formation was also observed during eutectoid decomposition because of slow cooling rate.

6. Dehydrogenation treatment at 700 °C for 18 h was found to be optimum in terms obtaining fine microstructure containing α and β phases. Comparatively lower dehydrogenation temperatures did not alter the microstructure while higher temperatures resulted coarsening of fine α and β-phases. Additionally, dehydrogenation decreased the hydrogen content to a level (0.0019 wt. % for SLM, 0.0025 wt. % for SLM+HIPped) below the values defined by standards and also even below the starting samples' hydrogen contents (0.0042 wt. % for SLM, 0.0139 wt. % for SLM+HIPped).

7. 4-step THP process caused excessive grain growth even tough it resulted in transformation of α'-martensitic phase in SLM and relatively coarse α+β phase in SLM+HIP samples to a very fine microstructure composed discontinuous α and β phases. As a result of 4-step THP, initial β grain sizes were observed to increase from ~71 and ~108 μm to final ~496 and ~598

μm in SLM and SLM+HIPped alloys, respectively. Therefore, after 4-step THP, average elongations were decreased from 4.70 % to 3.47 %, and from 12.58 % to 5.22 % for SLM and SLM+HIPped samples.

8. Elimination of β-solutionizing and eutectoid decomposition in 2-step THP prevented grain growth and grain size remained almost the same since the temperature was never reached up to 100 % beta phase region. Moreover, this treatment resulted very fine microstructure (composed of fine discontinuous α and β-phases) similar to 4-step THP. Therefore, elongation values of SLM and SLM+HIPped samples increased to 9.83% and 13.52%.

9. Responses of the SLM and SLM+HIP samples to either 4- or 2-step THP were more or less the in terms of hydrogen solubility similar resultant microstructure obtained during THP; however, the relative difference between mechanical properties (compression, tensile and hardness) before and after THP were dissimilar because of the differences in starting microstructures.

10. THP process which is commonly used for microstructural refining of cast and powder metallurgy products of Ti-6Al-4V alloys can also be applied to SLM parts successfully to refine their microstructures and increase ductility without a need for hot deformation. Accordingly, the usage of SLM Ti-6Al-4V parts will be possible in load bearing applications of aerospace or medical industries.

The following future studies are recommended in order to improve microstructural refinement mechanism of hydrogenation and dehydrogenation phenomena in SLM fabricated Ti-6Al-4V.

- Transmission electron microscopy (TEM), Rietveld and focus ion beam scanning electron microscopy (FIB-SEM) studies are required to characterize each phase constituents particularly present in the

microstructure of hydrogenated samples. By doing this, fcc-δ phase could be resolved more accurately in the microstructure.

- It is suggested that thermo gravimetric analysis (TGA) and resistivity measurements might be conducted to determine phase transformations occurred during each step.

- THPed materials should be tested using fatigue tests to compare their endurance limit with their wrought alloy counterparts which are used in load bearing application of aerospace or biomedical industry.

- In this thesis, the hydrogen solubility of Ti-6Al-4V was studied at constant hydrogenation temperature and time. However, it is known that hydrogen solubility of Ti-6Al-4V alloy can also be increased with increasing hydrogen partial pressure. Therefore, further hydrogenation treatments could be carried out at different hydrogen pressures in order to investigate pressure dependent hydrogen solubility in Ti-6Al-4V.

REFERENCES

[1] Donachie, J. (2000). Titanium: A Technical Guide, 2nd Edition. Ohio: ASM International.

[2] Meetham, G. W. (1981). The Development of Gas Turbine Materials. Essex, England: Applied Science Publishers LTD.

[3] Allen, P. (1996). Titanium Alloy Development. Advanced Materials & Processes, 10, 35-37.

[4] Peters M., Hemptenmacher. J., Kupfert J., Lejens C. (2003). Structure and Properties of Titanium and Titanium Alloys, Titan. Titan. Alloy. Weinheim: Wiley-VCH Verlag.

[5] Liu X., Chu. P., Ding C. (2004). Surface modification of titanium, titanium alloys, and related materials for biomedical applications. Mater. Sci. Eng. R Reports, 47, 49–121.

[6] Nouri A., Hodgson P., Wen C. (2010). Biomimetic Porous Titanium Scaffolds for Orthopedic and Dental Applications. A. Mukherjee, Biomimetics Learn. From Nat (s. 415–451). Australia: InTech.

[7] Lütjering G., Williams J. (2007). Titanium. Springer.

[8] Materials Properties Handbook: Titanium Alloys. (1994). ASM International.

[9] Leyens C., Peters M. (2003). Titanium and Titanium Alloys: Fundamentals and Applications. Weinheim, Germany: Wiley-VCH.

[10] Froes F. H., Allen P., Niinomi M. (1998). Non-Aerospace Applications of Titanium. TMS, (P. 3). Warrendale.

[11] Rosenberg, W. (1970). The Science, Technology and Application of Titanium. Oxford, UK: Pergamon Press.

[12] Collings E. W. (1994). Materials Properties Handbook: Titanium Alloys. Materials Park, USA: ASM.

[13] Boyer, R. (1996). Titanium '95: Science and Technology. Cambridge: The University Press.

[14] Walter J., Jackson M., Sims C. (1988). Titanium and its alloys: Priciples of alloying titanium. Metals Park, USA: ASM International.

[15] Thiehsen K. E., (1993). The effect of nickel, chromium, and primary alpha phase on the creep behavior of Ti-6242Si. Met. Trans. A, 24A, 1819-1826.

[16] Seagle S. R., Hall G., Boomberger H. (1972). Met.Eng. Q, 48-54.

[17] Lütjering G. (1998). Influence of Processing on Microstructure na Mechanical Properties of (α + β) Titanium Allyos. Materials Science and Engineering, A243, 23-45.

[18] Damkroger B. K., Edwards G. (1990). Continuous cooling transformation kinetics in alpha-beta titanium alloys. Simulation and Theory of Evolving Microstructures, The Metals, Minerals & Materials Society, 129-150

[19] Atlas of Microstructures of Industrial Alloys (8^{th}, 7b). (1972). Metals Handbook.

[20] Lee Y. T, Peters M., Welsch G. (1999). Metallurgical and Materials Transactions A (22A).

[21] Bremen S., Meiners W., Diatlov (2012). A. Selective laser melting: A manufacturing technology for the future? Laser Technik Journal, 9(2), 33-38.

[22] Wohlers T. T. (2009). Rapid prototyping & tooling sate of the industry. Detroit: Wohlers Associates.

[23] Sachs E. M, Clima M., Williams, Brancazio D., Cornie J. (1992). Three dimensional printing: rapid tooling and prototypes directly from Cad model. Journal of Engineering for Industry, 481-488.

[24] Jacops P. F. (1995). Stereolithography and other PP and M technologies: from rapid prototyping to rapid tooling. New York: SME.

[25] Hopkinson N., Hague R., Dickens P. (2006). Rapid Manufacturing: An Industrial Revolution for the Digital Age. Chichester: John Wiley & Sons, Ltd.

[26] Burns M. (1993). Automated fabrication: improving productivity in manufacturing. Upper Saddle River, NJ, USA: Prentice-Hall, Inc.

[27] Gibson I., Rosen D., Stucker B. (2015). Additive Manufacturing Technologies: 3D printing, rapid prototyping and direct digital manufacturing. New York: Springer.

[28] Chua C. K, Leong K., Lim C. (2003). Sing Rapid Prototyping- Principles and Applications (2nd Edition). Singapore: World Scientific Publishing Co. Pte. Ltd.

[29] Murr L. E., Gaytan S., Ramirez D., Martinez E., Martinez J., Hernandez J., Amato K., Shindo P., Medina F., Wicker R. (2012). Metal fabrication by additive manufacturing using laser and electron beam melting technologies. Journal of Materials Science & Technology, 1-14.

[30] Thompson S., Bian L., Shamsaei N., Yadollahi A. (2015). An Overview of Direct Laser Deposition for Additive Manufacturing; Part I: Transport Phenomena, Modeling and Diagnostics. Journal of Additive Manufacturing , 36-62.

[31] Gu D. D., Meiners W., Wissenbach K., Poprawe R. (2012). Laser additive manufacturing of metallic components: materials, processes and mechanisms. International Materials Reviews, 133-164.

[32] Venuvinod P. K., Ma W. (2001). Rapid prototyping: laser-based and other technologies (1st b.). Norwell,: Kluwer Academic Publishers.

[33] Wu X. (2007). A review of laser fabrication of metallic engineering components and of materials. Materials Science and Technology, 631-640.

[34] Kruth J. P., Levy. G., Klocke F., Childs T. (2007). Consolidation phenomena in laser and powder-bed based layered manufacturing. CIRP Annals - Manufacturing Technology, 730-759.

[35] Lü L., Fuh J., Wang Y. (2001). Laser-induced materials and processes for rapid prototyping. Norwell: Kluwer Academic Publishers.

[36] Arcam. Arcam Brochure. June 6, 2016. Web Site: http://www.arcam.com/wp-content/uploads/justaddbrochure-web.pdf.

[37] Larsson M., Lindhe U., Harrysson O. (2003). Rapid Manufacturing with Electron Beam Melting (EBM) – A manufacturing revolution? Austin: University of Texas.

[38] Kruth J. P., Mercelis P., Vaerenbergh J., Frogen L., Rombouts M. (2005). Binding mechanisms in selective laser sintering and selective laser melting. Rapid Prototyping Journal, 26 - 36.

[39] Poprawe R., Loosen P., Hoffmann H. (2007). The future of high power laser techniques. 16th Int. Symp. on 'Gas flow chemical lasers, and high-power lasers'. Gmunden, Austria: SPIE.

[40] Santosa E. C., Shiomia M., Osakadaa K., Laouib T. (2006). Rapid manufacturing of metal components by laser forming. International Journal of Machine Tools and Manufacture, 1459–1468.

[41] Schleifenbauma H., Meinersa. W., Wissenbacha K., Hinkeb C. (2010). Individualized production by means of high power Selective Laser Melting. CIRP Journal of Manufacturing Science and Technology, 161–169.

[42] Shiomi M., Osakada, Nakamura K., Yamashita T., Abe F. (2004). Residual Stress within Metallic Model Made by Selective Laser Melting Process. CIRP Annals - Manufacturing Technology, 195-198.

[43] Booth G. (2005). Manufacturing with Lasers Developments and Opportunities. Welding in the World, 16-20.

[44] Atwood C., Ensz M., Greene D. (1998.). Laser engineered net shaping (LENS(TM)): a tool for direct fabrication of metal parts. 17th International Congress on Applications of Lasers and Electro-Optics. Orlando.

[45] Palčiča I., Balazic M., Milfelnarc M., Buchmeistera B. (2009). Potential of Laser Engineered Net Shaping (LENS) Technology. Materials and Manufacturing Processes, 750-753.

[46] Taminger K., Hafley R. (2006). Electron Beam Freeform Fabrication. NASA Technical, Paper No. TM-2006-214284.

[47] Edwards P., O'Conner A., Ramulu M. (2013). Electron Beam Additive Manufacturing of Titanium Components: Properties and Performance. ASME J. Manuf. Sci. Eng, 061016.

[48] Liu W., DuPont J. (2003). Fabrication of functionally graded TiC/Ti composites by laser engineered net shaping. Scripta Materialia, 1337–1342.

[49] Banerjee R., Collins P., Genç A., Froser H. (2003). Direct laser deposition of in situ Ti–6Al–/4V–/TiB composites. Materials Science and Engineering: A, 343–349.

[50] Bontha S., Klingbeil N., Kobryn P., Fraser H. (2009). Effects of process variables and size scale on solidification microstructure in beam-based fabrication of bulky 3D structures. Materials Science and Engineering: A, 311–318.

[51] Hofmeister W., Griffith M. (2001). Solidification in direct metal deposition by LENS processing. JOM, 30-34.

[52] Li, Xiang, Wang, Chengtao, Zhang, Wenguang, Li (2009). Fabrication and characterization of porous Ti6Al4V parts for biomedical applications using electron beam melting process. Materials Letters, 403-405.

[53] Thijs L., Verhaeghe F., Craeghs T., Van Humbeeck J., Kruth J. (2010). A study of the microstructural evolution during selective laser melting of Ti-6Al-4V. Acta Materialia, 3303-3312.

[54] Al-Bermani S., Blackmore M., Zhan W., Todd I. (2010). The Origin of Microstructural Diversity, Texture and Mechanical Properties in Electron Beam Melted Ti-6Al-4V. Metallurgical and Materials Transactions A, 41(13), 3422-3434.

[55] Baufeld B., Biest O., Gault R. (2010). Additive manufacturing of Ti6Al4V components by shaped metal deposition: Microstructure and mechanical properties. Materials & Design, 31, S106–S111.

[56] Das S., Wohlert M., Beaman J., Bourell D. (1999). Processing of titanium net shapes by SLS/HIP. Materials and Design 20, 115-121.

[57] Facchini L., Magalini E., Robotti P., Molinari A., Höges S., Wissenbach K. (2010). Ductility of a Ti-6Al-4V alloy produced by selective laser melting of prealloyed powders. Rapid Prototyping Journal, 450-459.

[58] Facchini L., Magalini E., Robotti P., Molinari A. (2009). Microstructure and mechanical properties of Ti-6Al-4V produced by electron beam melting of pre-alloyed powders. Rapid Prototyping Journal, 171-178.

[59] Kalinyuk A. N., Trigub N., Zamkov V., Ivasishin G., Markovsky P., Teliovich R., Semiatin S. (2003). Microstructure, texture, and mechanical properties of electron-beam melted Ti-6Al-4V. Materials Science and Engineering, A346, 178-188.

[60] Murr L. E., Esquivel E., Quinones S., Gaytan S., Lopez M., Martinez E., Medina F., Hernandez D., Martinez E., Martinez J., Stafffard S., Brown D., Hoppe T., Meyers W., Lindhe U., Wicker R. (2009). Microstructure and mechanical behavior of Ti-6Al-4V produced by rapid-layer manufacturing, for biomedical applications. Journal of the Mechanical Behavior of Biomedical Materials, 20-32.

[61] Rafi H. K., Karthik N., Gong H., Starr T., Stucker B. (2013). Microstructures and Mechanical Properties of Ti6Al4V Parts Fabricated by Selective Laser Melting and Electron Beam Melting. Journal of Materials Engineering and Performance, 22(12), 3872-3883.

[62] Brandl E., Leyens C., Palm F., Schoberth A., Onteniente P. (2008). Wire instead of powder? Properties of additive manufactured Ti-6Al-4V for aerospace applications. in Euro-uRapid. Fraunhofer-Allianz: Berlin, Germany.

[63] Kruth J. P., Leu M., Nakagawa T. (1998). Progress in Additive Manufacturing and Rapid Prototyping. CIRP Annals - Manufacturing Technology, 525-540.

[64] Heinl P., Korner C., Singer R. (2008). Selective Electron Beam Melting of Cellular Titanium. Mechanical Properties. Advanced engineering materials, 10, 882-888.

[65] Porter D. A., Easterling K., Sherif M. (2009). Phase transformations in metals and alloys. Boca Raton, FL: CRC Press.

[66] Optomec. (2016, 1). LENS MR-7. July 24, 2016. Web site: http://www.optomec.com/wp-content/uploads/2014/04/LENS_MR-7_WEB.pdf

[67] Brandl E., Michailov V., Viehweger B., Leyens C. (2011). Deposition of Ti–6Al–4V using laser and wire, part II: Hardness and dimensions of single beads. Surface & Coatings Technology, 206, 1130-1141.

[68] Baufeld B., Brandl E., Van der Biest O. (2011). Wire based additive layer manufacturing: Comparison of microstructure and mechanical properties of Ti–6Al–4V components fabricated by laser-beam deposition and shaped metal deposition. Journal of Materials Processing Technology, 211, 1146–1158.

[69] Vilaro T., Colin C., Bartout J. (2011). As-Fabricated and Heat-Treated Microstructures of the Ti-6Al-4V Alloy Processed by Selective Laser Melting. Metallurgical and Materials Transactions A, 3190-3199.

[70] Thöne M., Leuders S., Riemer A., Tröster T., Richard H. (2012). Influence of heat-treatment on Selective Laser Melting products – e.g. Ti6Al4V. 492-498.

[71] Vrancken B., Thijs L., Kruth J., Humbeeck J. (2012). Heat treatment of Ti6Al4V produced by Selective Laser Melting: Microstructure and mechanical properties. Journal of Alloys and Compounds, 177-185.

[72] Froes F. H., Senkov O., Qazi J. (2004). Hydrogen as a temporary alloying element in titanium alloys: thermohydrogen processing. International Materials Review, 49, 227-245.

[73] Nosov V. K., Ouchinnikow A., Shchugorev Y. (2008). Applications of hydrogen plasticizing of titanium alloys. Metal Science and Heat Treatment Journal, 50(7-8), 378-382.

[74] Yoshimura H., Kimura K., Hayashi M., Ishii M., Hanamura T., Takamura J. (1994). Ultra-fine Equiaxed Grain Refinement and Improvement of

Mechanical Properties of α+β Type Titanium Alloys by Hydrogenation, Hot Working, Heat Treatment and Dehydrogenation. Materials Transactions, JIM, 35, 266-272.

[75] Senkov O. N., Konopleva E., Ponyatovsky E. (1994). Microstructure/Properties Relationships of Titanium Alloys. TMS, 207-214.

[76] Kerr W. R. (1985). The effect of hydrogen as a temporary alloying element on the microstructure and tensile properties of Ti-6Al-4V. Metallurgical and Materials Transactions A, 16(6), 1077-1087.

[77] Paton N. E., Hickman B., Leslie D. (1971). Behavior of hydrogen in α-phase Ti-Al alloys. Metallurgical Transactions, 2(10), 2791-2796.

[78] Matthews L., Knutsen R. (2010). Embrittlement of the Ti-6Al-4V alloy by hydrogen dosing at elevated temperatures. SAIMM, 111, 155-158.

[79] Senkov O. N., Dubois M., Jonas J. (1996). Elastic moduli of titanium-hydrogen alloys in the temperature range 20 °C to 1100 °C. Metallurgical and Materials Transactions A, 27(12), 3963–3970.

[80] Ilynn A. A., Kolachev B., Mamonov A. (1992). Phase and structure transformations in titanium alloys under thermohydrogenous treatment, Titanium 92: Science & Technology. 941-947. Warrendale, PA: TMS.

[81] Qazi J., Rahim J., Froes F., Senkov O., Genç A., (2001). Phase transformations in Ti-6Al-4V-x H alloys. Metallurgical and Materials Transactions A, 32(10), 2453-2463.

[82] Fang T., Wang W. (1998). Microstructural features of thermochemical processing in a Ti-6Al-4V alloy. Materials Chemistry and Physics, 56(1), 35-47.

[83] Wasilewski R. J., Kehl G. (1954). Diffusion of Hydrogen in Titanium. Metallurgica, 50, 225-230.

[84] Zhang Y., Zhang S. (1997). Hydrogenation Characteristics of Ti-6Al-4V Cast Alloy and Its Microstructural Modification by Hydrogen Treatment. International Journal of Hydrogen Ennergy, 22, 161-168.

[85] Lopez-Suarez A., Richards J., Trejo-Luna R., (2003). Analysis of hydrogen absorption by Ti and Ti-6Al-4V using the ERDA technique. International Journal of Hydrogen Energy, 28(10), 1107-1113.

[86] Manchester F. D., San-Martin A. (2000). H-Ti(hydrogen-titanium). Phase Diagrams of Binary Hydrogen Alloys. 238-258. Materials Park, OH 44073-0002, USA: ASM International.

[87] Zhao J., Ding H., Zhong Y., Lee C. (2008). Influence of hydrogenation on microstructures and microhardness of Ti6Al4V alloy. Transactions of Nonferrous Metals Society of China, 18(3), 506-511.

[88] San-Martin A., Manchester F. (1987). Bulletin of alloy phase diagrams (1st 8b). Springer US.

[89] Paton N.E., Williams J. (1976). B. I. Thompson A.W. içinde, Effect of Hydrogen on Behavior of Materials. 409–432. New York, NY: AIME.

[90] Nelson H. G, Thompson A. W. (1996), Hydrogen Effects in Metals. 699–715. Warrendale, PA: TMS.

[91] Gerberich W. W., Moody N., Jensen C., Hayman C., Javatavallabhula K. (1981). B. I. Thompson A. W. içinde, Hydrogen Effects in Metals. 731–744. Warrendale, PA: TMS-AIME.

[92] Williams J. C., Thompson A. W. (1976). Effect of Hydrogen on Behavior of Materials. 367–380. New York, NY: AIME.

[93] Shen C. C., Perng T. (2007). Pressure–composition isotherms and reversible hydrogen-induced phase transformations in Ti–6Al–4V. Acta Materialia, 55, 1053–1058.

[94] Sun Z., Zhou W., Hou H. (2009). Strengthening of Ti–6Al–4V alloys by thermohydrogen processing. International Journal of Hydrogen Energy, 34, 1971-1976.

[95] Guitar A., Vigna G., Luppo M. (2009). Microstructure and tensile properties after thermohydrogen processing of Ti–6Al–4V. Journal of Mechanical Behavior of Biomedical Materials 2, 156-163.

[96] Tun-Ying Fang, Wen-Hsiung W. (1998). Microstructural features of thermochemical processing in a Ti-6Al-4V alloy. Materials Chemistry and Physics, 56, 35-47.

[97] Oguh J.C. (2008). Investigations of the Microstructural Evolution in Ti-6Al-4V Alloy During Cyclic Hydrogenation and Dehydrogenation Heat Tretment. Cape Town: University of Cape Town.

[98] Niinomi M., Gong B., Kobayashi T., Ohyabu Y., Toriyama O. (1995). Fracture characteristics of Ti-6Al-4V and Ti-5Al-2.5Fe with refined microstructure using hydrogen. Metallurgical and Materials Transactions, 26(5), 1141-1151.

[99] Shen C. C., Yu. C., Perng T. (2009). Variation of structure and mechanical properties of Ti-6Al-4V with isothermal hydrogenation treatment. Acta Materialia, 57(3), 868-874.

[100] Luo L., Su Y., Guo J., Fu H. (2006). Formation of titanium hydride in Ti-6Al-4V alloy. Journal of Alloys and Compounds, 425(1-2), 140-144.

[101] Shan D. B., Zang Y., Lu T., Lv Y. (2008). The effect of hydrogen on the strengthening and softening of Ti-6Al-4V alloy. Scripta Materialia, 58(6), 449–452.

[102] Shan D. B., Zang Y., Lv Y., Guo B. (2007). Microstructural evolution and formation mechanism of FCC titanium hydride in Ti-6Al-4V-xH alloys. Journal of Alloys and Compounds, 427(1-2), 229–234.

[103] Qazi J. I., Senkov O., Rahim J., Froes F. (2003). Kinetics of martensite decomposition in Ti-6Al-4V-xH alloys. Materials Science and Engineering, A359, 137-149.

[104] Zhao J., Ding H., Zhaow, Tianx, Hou H., Wang Y. (2010). Effect of thermo hydrogen treatment on lattice defects and microstructure refinement of Ti6Al4V alloy. International Journal of Hydrogen Energy, 35(12), 6448-6454.

[105] Mur F. X. G., Rodriguez D., Planell J. (1996). Influence of tempering temperature and time on the α′-Ti-6Al-4V martensite. Journal of Alloys and Compounds, 234(2), 287-289.

[106] Senkov O. N., Froes F. (1999). Thermohydrogen processing of titanium alloys. International Journal of Hydrogen Energy, 24(6), 565–576.

[107] Bashkin I. O., Malyshev V., Aksenov Y. (1990). Influence of hydrogen on the plasticity and resistance to deformation of titanium alloy VT6 at temperatures up to 930oC. Physics of metals and metallography, 69(5), 158-164.

[108] Ovchinnikov A. V., Ilyin A., Nosov V., Shchugorev Y (2007). Effect of phase composition and deformation conditions on the hydrogen plasticization of hydrogen-containing titanium alloys. Russian Metallurgy (Metally), 2007(5), 402–407.

[109] Fogagnolo J. B., Sallica-Leva E., Lopes E., Jardini H., Caram R. (2012). The effect of the laser processing parameters in the microstructure and mechanical properties of Ti6Al4V produced by selective laser sintering/melting. International conference on metallurgy and materials. Brno: TangerLtd.

[110] Zhu T., Li M. (2011). Lattice variations of Ti-6Al-4V alloy with hydrogen content. Materials Characterization, 62, 724-729.

APPENDIX A

THE GAS PRESSURE CALCULATION

As PASCAL'S LAW states the pressure applied to a fluid increases the pressure of the fluid at same level throughout the same amount. It is also known that pressure in a fluid increases with depth because more fluid molecules rests on deeper sections.

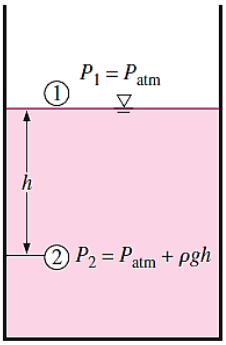

Figure A. 1: Pressure at depth of "h" in a fluid

Therefore, at a depth of ''h'' in a fluid (at point 2) shown in Figure A.1, the pressure will be;

$$P_2 = P_1 + \rho gh \qquad (A.1)$$

Where, P_2 is the pressure (Pascal; Pa(N/m^2))inside the fluid at a depth of h, P_1 is the atmospheric pressure (Pa), ρ is the density of fluid (kg/m^3) and h is the depth of the point in fluid (m).

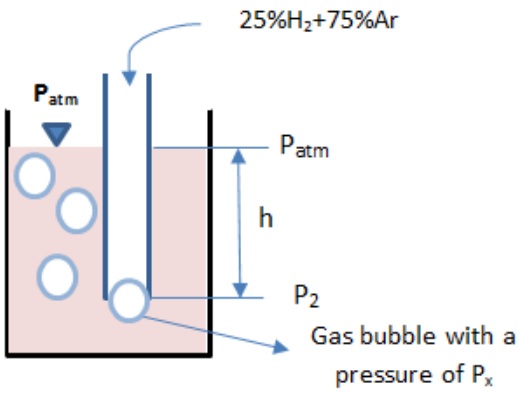

Figure A. 2: Gas bubbles containing 25%H_2+75%Ar

The gas bubble composed of 25%H_2+75%Ar should have pressure (P_x) higher than or at least equivalent to P_2 (the pressure of fluid at a depth of ''h''. (Figure A.2)

$$P_x \geq P_2 \qquad \text{where;} \qquad P_2 = P_{atmosphere} + \rho g h \qquad (A.2)$$

In the bubbler, the fluid was oil with a density of 864 kg/m^3. The atmospheric pressure, $P_{atmosphere}$, in Ankara and measured depth of pyrex pipe in oil were 98.05 Pa and 0.02 m, respectively. Therefore,

$$P_2 = 98.05Pa + (864\frac{kg}{m^3})(9.81\frac{m}{s^2})(0.02m) \qquad (A.3)$$

$$P_2 = 267.57Pa = 2.64atm \qquad (A.4)$$

APPENDIX B

Table B. 1: Thermo hydrogen process variables

Name of treatment	Temperature (°C)	Previous treatment	Heating / Cooling rate (°C/min) and time (min) to reach desired T.	Heating / Cooling atmosphere	Holding time (h)	Holding atmosphere	Cooling rate (°C/min) and time (min) to reach down to temp Tx	Final temperature after cooling, Tx	Cooling atmosphere
Hydrogenation	550	-	10.1, 52min	100% Ar	1	25%H_2+75%Ar	10, 53min	RT	Ar
	600	-	10.0, 58min	100% Ar	1	25%H_2+75%Ar	10, 58min	RT	Ar
	650	-	10.0, 63min	100% Ar	1	25%H_2+75%Ar	10, 63min	RT	Ar
	700	-	10.3, 66min	100% Ar	1	25%H_2+75%Ar	10, 66min	RT	Ar
	750	-	10.3, 70min	100% Ar	1	25%H_2+75%Ar	10, 73min	RT	Ar
	800	-	10.2, 76min	100% Ar	1	25%H_2+75%Ar	10, 78min	RT	Ar
	850	-	9.9, 83min	100% Ar	1	25%H_2+75%Ar	10, 83min	RT	Ar
Solutionizing	800	650°C hydro. x 1h	10.7, 14min	25%H_2+75%Ar	1/4	25%H_2+75%Ar	10, 80min	RT	Ar
	850	650°C hydro. x 1h	10.5, 19min	25%H_2+75%Ar	1/4	25%H_2+75%Ar	10, 85min	RT	Ar
	900	650°C hydro. x 1h	10.9, 23min	25%H_2+75%Ar	1/4	25%H_2+75%Ar	10, 90min	RT	Ar
Eutectoid decomposition (E.D.)	600	900°C solutionized, 1/4 h	10.0, 30min	25%H_2+75%Ar	3	25%H_2+75%Ar	10, 58min	RT	Ar
Dehyrogenation	600	600°C E.D. x 3 h	-	25%H_2+75%Ar	6	Vacuum	10, 58min	RT	Vacuum
	600	600°C E.D. x 3 h	-	25%H_2+75%Ar	18	Vacuum	10, 58min	RT	Vacuum
	600	600°C E.D. x 3 h	-	25%H_2+75%Ar	24	Vacuum	10, 58min	RT	Vacuum
	700	600°C E.D. x 3 h	10.2, 10min	25%H_2+75%Ar	6	Vacuum	10, 58min	RT	Vacuum
	700	600°C E.D. x 3 h	10.0, 10min	25%H_2+75%Ar	18	Vacuum	10, 58min	RT	Vacuum
	700	600°C E.D. x 3 h	10.1, 10min	25%H_2+75%Ar	24	Vacuum	10, 58min	RT	Vacuum
	800	600°C E.D. x 3 h	10.2, 20min	25%H_2+75%Ar	6	Vacuum	10, 58min	RT	Vacuum
	800	600°C E.D. x 3 h	10.1, 20min	25%H_2+75%Ar	18	Vacuum	10, 58min	RT	Vacuum
	800	600°C E.D. x 3 h	10.3, 19min	25%H_2+75%Ar	24	Vacuum	10, 58min	RT	Vacuum

APPENDIX C

Table C. 1: Standards in the scope of additive manufacturing

Standards	Name of the Standards
ASTM F2792	Terminology for Additive Manufacturing Technologies
ASTM F2915	Standard Specification for Additive Manufacturing File Format (AMF)
ASTM F2921	Terminology for Additive Manufacturing - Coordinate Systems and Test Methodologies
ASTM F2924	Specification for Additive Manufacturing Titanium-6 Aluminum-4 Vanadium with Powder Bed Fusion
ASTM F2971	Standard Practice for Reporting Data for Test Specimens Prepared by Additive Manufacturing
ASTM F3001	Standard Specification for Additive Manufacturing Titanium-6 Aluminum-4 Vanadium ELI with Powder Bed Fusion
ASTM F3049	Standard Guide for Characterizing Properties of Metal Powders Used for Additive Manufacturing Processes
ASTM F3055	Standard Specification for Additive Manufacturing Nickel Alloy (UNS N07718) with Powder Bed Fusion
ASTM F3056	Standard Specification for Standard Specification for Powder Bed Fusion
ASTM F3091	Standard Specification for Powder Bed Fusion of Plastic Materials
ASTM F3122	Standard Guide for Evaluating Mechanical Properties of Metal Materials Made via Additive Manufacturing Processes
ASTM F3184	Standard Specification for Additive Manufacturing Stainless Steel Alloy (UNS S31603) with Powder Bed Fusion
ASTM F3187	Standard Guide for Directed Energy Deposition of Metals
ISO/ASTM 52900	Terminology for Additive Manufacturing – General Principles – Terminology
ISO/ASTM 52915	Specification for Additive Manufacturing File Format (AMF) Version 1.2
ISO/ASTM 52921	Terminology for Additive Manufacturing - Coordinate Systems and Test Methodologies